CFD Simulation of Combustion Using Automatically Reduced Reaction Mechanisms: A Case for Diesel Engine

D I S S E R T A T I O N

submitted to the

Combined Faculties for the Natural Sciences and for Mathematics

of the Rupertus-Carola University of Heidelberg, Germany

for the degree of

Doctor of Natural Sciences

presented by

Ravindra Aglave, M. Chem. Engg.

born in Allahabad, India

Examiners: Prof. Dr. Dr. h. c. Jürgen Warnatz
Prof. Dr. Olaf Deutschmann

Heidelberg, February 23, 2007

Interdisciplinary Center for Scientific Computing
Rupertus - Carola - University of Heidelberg
2007

D I S S E R T A T I O N

submitted to the

Faculty of Physical Chemistry

of the Rupertus-Carola-University of

Heidelberg, Germany

for the degree of

Doctor of Natural Sciences

presented by

Ravindra Aglave, M. Chem. Engg.

born in Allahabad, India

Heidelberg, February 23, 2007

Title

CFD Simulation of Combustion Using Automatically Reduced Reaction Mechanisms: A Case for Diesel Engine

Examiners: Prof. Dr. Dr. h. c. Jürgen Warnatz
Prof. Dr. Olaf Deutschmann

Acknowledgments

There are numerous people whose inspiration, support and encouragement was directly or indirectly responsible to make this work possible.

I am permanently indebted to my thesis supervisor, Prof. Dr. Dr. h. c. Jürgen Warnatz, for providing me the opportunity for doctoral work in his group. His constant encouragement, many insightful suggestions, letting me have independence in my work and not to mention his whistling tunes that added humor to the atmosphere, were crucial in achieving my goals.

But for a meeting in a quaint small town restaurant in Ponca City, USA, with Prof. Olaf Deutschmann of Karlsruhe University (then at University of Heidelberg), I would not have been able to find my way toward this Ph.D. I express my grateful appreciation to him for being supportive and instrumental in fulfilling my quest for doctoral work.

On the count of inspiration, I would like to express my gratitude to Prof. Robert Hesketh of Rowan University, New Jersey (then at the University of Tulsa), for introducing me to the wonderful world of combustion and Dr. Richard Martin of Oral Roberts University, Tulsa (formerly Cheif Technology Officer of Callidus Technologies Inc.), for opening the door to Computational Fluid Dynamics.

I am grateful to Chrys Correa of BASF AG for patiently answering many of my questions regarding KIVA and Baris Ali Sen, whom I have never met in person, from Istanbul Technical University for his e-help on ILDM. I would also like to thank Prof. Bedii Ozdemir from Istanbul Technical University for many discussions and explanations on combustion modeling.

Thanks are also due to Priv. Doz. Dr. Uwe Riedel for giving useful comments on the thesis as well as solving all administrative and financial hurdles during my stay. Thanks to Berthold Schramm & Anton Ishmurzin for assisting me in creating the ILDM tables initially. I also thank Volkmar Reinhardt profusely for creating several ILDM tables and for his patience with me. Crina Heghes and Volker Karbach are thanked for the discussions on reaction kinetics issues. I appreciate Jürgen Moldenhauer and Jan Pitann for providing timely computer and hardware assistance. Rest of my colleagues and staff at IWR are acknowledged with content for their friendship.

Finally, I want to thank my parents for showing tremendous faith in me. My wife Ashwini deserves a heartfelt "thank you" for re-inspiring me for my Ph.D. and for her constant companionship, unwavering support, endless optimism and cheerful encouragement. This is her belated wedding gift.

Ravindra Aglave
Heidelberg, December 2006

Summary

Recent rise in oil prices and continued difficulties in raising gasoline production capacity of refineries has indicated that Diesel engines may play an important role in addressing the transportation needs of near future. It is not only cheaper to produce Diesel, but it is also a more efficient fuel based on energy per volume (9700 kcal/L), when compared to gasoline (8330 kcal/L). High-pressure operation (a compression ratio of 14:1 to 25:1) and absence of electronic spark ignition mechanism are some of the other advantages of Diesel engines.

In Europe, the share of Diesel cars has been growing strongly. In the UK, Diesel cars stock increased from 3% in 1990 to almost 15% in 2000 [1]. Diesels accounted for 42% market in Germany and 49% in entire Europe by end of 2005 [2] . Additionally, in view of the need to increase efficiency and meet the current EURO-IV[1] and subsequnt EURO-V[2] vehicle emission norms, tremendous effort is required in improving the design of Deisel engines.

Mathematical simulation of combustion in Diesel engines can play an important role in understanding not only the underlying physical and chemical processes such as spray dynamics, ignition, chemistry, heat transfer etc., but also the interactions between them, such as chemistry-turbulence interactions. It can aid in conceptualizing efficient designs and give capability of predicting pollutant formation.

Computational Fluid Dynamics (CFD) is a technique that uses numerical solutions to the governing equations of fluid dynamics. The complex set of partial differential equations are solved in a geometrical domain divided into small volumes, commonly known as mesh (or grid). In the present work, a standard finite-volume CFD code, KIVA III, which is capable of simulating two-phase engine flows is used. KIVA-III solves the three-dimensional Favre-averaged Navier-Stokes equations for a Diesel engine. A choice of RNG (Renormalised Group theory) k-ϵ model is added to the original k-ϵ model for describing turbulence. The spray dynamics are handled using a discrete droplet model (DDM) along with sub-models for collision, breakup, evaporation, etc. Sub-models are added for pollutant formation prediction, ignition, turbulence-chemistry interactions, radiation heat transfer and an updated wall-heat transfer algorithm. New models introduce the capability of harnessing the predictive capabilities of detail chemistry at industrially affordable computational time and resources.

[1]EURO-IV is a emission standard applicable vehicles sold in the EU from 2005. It limits diesel passenger car emissions to 0.25 g/km of NO_x and 0.025 g/km of Particulate Matter (PM), petrol cars to 0.08 g/km NOx and Heavy Goods Vehicles (HGVs) to 3.5 g/kWh of NO_x and 0.02 g/kWh of PM.

[2]EURO-V is the future mandatory European emission standard applicable to vehicles sold in the EU (heavy duty vehicles brought on the market from October 2008). It requires Heavy Goods Vehicles (HGVs) to emit no more than 2.0 g/kWh of NOx and 0.02 g/kWh of PM. A proposal suggests to limit Diesel car emissions to 0.200 g/km of NOx and 0.005 g/km of Particulate Matter (PM), petrol cars to 0.060 g/km NOx and 0.005 g/km PM.

The intrinsic low-dimensional manifold (ILDM) method is a technique for automatic reduction of a detailed chemical mechanism based on a local time scale analysis. Chemical processes faster in comparison to the turbulent mixing time scale are assumed to be in a dynamic equilibrium, allowing the chemistry to be expressed only in terms of a few progress variables. It allows the prediction of intermediate and minor species in order to accurately capture the flame propagation and predict pollutant formation. In current work, using n-heptane as a model Diesel fuel, a one- and two-dimensional ILDM with the CO_2 and H_2O as the progress variable is created. It is combined with a presumed probability density function (PDF) method in order to enable turbulence-chemistry interactions. Scalar dissipation rate is calculated to compare the mechanical and chemistry time scales and to choose the appropriate numerical cells for chemistry calculations. NO_x and soot, which are considered as the main pollutants in a Diesel engine are predicted using a Zeldovich model and a phenomenological two-equation model respectively, with the NO and soot precursors obtained from the ILDM chemistry.

Low-temperature reactions lead to the slow formation of a radical pool after the fuel is injected in the engine. The concentration of this radical pool increases during the ignition-delay period due to chain reactions. After a critical mass of radicals is formed, rapid reactions start, indicating the occurrence of ignition. It is impractical to use hundreds of reacting species and thousands of reactions in the ignition simulation. In the present work, a representative species (here CO) is tracked to detect ignition, whose concentration remains almost zero during the ignition period and which shows a sharp increase at ignition. The reaction rate of CO is obtained from pre-tabulated data generated from a comprehensive detailed mechanism, as a function of temperature and CO concentration. Turbulence-chemistry interactions are accounted for by integrating the reaction rate over a presumed probability density function (PDF). Therefore, ignition-delay can be calculated and location of ignition can be identified precisely. Both parameters play a critical role in further flame propagation and ultimately pollutant formation.

Radiation is an important mode of heat transfer in soot-rich Diesel engines. The six-dimensional radiative transfer equation (RTE) is solved for the radiative intensity. Models describing the variation of the radiative properties (e.g., absorption coefficients) with wavelength are incorporated. The radiative properties of the gases (CO_2 and H_2O) are described with a weighted sum of gray gases model (WSGGM). It calculates the total emissivity of a non-gray gas as the weighted sum of the emissivities of a small number of gray gases. The RTE is solved in discrete directions to describe the angular dependence of the intensity using the discrete ordinates method (DOM) with an assumption of optically thin medium. Like other parameters simulated, here too, the turbulence-radiation interactions are described using a presumed PDF approach.

A Caterpillar Diesel engine, for which experimental data were available, is simulated for several injection timings. Ignition is observed to occur at the edge of the spray, in the lean-to-stoichiometric region, where the temperatures are higher.

Thermal NO formation is seen in the stoichiometric region at high temperatures, while soot formation was seen in the richer regions where the temperatures are low. Simulated pressure, temperature and heat release curves show good agreement with experimental data. The mean NO at the end of the cycle was compared to experimental values and also showed reasonable agreement (a maximum deviation of about 10% was observed). The predicted mean soot (maximum deviation of about 30% from experimental values) at the end of the cycle showed an improved accuracy when compared to previous work.

This work establishes the suitability of ILDM in simulating turbulence-chemistry interactions using a presumed PDF approach, with greater accuracy in predicting kinetically controlled processes, without the computational burdens of using detail kinetic reaction mechanisms.

Zusammenfassung

Der Anstieg der Ölpreise der letzten Jahre sowie anhaltende Schwierigkeiten bei der Erhöhung der Kapazitäten von Erdölraffinerien zur Erzeugung von Benzin haben bereits angedeutet, daß den Dieselmotoren in naher Zukunft eine wichtige Rolle bei der Bewältigung der Mobilitätsbedürfnisse zukommen werden. Es ist nicht nur preiswerter, Diesel herzustellen, er hat im Vergleich zu Benzin auch die höhere Energidichte. In Europa hat sich der Anteil von Dieselfahrzeugen stark erhöht. In Großbritannien hat sich der Bestand an Dieselfahrzeugen von 3% im Jahr 1990 auf fast 15% im Jahr 2000 erhöht [1]. Ende 2005 hatten Dieselfahrzeuge in Deutschland einen Marktanteil von 42%, europaweit von 49% [2]. Große Anstrengungen müssen unternommen werden, das Design von Dieselmotoren zu verbessern, um deren Effizienz im Hinblick auf die Anforderungen der derzeitigen EURO IV[3]- und der nachfolgenden EURO V[4]- Abgasnormen zu steigern.

Mathematische Simulationen der Verbrennungsvorgänge in Dieselmotoren können einen wichtigen Beitrag zum Verständnis nicht nur der einzelnen physikalischen und chemischen Prozesse wie Spraydynamik, Zündung, Chemie, Wärmetransfer usw. liefern, sondern auch zu deren Zusammenspiel, wie z.B. der Chemie-Turbulenz-Wechselwirkungen. Sie können bei der konzeptionellen Entwicklung effizienter Konstruktionen hilfreich sein und ermöglichen die Vorhersage der Schadstoffentstehung.

"Computational Fluid Dynamics" (CFD) ist eine Methode, die auf der numerischen Lösung der Gleichungen der Strömungsmechanik beruht. Das komplexe System von partiellen Differentialgleichungen wird in einem geometrischen Gebiet gelöst, das in kleine Volumen, das sogenannte Gitter, unterteilt ist. In der vorliegenden Arbeit wird ein Standardprogramm für finite Volumen CFD-Berechnungen (KIVA-III) verwendet, das in der Lage ist, Zweiphasenströmungen in Motoren zu berechnen. KIVA-III löst die dreidimensionalen Favre-gemittelten Navier-Stokes-Gleichungen für einen Dieselmotor. Ein neues RNG (Renormierungs-Gruppen Theorie) k-ϵ-Model wird dem vorhandenen k-ϵ-Model hinzugefügt, um Turbulenz zubeschrieben. Die Dynamik des Sprays wird mit Hilfe eines diskreten Tröpfchenmodels "Discrete Droplet Model" (DDM) zusammen mit Teilmodellen für die Kollision, das Zerplatzen, das Verdampfen usw. der Tröpfchen beschrieben. Weitere Teilmodelle zur Vorhersage der Schadstoffentwicklung, für den Zündprozeß, der Chemie-Turbulenzwechselwirkung, der Wärmeübertragung durch Strahlung und ein aktualisierter Algorithmus der Wärmeübertragung an der Wand werden hinzugefügt. Die

[3]EURO-IV ist ein Abgasstandard für Fahrzeuge, die in der EU seit dem Jahr 2005 verkauft wurden. Er beschränkt deren Emissionen auf 0,25 g/km NOx und 0,025 g/km Feinstaub für Diesel-PKW, auf 0,08 g/km NOx für Benzinfahrzeuge und auf 3,5 g/kWh NOx and 0,02 g/kWh Feinstaub für Lastkraftwagen.

[4]Die EURO-V Norm ist der zukünftige europäische Abgasstandard (für neu auf den Markt gebrachte Lastkraftwagen ab Oktober 2008). Er schreibt vor, daß LKW nicht mehr als 2,0 g/km NOx und 0,02 g/kWh Feinstaub emittieren dürfen. Ein Vorschlag sieht vor, den Ausstoß von Diesel-PKW auf 0,200 g/km NOx und 0,005 g/km Feinstaub, von Benzinfahrzeugen auf 0,060 g/km NOx und 0,005 g/km Feinstaub zu limitieren.

neuen Modelle eröffnen die Möglichkeit, die Vorhersagekraft detaillierter chemischer Modelle zu einem für die industrielle Anwendung praktikablen Bedarf an Rechenzeit und Resourcen auszunutzen.

Die Methode der "Intrinsic Low-Dimensional Manifold" (ILDM) ist eine Technik zur automatischen Vereinfachung detaillierter chemischer Reaktionsmechanismen, die auf der Analyse lokaler Zeitskalen beruht. Chemische Prozesse, die im Vergleich zu turbulenten Mischprozessen schneller ablaufen, werden als im dynamischen Gleichgewicht betrachtet. Dies erlaubt die Beschreibung der chemischen Prozesse durch wenige Fortschrittsvariablen. Die Methode ermöglicht die Vorhersage von Zwischenprodukten und Spezies geringer Konzentration, um die Flammenausbreitung und die Entstehung von Schadstoffen präzise wiedergeben zu können. In der vorliegenden Arbeit, in der n-Heptan als Modellbrennstoff für Diesel benutzt wird, werden eine ein- und eine zweidimensionale ILDM mit CO_2 und H_2O als Fortschrittsvariablen erzeugt. Die ILDM-Methode wird mit einer angenommenen Wahrscheinlichkeitsdichtefunktion (PDF Methode) kombiniert, um Chemie-Turbulenzwechselwirkungen zu ermöglichen. Die skalare Dissipationsrate wird berechnet, um Beschreibung von mechanischen mit den chemischen Zeitskalen zu vergleichen und die angemessene numerische Zellengrößen für die Berechnung der chemischen Prozesse zu bestimmen. NOx und Ruß, die die Hauptschadstoffe eines Dieselmotors sind, werden mit Hilfe des Zeldovich-Modelles und eines phänomenologischen Zweigleichungsmodelles berechnet, jeweils mit den NO- und Rußvorläufern, die der ILDM Methode entnommen werden.

Nachdem der Brennstoff in den Motor eingespritzt wurde, führen Niedertemperaturreaktionen zur langsamen Bildung eines Reservoirs von Radikalen. Die Konzentration dieser Radikale erhöht sich während der Zündverzugszeit durch Kettenreaktionen. Nachdem eine kritische Anzahl von Radikalen erzeugt wurde, starten schnelle Reaktionen, die den Zündzeitpunkt kennzeichnen. Es ist in der Praxis nicht möglich, die Hunderte von reagierenden Spezies und Tausende von Reaktionen in der Simulation des Motors zu berücksichtigen. In dieser Arbeit wird eine repräsentative Spezies (hier CO) benutzt, um den Zündzeitpunkt zu erkennen. Die Konzentration dieser Spezies verbleibt auf einem sehr geringen Niveau während der Zündperiode und zeigt einen steilen Anstieg beim Zündzeitpunkt. Die Reaktionsrate von CO wird als Funktion der Temperatur und CO-Konzentration einer Tabelle entnommen, die mit Hilfe eines umfassenden, detaillierten Reaktionsmachanismuses erstellt wurde. Die Chemie-Turbulenzwechselwirkung wird berücksichtigt, indem die Reaktionsrate über eine angenommene Wahrscheinlichkeitsdichtefunktion integriert wird (PDF). Somit kann die Zündverzugszeit berechnet werden, und der Zündzeitpunkt kann identifiziert werden. Beide Parameter spielen eine kritische Rolle bei der späteren Flammenausbreitung und der Bildung von Schadstoffen.

Wärmestrahlung ist ein wichtiger Mechanismus der Wärmeübertragung in rußenden Dieselmotoren. Um die Strahlungsintensität zu erhalten, wird die 6-dimensionale Gleichung der strahlungsbedingten Wärmeübertragung (RTE, radiative transfer equation) gelöst. Modelle werden verwendet, die die Abhängigkeit der Strahlung-

seigenschaften (wie z.B. Absorptionskoeffizienten) von der Wellenlänge beschreiben. Die Strahlungseigenschaften der Gase (CO_2 und H_2O) werden durch eine gewichtete Summe von Modellen grauer Gase (WSGGM, weighted sum of gray gases model) beschrieben. Dieses Model berechnet die gesamte Abstrahlung eines nicht-grauen Gases als gewichtete Summe der Abstrahlungen einer kleinen Anzahl von grauen Gasen. Die Wärmeübertragungsgleichung (RTE) wird mit Hilfe der sogenannten "discrete ordinates method" Methode (DOM) in einzelnen Raumrichtungen gelöst, um die Winkelabhängigkeit der Strahlungsintensität beschreiben zu können. Dabei wird ein optisch dünnes Medium angenommen. Wieder wird die Turbulenz-Strahlungswechselwirkung durch Wahrscheinlichkeitsdichtefunktionen beschrieben.

Ein Dieselmotor von Caterpillar, für den experimentelle Daten verfügbar sind, wird für die Simulationen verschiedener Einspritzzeitpunkte verwendet. Es wird beobachtet, daß die Zündung an den Rändern des Sprays stattfindet, in der Region magerer bis stöchiometrischer Zusammensetzung, wo die Temperaturen höher sind. Die Bildung thermischen Stickstoffmonoxids wird im stöchiometrischen Gebiet bei hohen Temperaturen beobachtet, während die Rußbildung in den fetteren Regionen, wo die Temperaturen geringer sind, stattfindet. Die simulierten Druck-, Temperatur- und Wärmefreisetzungsverläufe stimmen gut mit den experimentellen Daten überein. Die mittlere NO-Konzentration am Ende des Motorzykluses wird ebenfalls mit experimentellen Werten vergleichen. Es zeigt sich eine ausreichend gute Übereinstimmung (die maximale Abweichung beträgt 10%). Die Genauigkeit der vorhergesagten mittleren Rußmenge am Ende eines Zyklus (maximale Abweichung 30% zu den experimentellen Daten) wird verbessert.

Diese Arbeit zeigt die Anwendbarkeit der ILDM-Methode bei der Simulation von Turbulenz-Chemiewechselwirkungen mit Hilfe angenommener Wahrscheinlochkeitsdichtefunktionen. Die ILDM Methode ermöglicht höhere Genauigkeit bei der Beschreibung kinetisch bedingter Prozesse, ohne aber die Bürde des großen rechentechnischen Aufwands detaillierter Reaktionsmechanismen auf sich nehmen zu müssen.

Contents

Chapter 1

Introduction

1.1 Background

Since the beginning of civilization, combustion of fuels has provided for majority of our energy needs. It still continues to provide for tgreater than 70 % [3] of the current energy needs of the planet. Therefore, combustion remains a key energy technology for the foreseeable future. Combustion is a phenomenon through which the energy trapped in various fuels is converted from chemical form to heat (and light) form. This energy can then be further utilized for generating steam, electricity, space-heating, transportation, cooking and many other applications. The fuel used in industrial and domestic combustion equipment can occur in any of the three naturally occurring phases (solids, liquids and gases). This fuel has to react with oxygen, occurring in gaseous form. Therefore it is also needs to be converted to gaseous form before undergoing combustion reactions. This conversion occurs by the evaporation of liquid fuels or release of the gases from solid fuels at high temperatures.

At a molecular level, the two reactants can undergo a change in their electronic configuration to form or break bonds that result in a chemical reaction. They have to be mixed thoroughly to carry out efficient combustion. Therefore bringing the two reactants, *viz.* fuel and oxygen, in the close proximity of each other at molecular level, forms a challenging part of designing any combustion equipment. Experimental investigations give useful data that can be used in designing such equipment while theoretical developments attempt to explain the observed experimental behavior. Numerical simulations give the necessary predictive capacity for designing combustion systems. Experimental results as well as theoretical propositions are used in the formulation of a successful numerical simulation.

Most fuels used in combustion applications are a mixture of several chemical species. Each of these species reacts with oxygen releasing its respective heat of reaction. These reactions do not occur as a single-step process, but constitute several elementary steps involving many intermediate species. Knowledge of all such steps and intermediate species is essential in understanding the combustion behavior of fuels. Several decades of research has yielded mathematical and numerical methods

for the treatment of the complex nature of chemical reactions. These include detail chemical kinetic modeling, equilibrium calculations and the solution of species balance equations in simple flow geometries.

The nature of the fluid flow inside combustion systems are varied, ranging from laminar in some cases to turbulent in majority of industrial equipment. The flow of fluids can have additional characteristics such that it may be compressible, swirling, and unsteady with respect to time or any of the combinations of the above. The characteristics of flow affect the way and extent to which the molecules of the fuel and the oxidant come in contact with each other. Thus, in addition to the detail knowledge of chemistry and the turbulent behavior of processes, it is also necessary to have a descriptive method of simulating the interactions between the two (*viz.* turbulence-chemistry interactions).

Combustion reactions typically give rise to several pollutants such as soot, NO_x and SO_x. Accurate prediction of these pollutants requires that all the details of chemical reactions be incorporated in the flow simulation. This becomes exhaustive for the cases of turbulent flows. Using a simplistic reaction simulation approach can give good results with respect to heat release and flow patterns, but fail to capture the details of ignition time delays and pollutant formation. On similar lines, complex ways (e.g. Monte Carlo) of modeling turbulent flows can also be exhaustive.

Several ways of modeling the minute details of turbulence alone and chemical reactions alone exist, evolving from the simplified approach of earlier days to most recent complex and numerically intensive approaches. Some of them are described in the following chapters. However for effective design and optimization in current industry, a balance of accuracy and duration-of-calculation is required. An approach that focuses only on the details of one of the phenomenon, can be misleading or not serve the overall purpose of simulation studies.

1.2 Combustion Processes

Combustion processes can be sub-divided based on mixing as premixed, non-premixed and partially premixed. Combustion in homogeneous-charge spark-ignition engines and lean-burn turbines is under premixed conditions. Contrastingly, combustion in Diesel engines or industrial furnaces is under non-premixed conditions. In the non-premixed cases, fuel is injected into the combustion chamber along with air, where it is ignited due to pre-existing hot gases or auto-ignites due to high temperature.

A second criterion for subdividing the turbulent combustion relates to the ratio of turbulence to chemical reaction time scales. Above a certain cross-over temperature, hydrocarbon oxidation occurs by chain-branching. Chain-branching ceases when the temperature falls below this limit, thus causing extinction of flame. This crossover-temperature increases with pressure. While the fast chemical processes can be simulated using equilibrium approach, slow chemical reactions require being modeled using kinetic expressions. Presence of slow and very fast reactions in the same

reaction mechanism can pose problems in numerical solutions due to stiffness of the equations.

Most industrial combustion processes involve turbulent flows. Laminar flows are encountered in few industrial cases and a large number of academic cases. Flow simulations require the solutions of balance equations (of mass, energy and momentum). These equations are mostly of partial differential form. Laminar flow cases are much simpler and straightforward and can often be approximated with 1-dimensional treatment. Presence of turbulence in the flow requires special treatment to account for the complex nature of turbulence.

1.3 Turbulence and Length Scales

Turbulent flows have a range of length scales along which energy is transferred, constituting the energy cascade. Kinetic energy enters the flow as large eddies break up into small eddies, which in turn break up into smaller eddies. And the smallest eddies disappear into viscous forces [4]. The range of scales starts from the geometry-dependent integral length scale and diminishes down to those of the smallest of the eddies, called Kolmogorov length scale, as seen in Figure 1.1. It shows the energy $E(k)$ of the eddies as a function of a wavenumber k, which is the inverse of the length scale. In order to characterize the length scales at any position,

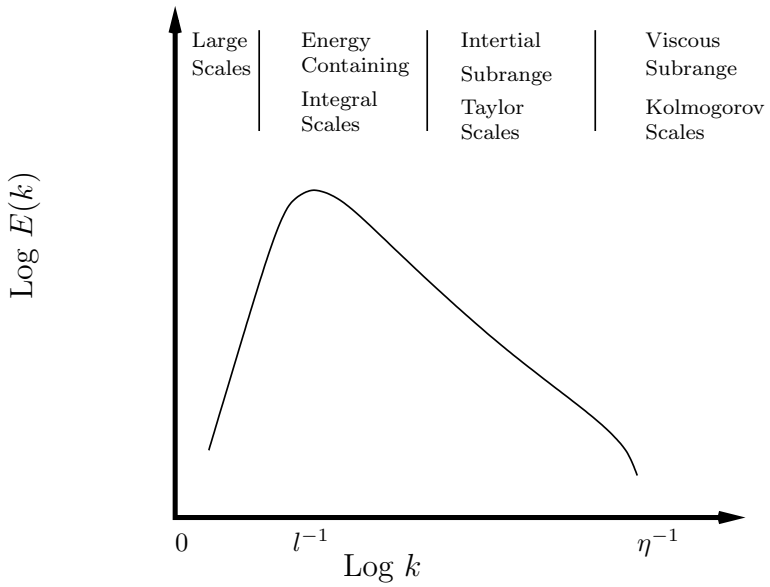

Figure 1.1: Schematic representation of the turbulent kinetic energy spectrum.

one has to measure at point x and time t the velocity $\boldsymbol{u}(x,t)$ and simultaneously at a second point $\boldsymbol{u}(x+r,t)$ with distance r apart. The correlation between these two points is defined by the average

$$R(x,r,t) = \overline{\boldsymbol{u}'(x,t)\,\boldsymbol{u}'(x+r,t)} \tag{1.1}$$

Using Kolmogorov's hypothesis of homogeneous isotropic turbulence at sufficiently high Reynolds number, the above correlation can be normalized to

$$f(r,t) = R(r,t) / \overline{\boldsymbol{u}'^2(t)} \tag{1.2}$$

The eddies of integral length scale contain the most energy and is given by

$$l(t) = \int_0^\infty f(r,t) \cdot \mathrm{d}r \qquad . \tag{1.3}$$

For very small values of r, only very small eddies fit into the distance between x and $x + r$. The motion of these small eddies is governed by viscosity. The dimensional analysis of these scales yields the Kolmogorov's length scale, given by;

$$\eta = \left(\frac{\nu^3}{\epsilon}\right)^{1/4} \qquad , \tag{1.4}$$

where ν is the viscosity and ϵ is he turbulent energy dissipation rate. An intermediate scale between the integral and the Kolmogorov scale is λ, called the Taylor micro scale, and is given by;

$$\lambda = \left(\frac{15\nu\boldsymbol{u}'^2}{\epsilon}\right)^{1/2} \qquad . \tag{1.5}$$

λ is interpreted as the distance that a large eddy convects a Kolmogorov eddy during its turnover time.

Two characteristic phenomenon of turbulent flows are *coherent structures* and *intermittancy*. Coherent structures are relatively well organized portions of turbulent flows which have a large length scales and long residence times than eddies. The switching of flow between turbulent and non-turbulent, causing non-uniformity in time and space, is called intermittancy.

Resolving all the length scales in turbulence (as in a Direct Numerical Simulation - DNS) requires tremendous numerical effort . Alternately, turbulent flow equations can be averaged and solved for the averaged quantities, terms as the RANS (Reynolds Averaged Navier-Stokes) quantities. They represent averages over physical spaces which are of order of the integral length scales. This gives rises to the problem of closure of variables. Problem of closure is solved using additional equations for the unclosed terms. In Large Eddy Simulations, an alternative approach, filtering scales smaller than integral scales is used, leading to different means and variances.

1.4 Reactions in Turbulent Flows

The eddy cascade hypothesis forms the basis of closure of models for high Reynolds numbers($\boldsymbol{u}L/\nu$) flows. It assumes an invariance in the energy transfer in the inertial subrange of turbulence. It therefore can relate the quantities at the smaller scales to those at larger scales. That points to the proposition that the viscous effects are not of importance except near the walls. Consequently one can use models which are defined at larger scales and get good results for turbulent flows without reactions.

Presence of reactants can alter the processes of eddy break-up, mixing and subsequent steepening of fuel and oxidizer gradients. Time scales characterizing the combustion processes are of the order of few microseconds or less, except for some of the pollutant forming processes. Flow processes with macroscopic length scale bring reactants close to the reaction zones, causing local mixing. Diffusion processes finally deliver the reactants to the regions where reaction is occurring. Unless nearly homogeneous conditions exist (premixed combustion or enforced turbulent mixing), reactions occur in a spatially narrow zone, typically less than the Kolmogorov scale. The zones remain narrow because there is never a buildup of reactants due to: i.) Slow inefficient diffusion process in gas. ii.) Relatively fast reactions [5]. The reacting zone responds to the oscillations in the reactant concentrations due to turbulence in accordance with the ratio of, the time scale of either the oscillations or the scalar dissipation rate, to that of the time scale of the reaction. Compared to the length scales of the reacting zones, the overall length scale of the combustion device is several orders of magnitude larger.

In the case of an infinitely fast one-step, irreversible reaction, there exists an infinitely thin non-equilibrium layer of reaction. Outside the layer, the concentrations of the fuel and reactions are zero or a linear function of mixture fraction. [4]. The solution in such a case is known as the Burke-Schumann Solution. Instead of an irreversible reaction, if a reversible reaction is assumed, we get an equilibrium solution.

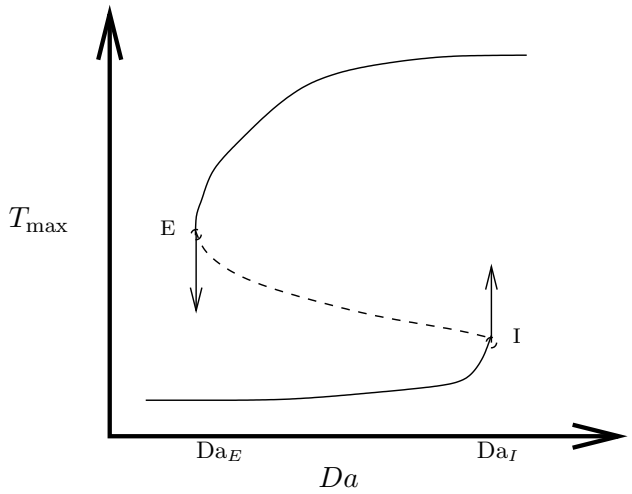

Figure 1.2: The S-shaped curve showing the ignition/extinction as a function of the Damköhler number.

One can therefore conclude that interaction between turbulence and combustion can invalidate the classical scaling laws known in non-reacting turbulent flows. Combustion involves large number of elementary reactions occurring on different time scales. If all the chemical time scales would interact with all the scales in the inertial range, simple scaling laws may be difficult or circumstantial at most [4]. Presence of chemical timescales however does not introduce viscosity as a parameter in dimensional scaling, but molecular properties such as Prandtl's number of Lewis number

can play a role. Heat release during combustion induces an increase in temperature which in turn accelerates the chemistry. Sensitivity of reactions to temperature translates to the physical phenomenon of extinction and ignition. Both of them are difficult to capture in modeling studies. Damkohler number, a ratio of the physical to chemical timescales, is an important parameter that can allow the separation of scales. A plot of maximum temperature versus the Damkohler number in a homogeneous turbulent reactor shows an S-shaped curve (see Figure 1.2). The lower branch is the slow reacting state prior to ignition. Increase in the residence/chemical time leads to ignition at point I. The upper branch is close-to-equilibrium, where the decrease in chemical time (increase in mechanical time) leads to extinction (Point E). Any initial state between the two is driven to either one of the branches. Knowing the stage of combustion (early, mid or late), this information can be utilized to direct any computation to avoid unrealistic results.

1.5 Scope of the Present Work

Present work is aimed at simulating the combustion process in a compression-ignition (CI) Diesel engines using automatically reduced mechanism using the ILDM technique in a 3-dimensional CFD model. While the conditions in the Diesel engine are characterized by high pressure and temperature, analogous approach can be used for simulation of combustion processes for similar non-premixed systems.

Diesel Engines are compression-ignition engines, in which only air is inspirited into the cylinder, unlike spark-ignition engines where an air-fuel mixture is inspirited. The fuel is injected directly into the combustion chamber in the form of a liquid spray. A Diesel engine consists of a cylindrical combustion chamber with a piston. Air is inspirited in the inlet stroke (at the beginning of the cycle) at atmospheric condition (higher if it is a turbocharged engine) when the piston is at the bottom dead center and the intake valve is open. In the compression stroke, the piston compresses the air that is trapped within the chamber, raising it to high temperature, finally stopping at the top dead center (TDC). The compression ratio in the CI engines is in the range of 12-24, much higher than that in the SI engines. Air pressure can reach 80-100 atm. and temperature can reach 800-1000 K at this point. Shortly before the piston reaches the TDC, liquid fuel is sprayed into the combustion chamber. Due to high temperature (above the ignition point of the fuel), the fuel auto-ignites. The time elapsed between the start-of-injection (SOI) and occurrence of ignition is called the ignition-delay time. In the expansion stroke, as the flame spreads through the combustion chamber, heat is released from the fuel. The piston is pushed toward the BDC (bottom dead center) as the hot burnt gases expand. Thus energy is converted to the mechanical movement of piston, which is further translated to a crankshaft and used for transport in an automobile or generate electricity etc. Combustion is completed as the piston reaches the BDC, where it reverses the direction to begin the exhaust stroke. The exhaust valves open and the burnt gases are released. This completes the cycle and the next inlet stroke begins at the end of the cycle.

There are several aspects to be considered for a CFD simulation in the Diesel engine, listed below.

- Combustion occurs at high pressures and the flow cannot be assumed to be incompressible.
- Turbulent flow requires the simulation to be essentially in three dimensions.
- Heat transfer due to radiation, convection and conduction is to be accounted for.
- Liquid spray droplets require a model for heat and mass transfer with the continuous phase, as well as break-up and coalescence.
- Suitable method of predicting the time of auto-ignition.
- Chemistry modeling of abundant and pollutant species.
- Moving grids to simulate the motion of piston.

All of the above mentioned considerations indicate that such a simulation is a complicated, nevertheless a useful exercise.

Presence of reacting species in flow requires the inclusion of additional terms in the equations of change. These are due to the source terms of each of the species and the energy released due to reaction. The change in the species concentration and heat released due to reaction is governed by the equations of rate kinetics. In turbulent reacting flows, these sources terms pose a problem because they are not in closed forms. One method of closing the source terms is through the use of a statistical approach, in which a probability density function (pdf) is formulated over which the source terms can be integrated. This is chosen method for the present work. If large numbers of species are present in the flow, this approach can become numerically expensive. Hence a technique, termed as ILDM (Intrinsically Low Dimensional Manifold), of reducing the reaction scheme to a representative progress variable can be employed. It is a mathematical technique of separating the reactions into fast and slow reaction groups based on eigen-value analysis of the Jacobian of source terms.

In this work, the intermediate species concentrations (C_2H_2, C_3H_3 and O) from ILDM are used in the soot formation and NO_x models to predict the pollutant levels. Variables such as pressure and temperature over the cycle are also predicted. A qualitative analysis of the properties such as flame propagation, ignition location are also presented. Chapter 2 describes the governing equations for modeling turbulent reactive flows. Introduction of RNG (Renormalized group theory) k-ϵ model of turbulence and an enhanced wall heat transfer correlation is also described in this chapter. Chapter 3 discusses the physical models (heat transfer, spray, radiation). The chemistry models (reaction mechanism for n-Heptane oxidation) used in the work are discussed in Chapter 4. It also elaborates the NO formation and destruction as well as the simplified soot model used for pollutant predictions. The technique of automatically reducing the chemical reaction mechanism and the methodology of its coupling to the flow simulation, thereby the focus on turbulence-chemistry interactions, is given in detail in Chapter 5. The key concepts of scalar dissipation

rate and its use in scaling the reaction progress variables for getting accurate results using ILDM methods are also laid out in this chapter. Numerical solution techniques used in KIVA are briefly outline in Chapter 6. Various parametric studies and comparison of results with experimentally available data is presented in Chapter 7. It is followed by a chapter on conclusions and recommendations for future work.

Chapter 2

Governing Equations

The governing equations for a general 3-dimensional flow of fluids are called the Navier-Stokes equations [6]. Additional equations for modeling the spray, chemistry and turbulence are given in the following chapter. These equations describe the balance of mass (total and individual species), momentum and energy in an unsteady, compressible turbulent flow. The compressibility effects are due to the density changes occurring as a result of change in pressure as well as due to chemical reactions. These equations can be derived from fundamental principles of balancing the concerned quantity over an infinitesimally small volume of flow space, and can be found in any standard text book. An Eulerian approach is used in this work, which means that the balance equations are written over a *fixed region of space*. The solution method however is an Arbitrary Lagrangian Eulerian (ALE) described in chapter 5 on numerical methods. The equations are modified to take into account the variations in density (compressible flow) in a Diesel Engine. In these equations, it is assumed that the smallest eddies are much larger than the mean free path of the gas molecules [7]. For compactness, these equations are written in vector notation. The unit vectors in the x-, y- and z-directions are represented by;

$$\vec{\boldsymbol{x}} = x\vec{i} + y\vec{j} + z\vec{k} \qquad . \tag{2.1}$$

The vector operator ∇ is given by

$$\nabla = \vec{\boldsymbol{i}}\frac{\partial}{\partial x} + \vec{\boldsymbol{j}}\frac{\partial}{\partial y} + \vec{\boldsymbol{k}}\frac{\partial}{\partial z} \tag{2.2}$$

and the fluid velocity vector $\vec{\boldsymbol{u}}$ is given by

$$\vec{\boldsymbol{u}} = u\left(x, y, z, t\right)\vec{\boldsymbol{i}} + v\left(x, y, z, t\right)\vec{\boldsymbol{j}} + w\left(x, y, z, t\right)\vec{\boldsymbol{k}} \qquad , \tag{2.3}$$

where t is time. A general balance equation for a variable ϕ over an element contains terms due to

- Change caused by flux through the surface due to diffusion, heat conduction, momentum transport, convection etc.
- Change caused by addition/removal of heat or species due to chemical reaction within the volume of the element.

- Change caused by long range processes like radiation and/or gravity, from surrounding elements.

It can be given by

$$\underbrace{\frac{\partial(\rho\phi)}{\partial t}}_{Accumulation} + \underbrace{\nabla\cdot(\rho\vec{\boldsymbol{u}}\phi)}_{Convection} = \underbrace{\nabla\cdot(\Gamma_\phi\nabla\phi)}_{DiffusionFlux} + \underbrace{S_\phi}_{Source} \quad . \tag{2.4}$$

2.1 Species Mass Balance

If there are n number of species, then the partial mass densities of each species adds up to form the total density ρ. Similarly, local flow velocity $\vec{u_i}$ of species i is composed of total velocity $\vec{\boldsymbol{u}}$ and the diffusion velocity $\vec{\boldsymbol{V_i}}$. Since species are formed and consumed, a production term is present in the equation, which is a product of the molar mass M_i and molar rate of formation ω_i

$$\frac{\partial\rho_i}{\partial t} + \nabla\cdot(\rho_i\vec{\boldsymbol{u_i}}) + \nabla\cdot\vec{\boldsymbol{J_i}} = \dot{\rho_i}^{\mathrm{C}} + \dot{\rho_i}^{\mathrm{S}} \quad , \tag{2.5}$$

where the superscript C and S stand for chemistry and spray (see section 3.3) source terms respectively. The spray term is applicable only to the fuel species in a diesel engine. The chemistry source term is given by

$$\dot{\rho_i}^{\mathrm{C}} = M_i\omega_i \tag{2.6}$$

and the diffusion vector is given by

$$\vec{\boldsymbol{J_i}} = \rho_i\vec{V_i} = -\rho D_i\nabla Y_i \tag{2.7}$$

The mean diffusion coefficient D_i of species i into the rest of the mixture can be calculated from the Stefan's law of diffusion using the binary diffusion coefficients D_{ij} viz.

$$D_i = \frac{1-w_i}{\sum_{i\neq j}\frac{x_j}{D_{ij}}} \quad . \tag{2.8}$$

,

Assuming equal diffusivities for all species , the diffusion coefficient is given by

$$D = \frac{\mu_{\mathrm{eff}}}{\rho Sc} \tag{2.9}$$

Where μ_{eff} is the dynamic viscosity (see Section 3.1) and Sc is the Schmidt Number

2.2 Overall Mass Balance

Addition of all the species transport equations gives the total mass balance equation, also known as the continuity equation. Since mass cannot be created or destroyed, the only source term is the one due to addition of fuel spray (designated as species number 1).

$$\frac{\partial\rho}{\partial t} + \nabla\cdot(\rho\vec{\boldsymbol{u}}) + \dot{\rho_1}^{\mathrm{S}} = 0 \tag{2.10}$$

2.3 Momentum Balance

The momentum balance equations is based on the Newtons second law which states that the acceleration of a fluid particle (rate of change of momentum) is equal to the total surface and body forces. The surface forces are molecular in origin and are described by a stress tensor $\overline{\overline{\sigma}}$

$$\frac{\partial\left(\rho\vec{u}\right)}{\partial t}+\nabla\cdot\left(\rho\vec{\boldsymbol{u}}\otimes\vec{\boldsymbol{u}}\right)-\nabla\cdot\,\overline{\overline{\sigma}}=\nabla p+\rho\vec{\boldsymbol{g}}+\dot{F}^{\mathrm{S}}\qquad,\tag{2.11}$$

where the viscous stress tensor $\overline{\overline{\sigma}}$ is given as

$$\overline{\overline{\sigma}}=\mu\left[\nabla^2\vec{\boldsymbol{u}}+\left(\nabla^2\vec{\boldsymbol{u}}\right)^{\mathrm{T}}\right]-\frac{2}{3}\mu\left(\nabla\cdot\vec{\boldsymbol{u}}\right)\overline{\overline{I}}\qquad.\tag{2.12}$$

2.4 Energy Balance

The energy balance equation is written in accordance with the first law of thermodynamics which states that the increase of the total energy in a material volume must equal the work done on the volume plus the heat added. The total energy is comprised of the internal energy, potential energy and the kinetic energy. A balance written for the internal energy E per unit mass (specific internal energy), excluding the chemical energy, is as follows:

$$\frac{\partial\rho E}{\partial t}+\nabla\cdot\left(\rho\vec{\boldsymbol{u}}E\right)=-p\nabla\cdot\vec{\boldsymbol{u}}+\overline{\overline{\sigma}}\colon\nabla\vec{\boldsymbol{u}}-\nabla\cdot\vec{\boldsymbol{J}}_{\mathrm{q}}+\rho\epsilon+\dot{Q}^{\mathrm{C}}+\dot{Q}^{\mathrm{S}}\qquad,\tag{2.13}$$

where ϵ is the dissipation rate of the turbulent kinetic energy k (see section 3.1). The heat flux vector $\vec{\boldsymbol{J}}_{\mathrm{q}}$ is the sum of contributions from heat conduction (Fouriers Law) and enthalpy diffusion. It can include a third term due to radiation, if applicable(see section 3.4). $\dot{Q}^{\mathrm{C}}$ and $\dot{Q}^{\mathrm{S}}$ are the source terms due to chemistry and spray.

$$\vec{\boldsymbol{J}}_{\mathrm{q}}=-K\nabla T-\rho D\sum h_i\nabla\left(\rho_i/\rho\right)\qquad.\tag{2.14}$$

T is the fluid temperature and h_i is the specific enthalpy of the species i and K is the thermal conductivity. K can be calculated from the Prandtl number Pr by

$$K=\frac{c_p\mu}{Pr}\tag{2.15}$$

$$c_p\left(T\right)=\sum_i c_{p_i}\left(T\right)\frac{\rho_i}{\rho}\qquad.\tag{2.16}$$

Value of Pr and c_p (specific heat capacity) for combustion mixtures can be found from various thermochemical property databases. One such is the JANAF tables [8]

2.5 State Relations

State relations give the additional equations to relate temperature, pressure and the enthalpy. One of the simplest equations of state for this purpose is the ideal gas

law, which is roughly accurate for gases at low pressures and high temperatures. However, this equation becomes increasingly inaccurate at higher pressures and lower temperatures. It is calculated iteratively using

$$T = \sum_i \left[h_i(T) - \frac{\rho_i}{\rho} E(T) \right] \frac{1}{R_0} \quad , \tag{2.17}$$

$$p = R_0 T \sum_i \frac{\rho_i}{M_i} \quad . \tag{2.18}$$

At normal pressures, the volume occupied by gas particles is a negligibly small fraction of the total volume of the gas. But at high pressures, this is no longer true. As a result, real gases are not as compressible at high pressures as an ideal gas. The volume of a real gas is therefore larger or pressure is smaller than expected from the ideal gas equation at high pressures. Redlich-Kwong equation of state is a considerable improvement. It is of interest primarily due to its relatively simple form and is superior to the van der Waals equation of state. The Redlich-Kwong equation is adequate for calculation of gas phase properties when the ratio of the pressure to the critical pressure is less than about one-half of the ratio of the temperature to the critical temperature.

Redlich-Kwong equation of state

$$P = \frac{RT}{V_/Nm - b} - \frac{a}{\sqrt{T} V_m (V_m + b)} \tag{2.19}$$

where $a = \dfrac{0.42748 R^2 T_c^{2.5}}{P_c}$, $b = \dfrac{0.08664 R T_c}{P_c}$, $R =$ ideal gas constant (8.31451 J/(mol·K)), and $V_/Nm =$ molar volume. A correction to the ideal gas law is introduced based on the Redlich-Kwong equation of state. However it did not produce any significant changes (less than 2% difference) in the pressure or temperature profiles, and was ignored for further computations.

2.6 Averaging of Equations

Full numerical solutions of the instantaneous governing equations is a difficult and time-consuming task, and is currently limited to only few simplified cases. This is possible when all the length and time scales involved are resolved. In a Diesel engine, the largest length scales are the integral length scale of the order of 0.1 m while the smallest are those of molecular diffusion, of the order of 10^{-5}m. The resolution of the length scales itself would require 10^4 points on the mesh in each direction, and a total of the order of 10^{12} for a 3-d simulation. If one has to factor in the time scales, then the smallest time scales are 10^{-6}-10^{-7} s. For a combustion cycle of about 30 ms, approximately 10^5 time step may be required. This gives an idea that such a computation may run into several months.

Averaging the instantaneous variable provides a way of describing the mean flow field where the local fluctuating quantities and turbulent structures are integrated into the mean quantities, and circumvents the need to describe them in the simulation.

Each quantity ϕ can be split into a mean quantity $\overline{\phi}$ and a fluctuating quantity $\phi^{'}$. Thus, a statistical method is used to describe the randomness in the flow. The mean of the fluctuations is equal to zero while the mean of the square of the fluctuations is called the variance and is given by

$$\phi = \overline{\phi} + \phi' \tag{2.20}$$

$$\overline{\phi'} = 0 \tag{2.21}$$

$$\phi'^2 = \overline{\phi^2} + \overline{\phi}^2 \quad . \tag{2.22}$$

Averaging over a small time interval is called ensemble averaging or Reynolds averaging technique, we get

$$\overline{\phi\left(t\right)} = \frac{1}{t - t_0} \int_{t_0}^{t} \phi\left(t^{'}\right) \mathrm{d}t^{'} \quad . \tag{2.23}$$

This technique brings unclosed correlations such as $\overline{u'\phi'}$ that are unknown and require modeling. The numerical procedure is called RANS (Reynolds Averaged Navier-Stokes) modeling. In case of Diesel engines, this concept is complicated by the fact that there are cycle-to-cycle variations in the mean quantities itself at any point of time. Therefore, variables are averaged over several cycles. This process is carried out at several crank angle locations to get the ensemble averaged variable over the entire cycle:

$$\overline{\phi_{N_{\mathrm{cyc}}}} = \frac{1}{N_{\mathrm{cyc}}} \sum_{n=1}^{N_{\mathrm{cyc}}} \phi_n \quad . \tag{2.24}$$

2.7 Favre Averaging

In turbulent flames, heat release causes fluctuations in density as well. Hence, Reynolds averaging causes some difficulty by introducing velocity-density correlations $\overline{\rho'\phi'}$. Explicit modeling of such terms can be avoided if a mass weighted average $\widetilde{\phi}$, called Favre average, is introduced. Then any quantity can be decomposed as

$$\phi = \widetilde{\phi} + \phi'' \tag{2.25}$$

$$\widetilde{\phi} = \frac{\overline{\rho\phi}}{\overline{\rho}} \tag{2.26}$$

$$\widetilde{\phi''} = \frac{\overline{\rho\left(\phi - \widetilde{\phi}\right)}}{\overline{\rho}} = 0 \quad . \tag{2.27}$$

Favre averaged balance equation are formally identical to Reynolds averaged equations for constant density flow, Favre averaging being only a mathematical formalism [10]. There is no simple relation between the Reynolds and Favre averages of a variable, since it requires the knowledge of density fluctuations correlation $\rho'\phi'$ remaining hidden in the Favre average:

$$\overline{\rho}\widetilde{\phi} = \rho\phi + \overline{\rho'\phi'} \quad . \tag{2.28}$$

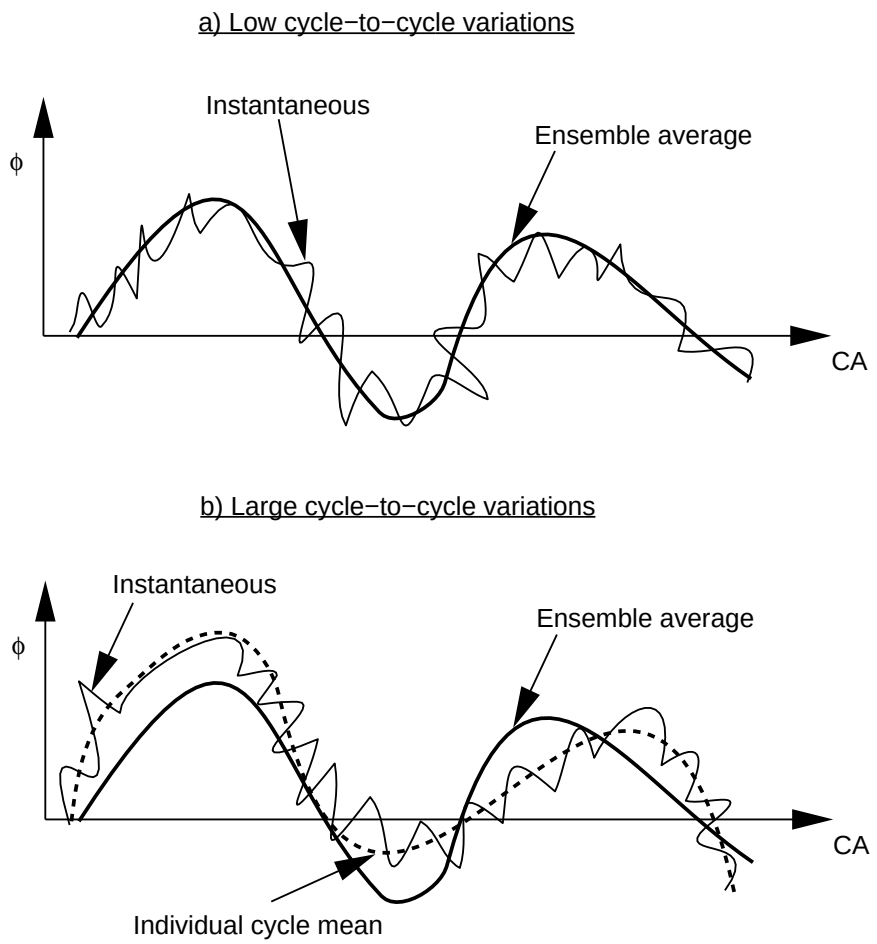

Figure 2.1: Ensemble averaging of variable ϕ as a function of crank angle [9] a: small cycle-to-cycle variations. b: Large cycle-to-cycle variations.

It should also be noted that most experimental techniques determine Reynolds averaged data, and its comparison with Favre-averaged quantities from simulation may not compare well. Finally, the Favre-averaged balance equations (with species density $\rho_i = \rho Y_i$ where Y_i is the mass fraction of species i), are as follows [11]:

Species mass balance

$$\frac{\partial \overline{\rho}\widetilde{Y_i}}{\partial t} + \nabla \cdot \left(\overline{\rho}\widetilde{\vec{\boldsymbol{u}}}\widetilde{Y_i}\right) = \nabla \cdot \left(\overline{\rho D \nabla Y_i} - \overline{\rho \vec{\boldsymbol{u}}'' Y_i''}\right) + \overline{\rho \dot{Y}_i^{\mathrm{C}}} + \overline{\rho \dot{Y}_i^{\mathrm{S}}} \tag{2.29}$$

Total mass balance or continuity equation

$$\frac{\partial \overline{\rho}}{\partial t} + \nabla \cdot \left(\overline{\rho}\widetilde{\vec{\boldsymbol{u}}}\right) = \overline{\dot{\rho}_i^{\mathrm{S}}} \tag{2.30}$$

Momentum balance

$$\frac{\partial \left(\overline{\rho}\vec{\boldsymbol{u}}\right)}{\partial t} + \nabla \cdot \left(\overline{\rho}\widetilde{\vec{\boldsymbol{u}}}\widetilde{\vec{\boldsymbol{u}}}\right) = \nabla \cdot \left(\overline{\overline{\sigma}} - \overline{\rho \vec{\boldsymbol{u}}'' \vec{\boldsymbol{u}}''}\right) - \nabla \widetilde{p} + \overline{\vec{\boldsymbol{F}}^{\mathrm{S}}} + \overline{\rho}\widetilde{\vec{\boldsymbol{g}}} + A_0 \nabla(2/3\rho k) \tag{2.31}$$

Energy balance

$$\frac{\partial\left(\overline{\rho}\widetilde{E}\right)}{\partial t}+\nabla\cdot\left(\overline{\rho}\widetilde{\vec{u}}\widetilde{E}\right)=-\widetilde{p}\nabla\widetilde{\vec{u}}-\nabla\cdot\left(\overline{\vec{J}}+\overline{\rho\vec{u}''E''}\right)+A_0\overline{\rho}\widetilde{\epsilon}+\overline{\dot{Q}^{\mathrm{C}}}+\overline{\dot{Q}^{\mathrm{S}}} \quad (2.32)$$

A_0 is 0 for laminar flow and 1 for turbulent flow. After averaging of the equations, one notices several terms of the form $\overline{\rho\vec{u}''\phi''}$ due to the fluctuations in turbulent flows. These are unknown quantities, and models are required to achieve closure of these terms (see Section 3.1). When the balance equations are closed with the said models, they only allow the determination of mean quantities, which may differ from instantaneous ones and cannot always be sufficient to describe turbulent combustion. Alternative ways are available (LES), which are prohibitive in their computational requirement for an industrial scale 3-D simulation.

Chapter 3

Physical Models

The models used to describe various physical process in the simulation of Diesel engines are described in this chapter. These models, in conjunction with the governing equations, complete the necessary mathematical requirement to simulate the combustion process in Diesel engines.

3.1 Turbulence

For a general statistically three-dimensional flow, there are four independent equations governing the mean velocity filed viz. the three components of the averaged equations for velocity together with mean continuity equation (or the Poisson's equation for pressure). There are also more than four unknowns, viz. the three components of the velocity, pressure and the quantities of the form of $\overline{\rho}\widetilde{\vec{\boldsymbol{u}}}\widetilde{\vec{\boldsymbol{u}}}$ (see Eq. 2.31). These quantities are referred to as Reynolds stresses, stemming from the momentum transfer by a fluctuating velocity field. Since there are more unknowns than the number of equations, a *closure problem* is manifested by the system of equations [12]. A gradient-diffusion hypothesis is used to achieve the closure. According to this hypothesis, the turbulent transport of a scalar is down the (in the direction of decreasing) mean scalar gradient that is in the direction of -ve$\nabla\phi$. This hypothesis can similarly be applied to the terms $\overline{\rho\vec{\boldsymbol{u}}''E''}$ and $\overline{\rho\vec{\boldsymbol{u}}''Y_i''}$ in energy and species balance equations (2.32 and 2.29) or any such scalar ϕ as:

$$\overline{\rho\vec{\boldsymbol{u}}''\phi''} = -\Gamma_{\phi,T}\nabla\widetilde{\phi} \qquad . \tag{3.1}$$

The effective diffusivity $\Gamma_{\phi,\text{eff}}$ is defined as the sum of molecular Γ_ϕ and turbulent $\Gamma_{\phi,\text{T}}$ components. Diffusivities corresponding to mass, energy and momentum transport are shown in the following Table 3.1. In the above diffusivity coefficients, the values for turbulent Prandtl number Pr_T and Schmidt number Sc_T is assumed to be equal to 0.56 and 0.9 respectively, a standard value for air in IC engines. Identical to the mass (species) and energy equations, the turbulent-viscosity hypothesis introduced by Boussinesq is mathematically analogous to the stress - rate-of-strain relation for a Newtonian fluid. As a consequence, Reynolds stress can be written as

$$\overline{\rho\vec{\boldsymbol{u}}''\vec{\boldsymbol{u}}''} = -\overline{\rho}\nu_T\nabla\widetilde{\vec{\boldsymbol{u}}} \qquad . \tag{3.2}$$

Now all that remains is to define the turbulent viscosity, to achieve closure of the equations. There are several models to accomplish this viz. algebraic mod-

Tansport quantity	Mass	Energy	Momentum
Transport coefficient	$\Gamma_{Y_i,\mathrm{T}}$	$\Gamma_{\mathrm{E,T}}$	Γ_{T}
Symbol	D_{T}	K_{T}/c_p	ν_{T}
Formula	$\mu_{\mathrm{T}}/\left(\overline{\rho}Sc_{\mathrm{T}}\right)$	$\mu_{\mathrm{T}}/Pr_{\mathrm{T}}$	$\mu_{\mathrm{T}}/\overline{\rho}$

Table 3.1: Turbulent exchange coefficients.

els (uniform turbulent viscosity model, mixing-length model [13]), one equation models [14, 15], two equation models (standard k-ϵ model [16] and the RNG k-ϵ model [17]) and Reynolds stress models.

3.1.1 *k*-ϵ Turbulence Model

In this simple model, two additional transport equation are solved for the two turbulence quantities viz. the turbulent kinetic energy $\widetilde{k}$ and the energy dissipation rate $\widetilde{\epsilon}$. These two quantities are related to the primary variables and can give a length scale and time scale to form a quantity with dimension of ν_{T}, thus making the model complete (no more flow-dependent specifications are required). This is a widely used model in CFD simulations.

$$\widetilde{k} = \frac{1}{2}\widetilde{u''^2} \tag{3.3}$$

$$\widetilde{\epsilon} = \overline{\nu\nabla\vec{\boldsymbol{u}}''^{\mathrm{T}} : \nabla\vec{\boldsymbol{u}}''} \tag{3.4}$$

$$\nu_{\mathrm{T}} = C_\mu\frac{\widetilde{k}^2}{\widetilde{\epsilon}} \quad . \tag{3.5}$$

The balance equation for $\widetilde{k}$ can be derived from Equations 3.3, 3.4, 3.5 and Equation 2.11 [18], giving

$$\begin{aligned}\frac{\partial\overline{\rho}\widetilde{k}}{\partial t} + \nabla\cdot\left(\overline{\rho}\tilde{\vec{\boldsymbol{u}}}\tilde{k}\right) = &- \frac{2}{3}\overline{\rho}\widetilde{k}\nabla\cdot\tilde{\vec{\boldsymbol{u}}} + \bar{\bar{\sigma}}\colon\nabla\tilde{\vec{\boldsymbol{u}}} + \nabla\cdot\left[\left(\frac{\mu_{\mathrm{eff}}}{Pr_k}\right)\nabla\tilde{k}\right] \\ &- \overline{\rho}\tilde{\epsilon} + \overline{\dot{W}^{\mathrm{S}}} \quad .\end{aligned} \tag{3.6}$$

$$\begin{aligned}\frac{\partial\overline{\rho}\widetilde{\epsilon}}{\partial t} + \nabla\cdot\left(\overline{\rho}\tilde{\vec{\boldsymbol{u}}}\right) = &- \left(\frac{2}{3}c_{\epsilon1} - c_{\epsilon3}\right)\overline{\rho}\widetilde{\epsilon}\nabla\cdot\tilde{\vec{\boldsymbol{u}}} + \nabla\cdot\left[\left(\frac{\mu_{\mathrm{eff}}}{Pr_\epsilon}\right)\nabla\widetilde{\epsilon}\right] \\ &+ \frac{\tilde{\epsilon}}{\tilde{k}}\left[c_{\epsilon1}\,\bar{\bar{\sigma}}\colon\nabla\tilde{\vec{\boldsymbol{u}}} - c_{\epsilon2}\overline{\rho}\tilde{\epsilon} + c_{\mathrm{s}}\overline{\dot{W}^{\mathrm{S}}}\right] \quad .\end{aligned} \tag{3.7}$$

The flow in an IC engine has variable density, causing change in the volume of an infinitesimal material volume. This is termed as velocity dilatation. The term $\left(\frac{2}{3}c_{\epsilon1} - c_{\epsilon3}\right)$ in the ϵ equation is to account for the changes in length scales due to velocity dilatation. The term $\overline{\dot{W}^{\mathrm{S}}}$ is due to spray interactions and described in more detail in section 3.3. The new quantities introduced in these equations are constants whose values are determined by some experimental and theoretical considerations. Standard values are used for engine calculations and are given in Table 3.2

Constant	$c_{\epsilon 1}$	$c_{\epsilon 2}$	$c_{\epsilon 3}$	c_s	Pr_k	Pr_ϵ	η_0	β	c_μ
Standard k-ϵ	1.44	1.92	-1.0	1.5	1.0	1.3	-	-	0.09
RNG k-ϵ	1.42	1.68	Eq.3.1.3	1.5	0.719	0.719	4.38	0.012	0.0845

Table 3.2: Values of the constants in the turbulence models. [18, 19]

3.1.2 Near-Wall Treatment

Treatment of turbulence described in the previous section is mostly valid in the homogeneous shear flow. The nature of flow near the wall requires much closer attention in terms of its mathematical treatment due is small length scales. Near the wall, flow gets separated into an inner layer dominated by viscous effects, and an outer layer where the viscous effects are not so important (divided by red line, see Fig. 3.1). Very close to the wall, within the inner layer (below green line, Fig. 3.1) is

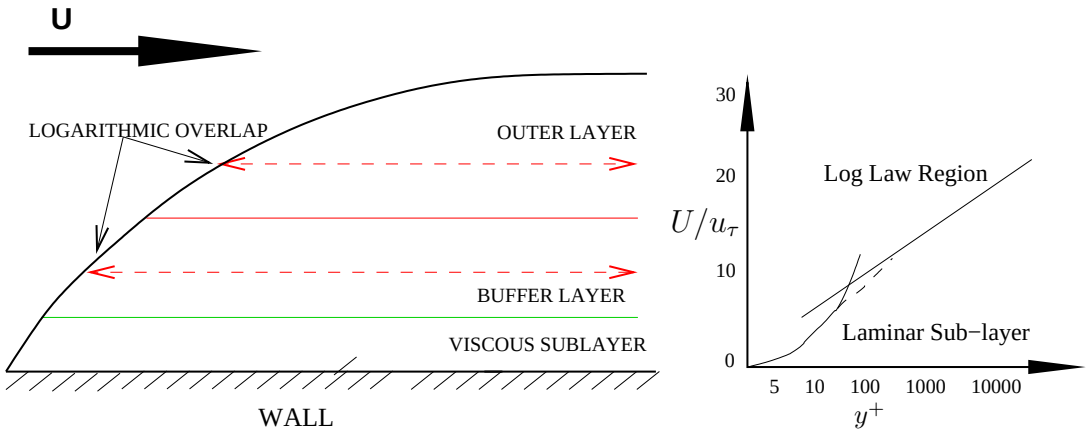

Figure 3.1: Boundary layer showing the logarithmic-law region and laminar sub-layer. Direction of flow is given by the bold arrow. Buffer layer is between the full red and green lines. Logarithmic law region is between the two dotted red lines.

called the viscous or laminar sub-layer. Straddling the inner and outer layer is the logarithmic overlap. While the change in velocity in the normal direction to the wall varies linearly with the distance y from the wall in the laminar sublayer, it varies logarithmically in the logarithmic overlap. The numerical solution of the turbulence model equations is impractical in the near wall region. One needs a simpler function that describes the flow between the last grid point near the wall and the wall. Such a function can be derived with several simplifying assumptions for the flow near the wall region:

1. The flow is quasi-steady.
2. The fluid velocity is directed parallel to a flat wall and varies only in the normal direction.
3. There are no stream wise pressure gradients.
4. There are no chemical reactions or spray source in the wall region.

5. The dimensionless wall heat loss is small compared to unity.
6. Reynolds numbers are large (effective viscosity is larger than laminar viscosity) and Mach numbers are small (dissipation of turbulent energy is negligible source for internal energy)

The k-ϵ equations can thus be rewritten with the above assumptions and in a non-dimensionalised form using the friction velocity (velocity at the wall) u_w defined by

$$u_{\mathrm{w}} = \sqrt{\frac{\tau_{\mathrm{w}}}{\rho_{\mathrm{w}}}} \qquad , \tag{3.8}$$

where τ_{w} is the wall shear stress and ρ_{w} is the wall density. k is non-dimensionalised using ${u_{\mathrm{w}}}^2$ and ϵ using ${u_{\mathrm{w}}}^3/y$ where y is the normal distance from the wall. Near the wall, the balance equations in other directions (viz. x and z) vanish and we are left with the equations only in the y direction. These equations in the expanded form are:

$$c_\mu \rho \frac{k^2}{\epsilon} y \frac{\partial u}{\partial y} = 1 \quad (u) \tag{3.9}$$

$$\frac{\partial}{\partial y}\left[\frac{c_\mu}{Pr_k}\rho\frac{k^2}{\epsilon}y\frac{\partial k}{\partial y}\right] + c_\mu\rho\frac{k^2}{\epsilon}y\left(\frac{\partial u}{\partial y}\right)^2 - \rho\frac{\epsilon}{y} = 0 \quad (k) \tag{3.10}$$

$$\frac{\partial}{\partial y}\left[\frac{c_\mu}{Pr_k}\rho\frac{k^2}{\epsilon}y\frac{\partial}{\partial y}\left(\frac{\epsilon}{y}\right)\right] + c_{\epsilon 1}c_\mu\rho k\left(\frac{\partial u}{\partial y}\right)^2 - c_{\epsilon 2}\rho\frac{\epsilon^2}{y^2 k} = 0 \quad (\epsilon) \quad . \tag{3.11}$$

The solution of the equations for u, k and ϵ using a Taylor series expansion leads to a velocity distribution near the wall give by:

$$u_0 = \frac{1}{\kappa}\ln y + B \tag{3.12}$$

$$\frac{u}{u_{\mathrm{w}}} = \frac{1}{\kappa}\ln\left[c_{\mathrm{lw}}\left(\frac{yu}{\nu_{\mathrm{L}}}\right)^{7/8}\right] + B \quad , \tag{3.13}$$

where κ is called the von Karman's constant and has a value of 0.4372 [18] for the values of model constants given in Table 3.2, B is equal to 5.5 for smooth walls [20], c_{lw} equals 0.15. The above function is called the law-of-the-wall and due to its logarithmic nature, the region of the boundary is called log-law region. In the laminar sublayer, the velocity is calculated using

$$\frac{u}{u_{\mathrm{w}}} = \left(\frac{yu}{\nu_{\mathrm{L}}}\right)^{1/2} \qquad . \tag{3.14}$$

The transition is made where Equation 3.13 and Equation 3.14 predict the same u_{w}. For the given constants, this gives a value of 144. The computed velocities on the grid point closest to the wall is matched to the values calculated using the wall functions. In the final numerical implementation, the tangential velocity at the last cell near the wall is calculated. This is used to evaluate the value of u_w using Equation 3.8 and 3.13. Heat transfer in the near wall region is treated on similar lines and more details are give in section 3.2

3.1.3 RNG k-ϵ Turbulence Model

The Renormalization Group Theory (RNG) concept employs a universal random force which drives the small-scale velocity fluctuations. This force represents the effect of the large scales (including initial and boundary conditions) on the eddies in the inertial range. It is chosen in such a way that the global properties of the resulting flow field are the same as those in the flow driven by the mean strain. The equations of motion for the large-scale field are derived by averaging over an infinitesimal band of small scales to remove them from explicit consideration. The removal process is iterated until the infinitesimal corrections to the equations accumulate to give finite changes. The effect of the small scales that have been removed is accounted for by dynamic equations for the large-scale velocity field through presence of an eddy viscosity. In the limit as successively larger scales are removed, the k-ϵ model is retrieved [19].

The procedure retains only the modifications of the viscosity. After the elimination of the small scales is complete, the random force is dropped from the resulting equations and the initial and boundary conditions are restored. The RNG procedure [17] gives rise to a set of equations having the attractive feature of no undetermined constants, and the presence of built-in corrections that allow the use of the model in both high- and low-Reynolds-number regions of the flow. An extra term appears in the ϵ equation, which is closed by an approximation, in the re-derived version of the model [21] for incompressible flows.

However, turbulence in internal combustion engines is characterised by large density variations even though the Mach numbers are low. Rapid Distortion Analysis is used to close the RNG ϵ equation for the compressible flow case. The final equation for ϵ has an added term and a constant [19] given as:

$$\begin{aligned}\frac{\partial \overline{\rho}\widetilde{\epsilon}}{\partial t} + \nabla\cdot\left(\overline{\rho}\tilde{\vec{u}}\tilde{\epsilon}\right) = \; & - \left(\frac{2}{3}c_{\epsilon 1} - c_{\epsilon 3} - \overbrace{\frac{2}{3}c_\mu c_\eta \frac{\widetilde{k}}{\widetilde{\epsilon}}\nabla\cdot\tilde{\vec{u}}}^{\text{extra term}}\right)\overline{\rho}\widetilde{\epsilon}\nabla\cdot\tilde{\vec{u}} \\ & + \frac{\tilde{\epsilon}}{\tilde{k}}\left[\left(c_{\epsilon 1} - \overbrace{c_\eta}^{\text{extra constant}}\right)\overline{\overline{\sigma}}\colon\nabla\tilde{\vec{u}} - c_{\epsilon 2}\overline{\rho}\tilde{\epsilon} + c_s\overline{\dot{W}^{\mathrm{S}}}\right] \\ & + \nabla\cdot\left[\left(\frac{\mu_{\text{eff}}}{Pr_\epsilon}\right)\nabla\widetilde{\epsilon}\right] \qquad , \end{aligned} \tag{3.15}$$

where

$$c_\eta = \frac{\eta\,(1-\eta/\eta_0)}{1+\beta\eta^3} \tag{3.16}$$

$$\eta = \frac{S\tilde{k}}{\epsilon} \tag{3.17}$$

$$S = \left(2S_{ij}S_{ij}\right)^{1/2} \tag{3.18}$$

$$S_{ij} = \frac{1}{2}\left(\frac{\partial u_i}{\partial x_j} + \frac{\partial u_j}{\partial x_i}\right) \qquad . \tag{3.19}$$

η is the ratio of the turbulent to mean strain rate and S is the magnitude of the mean strain S_{ij}. The values of all constants are give in Table 3.2. For rapid distortion in a compressible, low Mach number flow, following equations give the remaining constants [22].

$$c_{\epsilon 3} = \frac{-1 + 2C_{\epsilon 1} - 3m\,(n-1) + (-1)^{\delta}\sqrt{6}c_{\mu}c_{\eta}\eta}{3} \tag{3.20}$$

$$c_{\eta}\eta = \frac{-1}{\beta\eta_0} \tag{3.21}$$

$$m = 0.5\ [6] \tag{3.22}$$

$$\delta = 1; \qquad \text{if} \nabla \cdot \vec{\boldsymbol{u}} < 0$$

$$\delta = 0; \qquad \text{if} \nabla \cdot \vec{\boldsymbol{u}} > 0$$

The sign of $c_{\epsilon 3}$ changes with the sign of the velocity dilatation (linked through δ) and the polytropic process, thus improving the model. n is the index for a polytropic process, generally taken as 1.4 for engine studies [19]. The RNG k-ϵ model especially addresses the appreciable ratios of turbulent to mean-strain-rate time scales generated due to spray. While the standard version of the k-ϵ model is already present in the simulation code KIVA-3, the RNG version has been specifically implemented in this work.

In general, the k-ϵ models have constants which are geometry- and flow- dependent but can predict the mean velocities in fairly good agreement. It is however important to note that the gradient transport hypothesis is not theoretically sound in all types of turbulent flow [12]. Alternative Reynolds Stress Models are more accurate in predicting energy levels in an anisotropic turbulent flows (flows with swirling and significant streamline curvature) [23]. The RSM model requires a solution of additional 7 equations (6 for the shear stresses on each face of an element and the dissipation term), rendering it highly computing intensive. The RNG k-ϵ model is shown to be particularly suited for IC engines in which sprays cause high strain rates [19].

3.2 Heat Transfer

The mechanism of heat transfer in Diesel engines follows a three-fold mode viz. by conduction in the near wall film, convection in gas phase and radiation in high-temperature and soot-rich regions. Understanding of these modes is important because they influence the efficiency, emissions, knock characteristics as well as component stresses (not addressed in this work). While the convection of heat from free stream to the wall film can be calculated from standard correlations [24], calculating the wall film temperature involves special boundary layer treatment. A traditional way of treating the heat transfer in the boundary-layer based on Reynolds analogy is given in the following section (present in KIVA-3v), while an enhanced treatment for variable-density flows is described in Section 3.2.2.

3.2.1 Near-Wall Heat Transfer

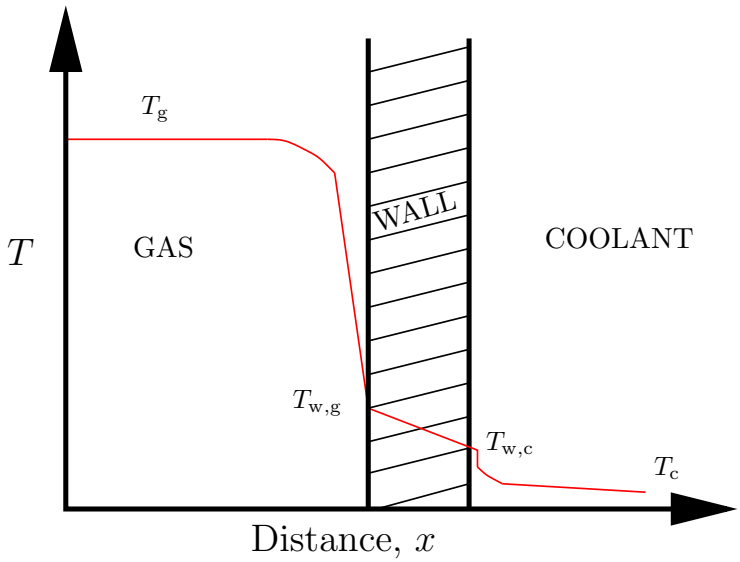

Figure 3.2: Schematic of heat transfer across combustion chamber wall. The steepest resistance to heat transfer (from T_g to $T_{w,g}$) is in the near wall viscous sub-layer.

The Reynolds analogy is used to estimate the turbulent heat flux if the stress, mean velocity and temperature fields are known [25]. Reynolds's analogy assumes that the ratio of turbulent (eddy) diffusivity of flow to turbulent diffusivity of heat is 1. Thus the analogy avoids an explicit statement on the magnitude of the eddy diffusivities. Writing the equation for temperature near the wall with the assumptions as described in Section 3.1.2 and non-dimensionalizing it with the wall temperature T_w we get

$$c_\mu \rho \frac{k^2}{\epsilon} y \frac{\partial T}{\partial y} = \frac{J_w Pr u_w}{c_p \tau_w T_w} = \zeta \quad , \tag{3.23}$$

where ζ is the dimensionless heat loss through the wall and is assumed to be small. A solution of this equation by Taylor series expansion gives

$$\frac{T}{T_w} = 1 + \frac{J_w Pr u_w}{c_p \tau_w T_w} \left(\frac{u}{u_w} + c_0 \right), \tag{3.24}$$

$$c_0 = R_c^{1/2} \left(\frac{Pr_l}{Pr} - 1 \right) \quad . \tag{3.25}$$

Equations 3.24 and 3.25 are used when $yu/\nu_l > R_c$ while the following equation is used when $yu/\nu_l > R_c$:

$$\frac{T}{T_w} = 1 + \frac{J_w Pr_l u_w}{c_p \tau_w T_w} \left(\frac{u}{u_w} \right) \quad . \tag{3.26}$$

3.2.2 Near-Wall Heat Transfer in Variable-Density Flows

The traditional temperature wall functions are derived based on the assumption of a steady-state incompressible flow, the validity of Reynolds analogy and a constant turbulent Prandtl number. Engine flows are characterized by density variations, and the unsteadiness and chemical heat release may invalidate the Reynold's analogy [26, 27]. The Reynolds analogy gives reasonable values for gases where the Prandtl number is roughly one. Experimental investigations also show that the turbulent Prandtl number increases in the buffer and the viscous sublayer [28]. A formulation for variable-density turbulent flows is described here [29], which has been implemented in the KIVA-3 code as part of this work. It is based on the following assumptions:

1. Gradients in the normal direction to the wall are much larger than those in the parallel direction.
2. The fluid velocity is directed parallel to the wall.
3. Pressure gradients, viscous dissipation, enthalpy diffusion effects on energy flux and radiation heat transfer are neglected in the wall region.
4. The fluid follows the ideal gas law.

The general energy conservation equation in 1 dimension can be written as

$$\frac{\partial q}{\partial y} = -\rho c_p \frac{\partial T}{\partial t} + \frac{\mathrm{d}p}{\mathrm{d}t} - Q_\mathrm{c} \quad , \tag{3.27}$$

$$\text{where } q = -\left(k + k_\mathrm{t}\right) \frac{\partial T}{\partial y} \quad . \tag{3.28}$$

Integrating the above equation using relation between conductivity and viscosity and making a quasi-steady state assumption gives

$$-c_p \left(\frac{\mu}{Pr} + \frac{\mu_\mathrm{t}}{Pr_\mathrm{t}} \right) \frac{\mathrm{d}T}{dy} + q_\mathrm{w} + Gy \quad , \tag{3.29}$$

where q_w is the heat flux through the wall and $G = \widetilde{Q_\mathrm{c}}$ is the average chemical heat release. Integrating this equation again will give the required expression for T_w in terms of T, the fluid temperature. To accomplish this, we need correlations describing the changes of Pr_t and ν_t. A curve fit technique taking into account the existing correlations in literature [29] finally give the heat loss as

$$q_\mathrm{w} = \frac{\rho c_p u_\mathrm{w} T \ln\left(T/T_\mathrm{w}\right)}{2.1 \ln\left(y^+\right) + 2.5} \quad , \tag{3.30}$$

where $y^+ = u_\mathrm{w} y/\nu$. The wall velocity is evaluated as described in earlier section of near wall turbulence treatment 3.1.2. This differs from the function described in the previous section, the wall heat flux being proportional to the logarithm to the ratio of flow temperature to the wall temperature as against linearly proportional in previous case. Studies by Han and Reitz [29] have reported that there is a significant impact of compressibility on heat transfer, although the effects of unsteadiness and chemical heat release are negligible.

3.3 Spray

Fuel is introduced into the cylinder in the form of a spray of fuel droplets atomized by a nozzle with a large pressure drop. The pressure at the injector ranges from 200 bar-1700 bar while that inside the cylinder is 50 bar-100 bar [24]. The liquid droplets injected in the cylinder may undergo one or more of the processes viz. collision, break-up or evaporation. The evaporated fuel mixes into the air where finally combustion takes place. Therefore, models are required that describe these four processes (atomization, collision, breakup and evaporation), thereby satisfying the mass, momentum and heat exchange equations. In one class of models, the motion of all droplets is represented via an Eulerian partial differential spray probability equation. In contrast, the discrete dynamic model (DDM) class tracks a "parcel" of droplets in Lagrangian fashion from its origin. Each droplet in a "parcel" is identical and non-interacting. The droplet "parcels" are used continuously throughout the injection process, with a specific initial condition of position, size, velocity, number of droplets with a prescribed distribution, spray angle and temperature.

3.3.1 Mathematical Formulation

The mathematical formulation of the sprays is based on a Monte-Carlo discrete particle technique [30, 31], and consists of a probability distribution functions *f*. The function f has 10 variables listed below:

1. The three spatial coordinates, $\vec{x}$.
2. The velocity components in three directions, $\vec{v}$.
3. The equilibrium radius (radius of a spherical drop only under the force of surface tension), r.
4. The temperature of the droplet T_{D}, assumed uniform within the droplet.
5. The distortion from spherecity, y.
6. The time rate of change of distortion, $\dot{y} = \mathrm{d}y/\mathrm{d}t$.

The distribution function f is defined such that

$$f = f\left(\vec{x}, \vec{y}, r, T_{\mathrm{d}}, y, \dot{y}, t\right) \mathrm{d}\vec{v}\, \mathrm{d}r\, \mathrm{d}T_{\mathrm{d}}\, \mathrm{d}y\, \mathrm{d}\dot{y} \tag{3.31}$$

It is the number of probable droplets per unit volume at position $\vec{x}$ and time t with velocities in the interval $(\vec{v}, \vec{v} + \mathrm{d}\vec{v})$, temperatures in the interval$(T_{\mathrm{d}}, T_{\mathrm{d}} + dT_{\mathrm{d}})$, radius in the interval $(r, r + \mathrm{d}r)$ and distortion parameters in the range $(y, y + \mathrm{d}y)$ and $(\dot{y}, \dot{y} + \mathrm{d}\dot{y})$. The time evolution of the function f is given by:

$$\frac{\partial f}{\partial t} + \nabla_x \cdot (f\boldsymbol{v}) + \nabla_v \cdot (fF) + \frac{\partial}{\partial r}(fR) + \frac{\partial}{\partial r}\left(f\dot{T}_{\mathrm{d}}\right) + \frac{\partial}{\partial y}(f\dot{y})\frac{\partial}{\partial y}(f\ddot{y}) = \dot{f}_{\mathrm{coll}} + \dot{f}_{\mathrm{break}}. \tag{3.32}$$

3.3.2 Atomization

Liquid injection is simulated using the 'blob' injection method of Reitz and Diwakar [32]. In this method, the liquid is introduced at the nozzle exit as 'blobs' with

a characteristic diameter equal to the nozzle exit diameter [33]. The atomization process is a consequence of

1. Inner-nozzle disturbances, mainly due to cavity formation at the sharp nozzle inlet edge, which are responsible for the formation of a fragmented liquid core.
2. Aerodynamic forces which break the liquid fragments into tiny droplets.

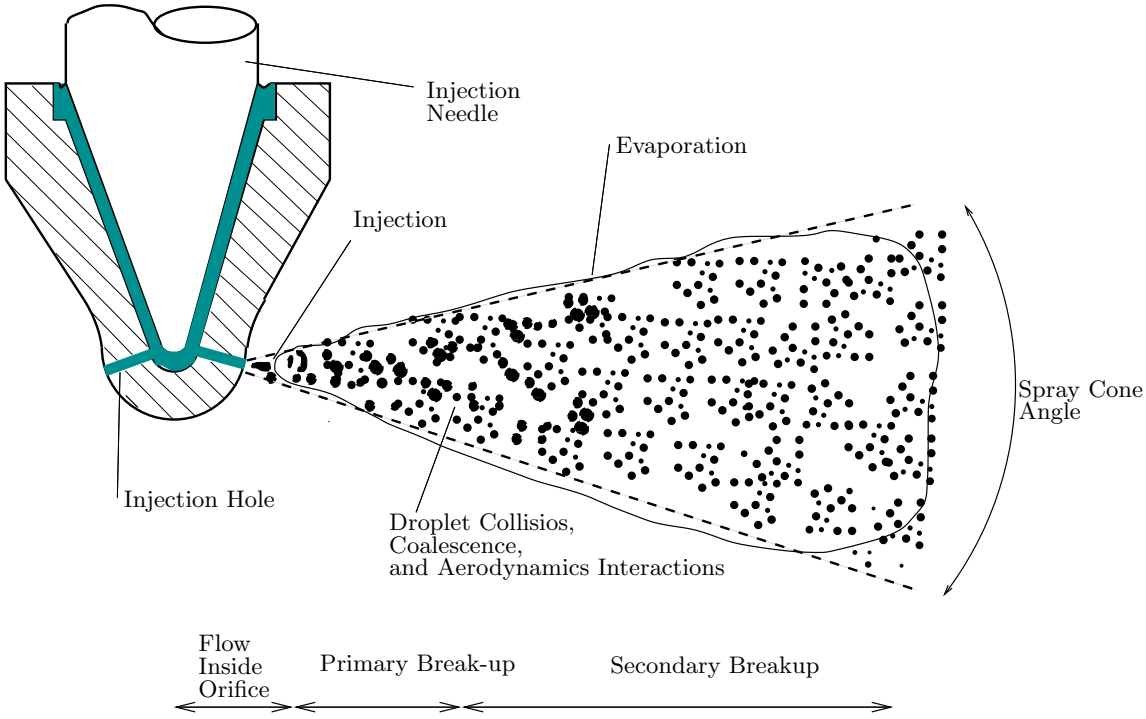

Figure 3.3: Schematic of a spray nozzle showing different flow (collision, coalescence, break-up evaporation) regimes.

The atomization of IC-engine fuel sprays can be divided into two main processes, primary and secondary break-up. The former takes place in the region close to the nozzle at high Weber numbers. It is not only determined by the interaction between the liquid and gaseous phases but also by internal nozzle phenomena like turbulence and cavitation(see Fig. 3.3). Atomization that occurs further downstream in the spray due to aerodynamic interaction processes and is largely independent of the nozzle type is called secondary break-up. The classic break-up models like TAB (Taylor Analogy Break-up), and Wave Breakup based on liquid-jet instability analysis do not distinguish between the two processes. The parameters of these models are usually tuned to match experimental data further downstream in the region of the secondary break-up [35]. Originally, these parameters are supposed to depend only on nozzle geometry, in reality they also account for numerical effects. Other models like ETAB (Enhanced TAB), FIPA (Fractionnement Induit Par Acceleration) or KH-RT(Kelvin-Helmholtz - Rayleigh-Taylor) treat the primary break-up region separately. Hence, they in principle offer the possibility to simulate both break-up processes independently. The correct values for the additional set of parameters, however, are not easy to determine due to the lack of experimental data

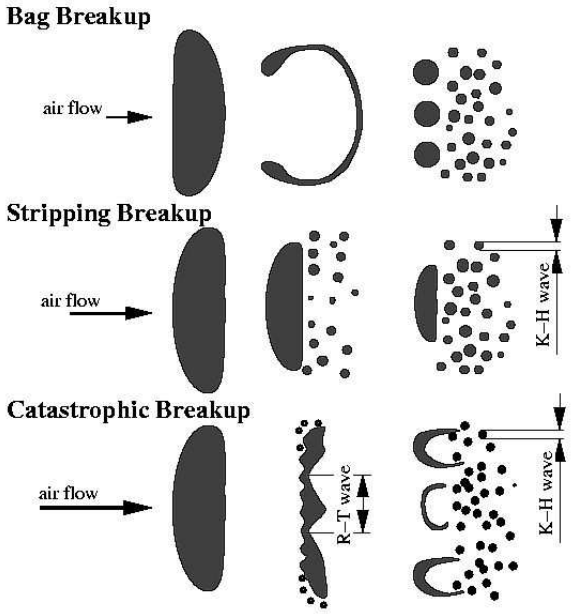

Figure 3.4: Schematic representation of drop breakup mechanisms [34]. *Bag breakup*: $6 < We < 80$, *Stripping (shear) breakup*: $80 < We < 350$, *Catastrophic (surface wave) breakup*: $We > 350$.

for the primary break-up region.

Taylor Analogy Breakup Model
Taylor Analogy Breakup (TAB) Model is based on Taylor's analogy and is a classic method for calculating droplet breakup. [36]. It is summarized as:

1. The drop deformation in terms of the radial cross-section change, x, is described by the forced, damped harmonic oscillator $m\frac{\mathrm{d}^2x}{dt^2} + b\frac{\mathrm{d}x}{\mathrm{d}t} + cx = F$.
2. The forcing term, F, arises from the aerodynamic drag, the restoring force, cx, is given by the surface tension and the damping term, $b\frac{\mathrm{d}x}{\mathrm{d}t}$, is due to the liquid viscosity. Drop breakup occurs when $x > a/2$, where a is the drop radius, which corresponds to $We > We_{\mathrm{crit}} = 6$.
3. The product drop size is determined by an energy consideration which equates the surface, oscillation and radial kinetic energies of the parent and product drops.
4. Shortcomings of TAB model: Not suited for atomization and the product droplet size is underestimated.

Wave Breakup Model
An alternative to the TAB model for high Weber number flows is the Wave breakup model of Reitz [37]. It considers the breakup of droplets induced by the relative velocity between the gas and the liquid phases. It assumes that the time required for breakup and the resulting droplet size is related to the fasted growing

Kelvin-Helmholtz (KH) instability wave, described in following paragraph. Kelvin-Helmholtz instability can occur when velocity shear is present within a continuous fluid or when there is sufficient velocity difference across the interface between two fluids. The theory can be used to predict the onset of instability and transition to turbulent flow in fluids of different densities moving at various speeds. The growth rate of this instability is used to predict the details of the newly formed droplets. The Wave Breakup model is appropriate for high-speed injections where the Weber number is greater than 100 [38]. Liquid breakup is modeled by postulating that new drops with radius r_c are formed from parent drop of radius r such that

$$r_c = B_0 \Lambda_{\mathrm{KH}} \tag{3.33}$$

where B_0 is a constant (=0.61) and Λ_{KH} is the wavelength of the fastest growing frequency of the KH wave, Ω_{KH}. The values of Λ_{KH} and Ω_{KH} is given by:

$$\Lambda_{\mathrm{KH}} = \frac{9.02r\left(1+0.45\sqrt{Z}\right)\left(1+0.4T^{0.7}\right)}{\left(1+0.865We^{1.67}\right)^{0.6}} \tag{3.34}$$

$$\Omega_{\mathrm{KH}} = \frac{0.34+0.38We^{1.5}}{(1+Z)\left(1+1.4T^{0.6}\right)}\sqrt{\frac{\sigma}{\rho_{\mathrm{L}}r^3}} \tag{3.35}$$

where

$$We = \frac{\rho_g u_r^2 r}{\sigma} \qquad \text{Weber Number}$$

$$Z = \frac{\sqrt{We_{\mathrm{L}}}}{Re_{\mathrm{L}}} \qquad \text{Ohnesorge Number}$$

$$Ta = Z\sqrt{We} \qquad \text{Taylor Number}$$

$$We_{\mathrm{L}} = \frac{\rho_{\mathrm{L}} u_r^2 r}{\sigma} \qquad \text{Liquid Weber Number}$$

$$Re_{\mathrm{L}} = \frac{u_r r \rho_{\mathrm{L}}}{\mu_{\mathrm{L}}} \qquad \text{Liquid Reynold's Number}$$

.

The rate of change of the parent drop is described by [32]

$$\frac{\mathrm{d}r}{\mathrm{d}t} = \frac{r-r}{\tau} \tag{3.36}$$

$$\tau = \frac{3.788B_1 r}{\Omega_{\mathrm{KH}}\Lambda_{\mathrm{KH}}} \quad , \tag{3.37}$$

where B_1 is a constant between 10 and 60 [33]. A parametric study of the constant is presented in the results section (7.4). When a sufficient number of new child droplets are created, a new parcel is added to the computation. This is performed when the liquid mass removed from the parent is greater than 3% of the average injected mass and the number of product droplets is greater or equal to the number

of parent drops. The product droplets formed have the same temperature, physical location and velocity (magnitude and direction) as that of the parent. The probability distribution of the broken droplets is given as

$$B = g\left(r\right)\delta\left(T - T_{\mathrm{d1}}\right)\delta\left(y\right)\delta\left(\dot{y}\right)\frac{1}{2\pi}\int\delta\left[\vec{v} - \left(\vec{v_1} + \omega\vec{n}\right)\right]\mathrm{d}\vec{n} \qquad , \tag{3.38}$$

where $g\left(r\right)$ is the size distribution and ω is the magnitude of the velocity of the resulting droplets. The breakup source term in equation 3.32 is given as

$$\dot{f}_{break} = \int f\left(\vec{x}, \vec{v_1}, r_1, T_{\mathrm{d1}}, 1, \dot{y_1}, t\right)\dot{y}B\left(\vec{x}, \vec{v_1}, r_1, T_{d1}, 1, \dot{y_1}, t\right)\mathrm{d}\vec{v_1}\mathrm{d}r_1\mathrm{d}T_{\mathrm{d1}}\mathrm{d}\dot{y_1} \quad . \tag{3.39}$$

The breakup transition probability function B is defined so that $B\,\mathrm{d}\vec{v}\,\mathrm{d}r\mathrm{d}T_{\mathrm{d}}\,\mathrm{d}y\,\mathrm{d}\dot{y}$ is the probable number of droplets with properties in the implied interval that are produced by the breakup of droplet with *subscript* 1 properties. *KH-RT Model*
In diesel sprays, injected droplets have a very high initial velocity. They decelerate quickly due to the drag forces. Any time a dense, heavy fluid is being accelerated/decelerated by a light fluid, the Rayleigh-Taylor (RT) instability can be important [39]. Neglecting the liquid viscosity [40], the fastest growing RT frequency Ω_{RT} and the corresponding wave number K_{RT}(inverse of Frequency) are given as [33]

$$\Omega_{\mathrm{RT}} = \sqrt{\frac{2\left[-g_t\left(\rho_l - \rho_g\right)\right]^{3/2}}{3\sqrt{3\sigma}\left(\rho_l + \rho_g\right)}} \tag{3.40}$$

$$K_{\mathrm{RT}} = \sqrt{\frac{-g_t\left(\rho_l - \rho_g\right)}{3\sigma}} \tag{3.41}$$

$$g_t = \vec{\boldsymbol{g}}\cdot\vec{\boldsymbol{j}} + \vec{\boldsymbol{a}}\cdot\vec{\boldsymbol{j}} \tag{3.42}$$

where $\vec{\boldsymbol{g}}$ and $\vec{\boldsymbol{a}}$ represent the gravity and the droplet acceleration vector while $\vec{\boldsymbol{j}}$ is the unit tangential vector to the droplet trajectory. If the wavelength $2\pi C_{\mathrm{RT}}/K_{\mathrm{RT}}$ is smaller than the droplet diameter, RT waves are considered to be growing on the droplet surface. The time of growth is tracked and compared to the breakup time

$$\tau_{\mathrm{RT}} = \frac{C_\tau}{\Omega_{\mathrm{RT}}} \quad . \tag{3.43}$$

C_τ is a constant assumed to be 1. After the breakup time, the parent droplet is broken into smaller droplet of radius r_{c} such that

$$r_{\mathrm{c}} = \frac{\pi C_{\mathrm{RT}}}{K_{\mathrm{RT}}} \quad , \tag{3.44}$$

where C_{RT} is equal to 0.3. A comparison of the engine simulation results for the two different spray models are presented in the results section (see section 7.4).

3.3.3 Collision

Any two droplets can collide when they are in the a) same numerical mesh or b) same trajectory. In the first case, the collisions are grid dependent. Whenever two droplets collide, they can:

1. Coalesce to give a single droplet. The velocity of the new droplet is calculated using the mass averaging procedure and the size by adding the volumes.
2. No mass and energy transfer takes place, they maintain their sizes and temperatures but undergo only velocity changes.

The collision impact parameter, b, is compared with the critical impact parameter b_{cr} to decide the resultant action of a collision:

$$b_{\mathrm{cr}} = \frac{1}{We}\left[\left(\frac{r_2}{r_1}\right)^3 - 2.4\left(\frac{r_2}{r_1}\right)^2 + 2.7\left(\frac{r_2}{r_1}\right)\right] \quad , \tag{3.45}$$

where the Weber number We is given based on the difference in the velocities;

$$We = \frac{\rho_{\mathrm{L}}\left|\vec{\boldsymbol{v_1}} - \vec{\boldsymbol{v_2}}\right| r_1}{\alpha_{\mathrm{L}}\left(\overline{T}_{\mathrm{L}}\right)} \qquad \text{with} \qquad T_{\mathrm{d}} = \frac{{r_1}^3 T_{\mathrm{L1}} + {r_2}^3 T_{\mathrm{L2}}}{{r_1}^3 + {r_2}^3} \quad , \tag{3.46}$$

where α_{L} is the liquid surface tension. Thus a collision probability density σ can be obtained which gives the probable number of droplets resulting from a collision between drop 1 and drop 2 [41]. It is known from the probability density formulation [41] that the drops with large differences in radius or velocity have a larger probability of collision.

If, however, the second condition of collision, viz. crossing of trajectories, is used, then it is numerically demanding to apply the condition to all pairs of parcels. Impossible collisions can be sorted by verifying two conditions [42]. The first condition is that the parcels have to travel toward each other. The second condition is that the relative displacements of the particles must be larger than the distance between them. If v_1 and v_2 are the velocities of any two parcels under consideration, then the two conditions can be mathematically represented as

$$v_{12} = (v_1 - v_2)\frac{\boldsymbol{x}_2 - \boldsymbol{x}_1}{|\boldsymbol{x}_2 - \boldsymbol{x}_1|} \tag{3.47}$$

$$v_{12}\Delta t > |\boldsymbol{x}_2 - \boldsymbol{x}_1| - (r_1 - r_2) \tag{3.48}$$

Thus, if $\alpha_0 \in [0, \Delta t]$ and $\beta_0 \in [0, \Delta t]$ where α_0 and β_0 are solution to a system

$$\frac{\partial\left|\boldsymbol{p}_2 - \boldsymbol{p}_1\right|}{\partial\alpha, \beta}(\alpha_0, \beta_0) = 0 \tag{3.49}$$

$$\text{where} \qquad \boldsymbol{p}_1 = \boldsymbol{x}_1 + \alpha\boldsymbol{v}_1 \tag{3.50}$$

$$\boldsymbol{p}_2 = \boldsymbol{x}_2 + \beta\boldsymbol{v}_2 \quad , \tag{3.51}$$

then collision will occur if a random number $\xi \in [0, 1]$ is less than P where

$$P = \mathbf{min}\left(1, C_1\frac{r_1 + r_2}{12}\right)e^{-C_2|\alpha_0 - \beta_0|/\Delta t} \quad . \tag{3.52}$$

where$\Delta_{12} = |\boldsymbol{p}_2(\beta_0) - \boldsymbol{p}_1(\alpha_0)|$ is the minimum distance between the two trajectories. $C_1 = 1.0$ and $C_2 = 0.0$ are the model constants [42]. Particles whose trajectories close to each other also have a chance to collide. The difference between α_0 and β_0 gives an estimate of the probability of the collision. This model has also been implemented in the KIVA code and comparative results with respect to the previously described condition (viz. same cell condition) are discussed in Section 7.4.

3.3.4 Evaporation

The atomized droplets of injected liquid fuel gain heat from the surroundings and evaporate as vapor into the bulk gas (air). The vapor pressure and consequently the rate of evaporation increases as the droplet temperature increases due to heat transfer. As the evaporated mass transfers away from the drop, the temperature of the drop decreases [24]. The energy flux on the surface of the droplet with the droplet temperature as the variable can be written as

$$4\pi r^2 \dot{Q}_{\mathrm{d}} = \rho_{\mathrm{d}} \frac{4}{3} \pi r^3 c_{p,l} \dot{T}_{\mathrm{d}} - \rho_{\mathrm{d}} 4\pi r^2 RL\left(T_{\mathrm{d}}\right) \tag{3.53}$$

The heat conduction rate $\dot{Q}_{\mathrm{d}}$ is given by the Ranz-Marshall correlation

$$\begin{aligned} \dot{Q}_{\mathrm{d}} &= \frac{K_{\mathrm{air}}\left(\hat{T}\right)(T - T_{\mathrm{d}})}{2r} Nu_{\mathrm{d}} \\ \text{where} \qquad \hat{T} &= \frac{2}{3} T_d + \frac{1}{3} T \qquad . \end{aligned} \tag{3.54}$$

The convective heat transfer to the droplet is given by the Nusselt number Nu_{d}, where

$$Nu_{\mathrm{d}} = \left(2 + 0.6 Re_{\mathrm{d}}^{1/2} Pr_{\mathrm{d}}^{1/3}\right) \frac{\ln\left(1 + B_{\mathrm{d}}\right)}{B_{\mathrm{d}}} \qquad . \tag{3.55}$$

The Reynolds number Re_{d} is given by;

$$Re_{\mathrm{d}} = \frac{2\rho \left|\vec{u} - \vec{u''} - \vec{v}\right| r}{\mu_{\mathrm{air}}\left(\hat{T}\right)} \tag{3.56}$$

$$\begin{aligned} \mu_{\mathrm{air}}\left(\hat{T}\right) &= \frac{A_1 \hat{T}^{3/2}}{\hat{T} + A_2} \\ A_1 &= 1.457 x 10^{-5} \\ A_2 &= 110 \qquad , \end{aligned} \tag{3.57}$$

the Prandtl number by

$$Pr_{\mathrm{d}} = \frac{\mu_{\mathrm{air}}\left(\hat{T}\right) C_p\left(\hat{T}\right)}{K_{\mathrm{air}}\left(\hat{T}\right)} \tag{3.58}$$

$$K_{\mathrm{air}}\left(\hat{T}\right) = \frac{K_1 \hat{T}^{3/2}}{\hat{T} + K_2} \tag{3.59}$$

$$K_1 = 252$$

$$A_2 = 200$$

and the Spalding transfer number by

$$Br_{\mathrm{d}} = \frac{Y_1^* - Y_1}{1 - Y_1^*} \quad . \tag{3.60}$$

The Spalding number represents the gradients at the droplet surface. Y_1 is the mass fraction of the fuel in the gas phase, the mass fraction on the surface Y_1^* is given as

$$Y_1^*\left(T_{\mathrm{d}}\right) = \frac{M_1}{M_1 + M_0\left(\frac{p}{p_{\mathrm{v}}\left(T_{\mathrm{d}}\right)} - 1\right)} \quad , \tag{3.61}$$

where M_1 is the molar mass of the fuel, M_0 is the mean molar mass without the fuel and $p_{\mathrm{v}}\left(T_{\mathrm{d}}\right)$ is the equilibrium vapor pressure. Therefore, the heat conduction rate $\dot{Q}_{\mathrm{d}}$ can be calculated using equation(3.55). The latent heat in equation (3.53) is given by

$$L\left(T_{\mathrm{d}}\right) = E_1\left(T_{\mathrm{d}}\right) + \frac{RT_{\mathrm{d}}}{M_1} - E_1\left(T_{\mathrm{d}}\right) - \frac{p_{\mathrm{v}}\left(T_{\mathrm{d}}\right)}{\rho_d} \quad . \tag{3.62}$$

R represents the rate of change of the droplet radius and is given by the Frossling correlation:

$$R = -\frac{(\rho D)_{\mathrm{air}}\left(\hat{T}\right)}{2\rho_{\mathrm{d}} r} B_{\mathrm{d}} Sh_{\mathrm{d}} \tag{3.63}$$

$$Sh_{\mathrm{d}} = \left(2 + 0.6 Re_{\mathrm{d}}^{1/2} Sc_{\mathrm{d}}^{1/3}\right) \frac{\ln\left(1 + B_d\right)}{B_{\mathrm{d}}} \tag{3.64}$$

$$\text{where} \qquad Sc_{\mathrm{d}} = \frac{\mu_{\mathrm{air}}\left(\hat{T}\right)}{\rho D_{\mathrm{air}}\left(\hat{T}\right)} \quad .$$

3.3.5 Acceleration and Drag

The droplet acceleration term has contributions from the gravitational acceleration and aerodynamic drag. The total force F is, assuming that the droplet remains

spherical is given as

$$F = \frac{3}{8}\frac{\rho}{\rho_{\mathrm{L}}}\frac{\left|\vec{\boldsymbol{u}}+\vec{\boldsymbol{u}''}-\vec{\boldsymbol{v}}\right|}{r}\left(\vec{\boldsymbol{u}}+\vec{\boldsymbol{u}''}-\vec{\boldsymbol{v}}\right)C_{\mathrm{D}}+\vec{\boldsymbol{g}} \tag{3.65}$$

$$\text{where} \quad C_{\mathrm{D}} = \frac{24}{Re_{\mathrm{L}}}\left(1+\frac{1}{6}Re_{\mathrm{L}}^{2/3}\right) \quad \text{for } Re_{\mathrm{L}}<1000$$

$$= 0.424 \quad \text{for } Re_{\mathrm{L}}>1000 \tag{3.66}$$

However, as the drop moves through the gas, its shape is altered significantly when the Weber number is large. The dynamics drag model accounts for the effects of the droplet shape distortion and is given by the equation;

$$C_{\mathrm{D}} = C_{\mathrm{D,sphere}}\left(1+2.632y\right) \tag{3.67}$$

where y is the droplet distortion as determined by the solution of

$$\frac{\mathrm{d}^2y}{\mathrm{d}t^2} = \frac{C_{\mathrm{F}}}{C_{\mathrm{b}}}\frac{\rho_{\mathrm{G}}}{\rho_{\mathrm{L}}}\frac{u^2}{r^2} - \frac{C_{\mathrm{k}}\sigma}{\rho_L r^3}y - \frac{C_{\mathrm{d}}\mu_{\mathrm{L}}}{\rho_{\mathrm{L}}r^2}\frac{\mathrm{d}y}{\mathrm{d}t} \tag{3.68}$$

In the case of no distortion ($y=0$), the drag coefficient of a sphere will be obtained while at maximum distortion, the drag coefficient corresponding to a disc will be obtained.

3.3.6 Gas - Spray Interaction Terms

The spray (discrete) phase gives rise to source terms, which are added to the equations of the gas phase. These terms are listed as;

$$\overline{\rho\dot{Y}_i^{\mathrm{S}}} = -\int f\rho_{\mathrm{d}}4\pi r^2R\cdot\mathrm{d}\vec{v}\cdot\mathrm{d}r\cdot\mathrm{d}T_{\mathrm{d}}\cdot\mathrm{d}y\cdot\mathrm{d}\dot{y}$$

$$\overline{\vec{F}^{\mathrm{S}}} = -\int f\rho_{\mathrm{d}}\left(4/3\pi r^3\vec{F}+4^2R\vec{v}\right)\cdot\mathrm{d}\vec{v}\cdot\mathrm{d}r\cdot\mathrm{d}T_{\mathrm{d}}\cdot\mathrm{d}y\cdot d\dot{y}$$

$$\overline{\dot{Q}^{\mathrm{S}}} = -\int f\rho_{\mathrm{d}}\left[4\pi r^2R\left[E_1\left(T_{\mathrm{d}}\right)+\frac{1}{2}\left(\vec{v}-\vec{u}\right)\frac{4}{3}\pi r^3\left[c_{p,L}\dot{T}_{\mathrm{d}}+\vec{F}\left(\vec{v}-\vec{u}-\vec{u''}\right)\right]\right]\right]\cdot \mathrm{d}\vec{v}\cdot\mathrm{d}r\cdot\mathrm{d}T_{\mathrm{d}}\cdot\mathrm{d}y\cdot\mathrm{d}\dot{y}$$

$$\overline{\dot{W}^{\mathrm{S}}} = -\int f\rho_{\mathrm{d}}\frac{4}{3}\pi r^3\vec{\boldsymbol{F}}\vec{u''}\cdot\mathrm{d}\vec{v}\cdot\mathrm{d}r\cdot\mathrm{d}T_{\mathrm{d}}\cdot\mathrm{d}y\cdot\mathrm{d}\dot{y}$$

.

3.4 Radiation

The emission and absorption of electromagnetic waves (in the visible and infrared wavelengths) from hot surfaces is responsible for radiative heat transfer. In an IC engine, heat is transferred radiatively from the high temperature combustion gases and the particulate cloud in the flame region to the chamber walls. Soot in the flame region is the cause of the particulate clouds, and is insignificant in

the spark ignited engines [24], but forms substantial part of the total radiation in Diesel engines. Radiation does not contribute any terms to the mass and momentum balance equations. The heat flux term in the energy equation 2.32 will have a term due to radiation and thus becomes

$$J = -K\Delta T + \vec{\boldsymbol{F}} - \rho D \sum_i h_i \Delta\left(\frac{\rho_i}{\rho}\right) \qquad . \tag{3.69}$$

$\vec{\boldsymbol{F}}$ is the radiation heat flux vector, and its divergence need to be determined to solve the energy equation. The radiative transfer equation (RTE), forming the the basis of the solution, is derived by an energy balance over a small elementary volume taken along the direction of a small pencil of electromagnetic radiation, confined in a solid angle [43]. The governing variable of such an equation is the spectral intensity I_λ and is defined as the energy emitted per unit time per unit wavelength interval around λ, per unit projected surface area. The projected surface area is normal to the direction of propagation $\vec{\Omega}$ into a unit elemental solid angle centered around the direction $\vec{\Omega}$. The balance equation for spectral intensity is give as [43]

$$\left(\vec{\nabla}\cdot\vec{\Omega}\right) = -k_{\mathrm{a},\lambda} I_\lambda + k_{\mathrm{s},\lambda} I_\lambda + k_{\mathrm{a},\lambda} I_{\mathrm{b},\lambda} + \frac{k_{\mathrm{a},\lambda}}{4\pi}\int P\left(\Omega', \Omega\right) I_\lambda \, \mathrm{d}\Omega' \qquad . \tag{3.70}$$

The term on the left-hand side is the gradient of the intensity. The first two terms on the right-hand side represent attenuation of the directional intensity due to absorption (coefficient = $k_{\mathrm{a},\lambda}$) and out-scattering (coefficient = $k_{\mathrm{s},\lambda}$). $I_{\mathrm{b},\lambda}$ is the blackbody intensity contribution to the total intensity and is represented by the third term. In-scattering from surrounding medium contributes via the fourth term harnessed by the probability $P\left(\Omega, \Omega'\right)$. It represents the probability of the radiation propagating in the direction Ω' being scattered into direction Ω. For typical soot particle diameters between 30nm-65 nm, scattering of intensity is negligible compared to absorption which can be shown by Mie theory [44, 45]. Such scattering is important where the particle sizes are large e.g. pulverized coal, fly ash etc. Assuming a scattering coefficient $k_{\mathrm{s},\lambda}$ equal to zero eliminates the second and the fourth term.

The direction of propagation Ω can be expressed in terms of its direction cosines viz. (ζ, η, μ) where

$$\zeta = \sin\theta\cos\phi \quad \eta = \sin\theta\sin\phi \quad \mu = \cos\theta \qquad .$$

The RTE thus reduces to

$$\mu\frac{\partial I_\lambda}{\partial x} + \eta\frac{\partial I_\lambda}{\partial y} + \zeta\frac{\partial I_\lambda}{\partial z} = -k_{\mathrm{a},\lambda} I_\lambda + k_{\mathrm{a},\lambda} I_{\mathrm{b},\lambda} \qquad . \tag{3.71}$$

After obtaining the distribution of the intensity as a function of the spatial coordinates, the solid angle and the wavelengths, the divergence of the radiative flux vector is obtained from

$$\nabla\cdot\vec{F} = \int_0^\infty k_{\mathrm{a},\lambda}\left[4\pi I_{\mathrm{b},\lambda} - G_\lambda\right]\mathrm{d}\lambda \qquad \text{where } G_\lambda = \int_{\Omega=0}^{4\pi} I_\lambda \mathrm{d}\Omega \qquad . \tag{3.72}$$

The first and second terms in the integral represents the local rate of emission and absorption respectively. G_λ is the irradiance obtained by integrating the intensity over all directions. The extent of absorption of radiation depends on the optical thickness of the medium. An optically thin medium absorbs negligible radiation and in such a situation, G_λ can be assumed to be zero. Consequently, the energy equation can be simplified to eliminate its dependence on the intensity I_λ,

$$\nabla \cdot \vec{\boldsymbol{F}} = \int_0^\infty 4\pi k_{\mathrm{a},\lambda} I_{\mathrm{b},\lambda} \, \mathrm{d}\lambda \qquad . \tag{3.73}$$

Black body radiation intensity $I_{\mathrm{b},\lambda}$ is a function only of the temperature, eliminating the need for solving the RTE. The assumption of optically thin medium overestimates the radiative heat loss [46] in the medium because re-absorption of radiation is neglected. Determination of optical thickness requires the values of the absorption coefficient $k_{\mathrm{a},\lambda}$ for all radiating species. Optical thickness is give by

$$X_\lambda = k_{\mathrm{a},\lambda} L_{\mathrm{e}} \qquad , \tag{3.74}$$

where L_{e} is the beam length. The beam length of an array depends on its wavelength but a mean beam length can also be defined [47]. However, to calculate the optical thickness, its necessary to determine the absorption coefficients of all species. Absorption coefficients are highly temperature-dependent, which in turn cannot be determined accurately without a radiation model. Determination of radiative properties to solve the radiation equation are discussed in the next section.

The radiation model, its solution method and testing of the method for an standalone example problem (box furnace) is described in a previous work [48]. Only general remarks are made regarding the solution procedure in the following section. The radiation algorithm was however not implemented into the KIVA code previously. It has been implemented in this work with suitable tailoring for 1-step chemistry as well as 1- and 2-rpv ILDM chemistry cases with an option to choose optically thick or thin medium. Results of simulation for with and without radiation are compared in the results Chapter 7.

3.4.1 Radiation Properties of Species

Soot, water and carbon-dioxide are strong absorbers and emitters of radiation. Their radiation properties depend on the wavelength of radiation, but more importantly are affected by the accuracy in prediction of their concentrations/sizes. The radiation property prediction method has to be compatible with the chemistry, turbulence and the radiation model used to solve the RTE. Flame radiation can be classified into luminous and non-luminous. Non-luminous radiation is produced by various transitions in the vibrational-rotation energy states of molecules. It is concentrated in the gaseous absorption bands in the infrared spectrum. In a luminous flame, radiation is in the visible and infrared spectrum, such as that due to soot particles [49].

Radiation due gases: Analysis of each discrete absorption-emission line in a spectrum of energy level transitions can be prohibitive. In reality, the spectral lines are pressure-broadened, giving rise to bands. Narrow-band models (NBM) describe the emissivity over a small wavelength range of each band [50]. Narrow-band methods and line-by-line methods are accurate but prohibitive in computational effort due to the requirement of solution of the RTE several hundreds of time [51]. They have been reportedly used in simpler laminar flame calculations [52, 53]. The exponential wide band model (EWBM) [54] involves dividing the spectrum into wider bands with an exponential variation of the spectral quantities in the band. Although it requires less data points, the number of instances of solving the RTE are still fairly high, with a minimum of 11 [51] for a time step. An unsteady-state simulation like that in a Diesel engine would entail unacceptable computer time.

A simplifying assumption would be to consider the gases as gray. The concomitant result is that the radiative properties become independent of the wavelengths and can be calculated by co-relation comparison with detail models [55]. It is the optimum way in terms of accuracy and solution time. The WSGGM model is one such model where the total emissivity of a non-gray gases is represented as the **W**eighted **S**um of a small number of **G**rey **G**ases (and hence the name) [56]. The emissivity is given as

$$\epsilon = \sum_{i=1}^{N_g} w_i \left(T\right) \left(1 - \exp\left[-k_{i,p} p L_e\right]\right) \quad , \tag{3.75}$$

where $k_{i,p}$ are the constant coefficients, p is the partial pressure of the radiating gas, L_e is the beam length and w_i are the weights as a function of temperature given by

$$w_i = \sum_{j=1}^{J} b_{i,j} T^{j-1} \quad . \tag{3.76}$$

N_g is the total number of absorption bands or gray gases, into which the emission-absorption spectrum is divided, each with a corresponding absorption coefficient ($k_i = k_{i,p} p$). Each band emits a fraction of the total spectrum of a blackbody radiation. This fraction is the weighting factor w_i. The RTE is solved for each of these bands. The total intensity over the entire spectrum can be obtained by summing the individual contributions of all the bands or gray gases. Thus,

$$I = \sum_{i}^{N_g} I_i \quad . \tag{3.77}$$

The total blackbody intensity is given by

$$I_\mathrm{b} = \frac{\sigma}{\pi} T^4 \quad . \tag{3.78}$$

where σ is the Stefan-Boltzmann's constant. Typical values of the absorption coefficient $k_{i,p}$ and the polynomial coefficients $b_{i,j}$ for determining w_i are given in Table 3.4.1 for two different ratios of H_2O-CO_2 partial pressures

$\frac{p_w}{p_c} = 1.0$					
i	$k_{i,p}$	$b_{i,1} \times 10^1$	$b_{i,2} \times 10^4$	$b_{i,3} \times 10^7$	$b_{i,4} \times 10^{11}$
1	0.4303	5.150	-2.303	0.9779	-1.494
2	7.055	0.7749	3.399	-2.297	3.770
3	178.1	1.907	-1.824	0.5608	-0.5122
$\frac{p_w}{p_c} = 2.0$					
i	$k_{i,p}$	$b_{i,1} \times 10^1$	$b_{i,2} \times 10^4$	$b_{i,3} \times 10^7$	$b_{i,4} \times 10^{11}$
1	0.4201	6.508	-5.551	3.029	-5.353
2	6.516	-0.2504	6.112	-3.882	6.528
3	131.9	2.718	-3.118	1.221	-1.612

Table 3.3: WSGGM absorption and polynomial coefficients.

Radiation due to soot: Soot emissivity can be accurately predicted if the size distribution, shape and optical properties of soot particles is known. Mie theory, [44] based on the exact solution of Maxwell's equations for scattering of incident wave on a sphere, is the commonly used model for such predictions. In the limit of a very small size parameter α (i.e. $\alpha << 1$), Mie theory is reduced to the Rayleigh limit, and the absorption coefficient is given by [49]

$$k_{\text{soot},\lambda} = \frac{36\pi n\kappa}{\left(n^2 - \kappa^2 + 2\right)^2 + 4n^2\kappa^2} \frac{f_{\text{v}}}{\lambda} \qquad , \tag{3.79}$$

where n and κ are optical constants. Emission of radiation from soot is independent on the wavelength [57]. An appropriate choice of n and κ can be used to simplify the above equation to [58]

$$k_{\text{soot},\lambda} = \frac{C_0}{\lambda} f_{\text{v}} \qquad , \tag{3.80}$$

where C_0 is a constant. To obtain the gray-soot absorption coefficient, above equation is integrated over the entire spectrum of wavelengths by

$$k_{\text{soot}} = \frac{1}{\sigma T^4} \int_0^\infty k_{\text{soot},\lambda}\, e_{\text{b},\lambda}\, d\lambda = 3.6\, \frac{C_0}{C_2}\, f_{\text{v}} T \qquad , \tag{3.81}$$

where $e_{\text{b},\lambda}$ is the black body emissivity and C_2 is the Planck's second constant (=1.4388 cmK). The suggested value of C_0 is 4.64 [59]. Reports in literature show very good agreement between the detail wavelength dependent calculations and the above method [60]. The emissivity can then be obtained by

$$\epsilon_s = 1 - \exp\left(-k_{\text{soot}} L_{\text{E}}\right) \quad . \tag{3.82}$$

3.4.2 Solution of the RTE

Flux methods of solution of the RTE offer high degree of accuracy [61] and are widely used in combustion calculations. Radiative intensity depends on the angles

of transmission and results in the complexity associated with the solution of RTE. The angular dependence, when separated from the spatial dependence, simplifies the solution procedure. If the intensity is assumed uniform on a given interval of solid angle, then the RTE reduces to a series of linear coupled ODEs. Two such commonly used flux methods are the discrete ordinates method (DOM) [62] and the spherical harmonics method [63]. The DOM is an accurate and efficient method for combustion calculations [64, 65, 66, 67, 68, 69].

The solid angle of 4π around a point is divided into several sectors. The size of each sector is determined from quadrature schemes. The transport equation is then solved for this set of discrete directions, represented by its direction cosines, spanning the total solid angle. The solution procedure, its validation and testing is given in previous work [48]. In the present work, this method is implemented in the KIVA code for radiation calculations in Diesel engine. Since in this work better soot predictions are reported than in the previous work, some effect of radiation is expected. A comparison is given in the Section 7.7 for both thin optical medium (NO RTE solved) and thick optical medium with 4 discrete ordinates. The mean absorption and emission coefficients are calculated by integrating them over PDFs of T, ξ and reaction progress variables similar to other source terms.

Chapter 4

Chemistry Models

4.1 Chemistry

Modeling of combustion requires the knowledge of elementary reactions making up the global reaction, molecularity & order of reactions, rates of reactions and its temperature and pressure dependence. All of this information is incorporated in a reaction mechanism. A solution of the equations governing a mechanism can give us valuable outcome such as product concentrations, temperature profiles and heat released. Therefore, detailed information about reaction kinetics is essential for any combustion model. The solution to a system of reactions also requires thermodynamic data, equilibrium constants, and physical properties of species [70]. The chemistry of a system can be modeled using any of the following approaches;

4.1.1 Simplified Chemistry Modeling

The most common practice is to assume that the combustion process can be described by a single reaction of the form

$$\text{Fuel} + \text{Oxidizer} \longrightarrow \text{Products} \quad , \tag{4.1}$$

and the rate of the reaction is given by an Arrhenius equation of the form

$$Rate_{\text{fuel}} = A\rho^2 \left[Fuel\right]^a \left[Oxidizer\right]^b \exp\left(-\frac{E_{\text{A}}}{\tilde{R}T}\right) \quad , \tag{4.2}$$

where $Rate_{\text{fuel}}$ is the rate of disappearance of unburned fuel, $\tilde{R}$ is the universal gas constant, a, b, A and E_{A} are the order of reaction, pre-exponential coefficient and activation energy. This approach assumes that the complex hydrocarbon fuel oxidation can be adequately represented by a single (or few) overall reactions. No intermediate species concentrations can be calculated. It also uses local average values of concentrations and temperatures to calculate local reaction rates. (In reality, the instantaneous values determine the reaction rate.) The burning rate is made strongly dependent on the chemical kinetics and the influence of turbulence is neglected. Moreover, the parameters in the equation need to be adjusted to each individual engine design specifications to fit the experimental data.

An alternative, but equally simple approach is to assume that turbulent mixing is the rate-limiting factor while the kinetics are infinitely fast. The reaction rate is assumed to be inversely proportional to the turbulent mixing time ($\approx k/\epsilon$). A common way to assimilate both these approaches is to select the lower rate of the two and use it to calculate the burning rate.

4.1.2 Equilibrium Chemistry Modeling

Equilibrium is said to have occurred when the species concentration do not change with time. Equilibrium composition is found by minimization of the free energy of the system. The equilibrium approach assumes that the reacting species and the products reach their equilibrium values as soon as mixing is complete. Thus, the only description required is that of the process of mixing. Assuming equal diffusivity of all species simplifies mixing calculations. Instead of the species, mixing of the elements is tracked, since their concentrations are unchanged during the course of the reaction. For this reason, a mixture fraction ξ is defined such that [70]

$$\xi = \frac{Z_i - Z_{i,\text{fuel}}}{Z_{i,\text{oxidizer}} - Z_{i,\text{fuel}}} \quad , \tag{4.3}$$

where Z_i denotes the mass fraction of element i. The mass fraction is the ratio of the given element i to that of the total mass. A conservation equation for the mixture fraction ξ can be written in a fashion similar to Equation 2.4. After Favre averaging, the same equation transforms to

$$\frac{\partial \overline{\rho}\tilde{\xi}}{\partial t} + \nabla \cdot \left(\overline{\rho}\tilde{\vec{u}}\tilde{\xi}\right) = \nabla \cdot \left(\rho D_{\text{T}} \nabla \tilde{\xi}\right) + \overline{\rho \dot{\xi}^{\text{S}}} \quad , \tag{4.4}$$

where the last term is the source of mixture fraction due to spray. This equation has no chemical source terms because ξ is a conserved scalar. If ξ is defined using the element C, the source due to spray is

$$\overline{\rho \dot{\xi}^{\text{S}}} = \overline{\dot{\rho}^{\text{S}}} Z_{\text{C,Fuel}} \quad . \tag{4.5}$$

If the system under consideration is under adiabatic operating conditions, then its enthalpy h is also a conserved quantity. It can be uniquely determined from ξ. In a non-adiabatic system, such as a Diesel engine, all scalar variables are unique functions of the mixture fraction and enthalpy. And they can be defined through the equilibrium relationship [70] obtained by minimization of the Gibbs free energy of the system. The chemistry and heat source terms in Equations 2.5 and 2.13 can be calculated for a time step δt as

$$\dot{\rho}^{\text{C}} = \left(\rho_i^{\text{eq}} - \rho_i^{\text{old}}\right)/\Delta t \tag{4.6}$$

$$\dot{Q}^{\text{C}} = -\sum_i \dot{\rho}_i^{\text{C}} \left(\Delta h_{\text{f}}^0\right)_i \quad . \tag{4.7}$$

4.1.3 Detail Chemistry Modeling

A reaction mechanism is a collection of elementary reactions. An elementary reaction is one that occurs exactly as it is represented by a reaction equation. Unlike

global or complex reactions, it cannot be further broken down into constituent reactions. The reaction mechanisms describe how a reaction takes place at the molecular level, which bonds are broken or formed and in which order, and what the relative rate of the steps are. Therefore, the understanding of properties of reactants and products is required [71].

Each step of the mechanism involves re-arrangement or combinations of molecular species. The interaction of these steps produce the overall balanced stoichiometric chemical equation of the global reaction. For a mechanism to be considered valid, its sum must equal the overall balanced equation, its predictions of intermediates must not be contrary to experimental observations and its predicted rate law must agree with experimental data. Since a set of elementary reactions makes up the detail reaction mechanism, such a set can be represented as

$$\sum_i a_i^r x_i \rightleftharpoons \sum_i b_i^r x_i \quad , \tag{4.8}$$

where x_i is the mole fraction of species i, and a and b are the integral stoichiometric coefficients of species i in reaction r. The rate of this reaction $\dot{\omega}_r$ is given by

$$\dot{\omega}_r = k_\mathrm{f} \prod \left(\rho_i / M_i\right)^{a_i^r} - k_\mathrm{b} \prod \left(\rho_i / M_i\right)^{b_i^r} \quad . \tag{4.9}$$

The forward and backward reaction rates k_f and k_r are assumed to be in the Arrhenius form,

$$k_\mathrm{f} = A_\mathrm{f} T^{n,\mathrm{f}} \exp\left(\frac{-E_\mathrm{f}}{R_0 T}\right) \quad , \tag{4.10}$$

$$k_\mathrm{b} = A_\mathrm{b} T^{n,\mathrm{b}} \exp\left(\frac{-E_\mathrm{b}}{R_0 T}\right) \quad , \tag{4.11}$$

where A is the pre-exponential factor, n is the temperature exponent and E is the activation energy. Now, the source terms for Equation 2.5 and 2.13 can be calculated as

$$\dot{\rho}_i^\mathrm{C} = M_i \sum_i \left(b_i^r - a_i^r\right) \dot{\omega}_r \quad , \tag{4.12}$$

$$\dot{Q}^\mathrm{C} = \sum_r \dot{\omega}_r \sum_i \left(b_i^r - a_i^r\right) \left(\Delta h_\mathrm{f}^0\right)_i \quad . \tag{4.13}$$

4.2 Heptane Oxidation Chemistry and Mechanism

There are a number of detailed [72, 73, 74, 75] and reduced [76, 77] oxidation mechanisms available, describing the reaction path of heptane oxidation under various pressure and temperature conditions. These mechanisms were derived by building upon the mechanism of lower alkanes/alkenes (up to C_4-species). A detailed mechanism captures various characteristic phenomenon of combustion such as autoignition, negative temperature coefficient (NTC) regime, accelerated reaction rates

due to chain-branching at high temperatures etc. A brief description in terms of the classes of reactions in the mechanism, divided into two temperature regimes is given below. It is based on the work of Westbrook et al. [75]. This description is followed by an explanation about the process by which the mechanism used in the present ILDM treatment in this worked was arrived at. The mechanism for high temperatures were developed first. However, these mechanisms could not explain phenomenon like engine knock. Further investigations led to the development of the low temperature mechanisms. Therefore the high-temperature mechanism is discussed first. Together with the $H_2/O_2/CO$ subsystem, the C_1/C_2 subsystem, the C_3/C_4 subsystem, they constitute the detail mechanism. The $H_2/O_2/CO$ subsystem, the C_1/C_2 subsystem, the C_3/C_4 subsystem is well documented [70] with the sources of rate parameters and verified [71].

4.2.1 High-Temperature Oxidation

The oxidation at high temperature starts with the unimolecular decomposition of heptane to give either one of the four possible heptyl radicals and one H radical (high activation energy path because C-H bond has higher energy than C-C bond) or two of the 6 possible alkyl radicals. The 4 possibilities of heptyl radical are due to the 4 possible scission sites. Only one example for each is given below:

$$\begin{aligned} C_7H_{16} &\rightleftharpoons 1\text{-}C_7H_{15} + H \\ C_7H_{16} &\rightleftharpoons nC_3H_7 + 1\text{-}C_4H_9 \quad . \end{aligned}$$

H atom abstraction can take place at any of the 4 carbon sites again giving one of 4 possible heptyl radicals and H_2. For example:

$$C_7H_{16} + H \rightleftharpoons 1\text{-}C_7H_{15} + H_2 \quad .$$

Alkyl radical decomposition splits the radicals formed in step 1 via β scission (scission at β carbon atom) to give smaller alkyl radicals and alkenes. For example:

$$C_7H_{15} + H \rightleftharpoons 1\text{-}C_4H_9 + C_3H_6 \quad .$$

Addition of alkyl radicals to molecular oxygen to give HO_2 and an olefin. This reaction proceeds through several intermediate steps involving species of type RO_2 (alkylperoxide) and QOOH (alkenyl-hydroperoxide), where R is an alkyl radical while Q is an alkenyl radical.

$$C_3H_7 + H \rightleftharpoons 1\text{-}C_3H_6 + HO_2 \quad .$$

Alkyl radicals can undergo internal H atom transfer to give an isomer of the alkyl radical.

$$1\text{-}C_7H_{15} + H \rightleftharpoons 3\text{-}C_7H_{15} \quad .$$

Alkyl radicals can undergo rapid decomposition via elimination of an olefin molecule. Smaller olefin species are important in all combustion systems. At high temperatures, alkyl radicals decompose to smaller olefins, while at low temperatures, the RO_2 reaction path can give small quantities of larger olefins.

$$4\text{-}C_7H_{15} \rightleftharpoons C_2H_5 + 1\text{-}C_5H_{10} \quad .$$

Addition of OH and O radicals to large olefin at the double bonds:

$$4\text{-}C_7H_{14} + O \rightleftharpoons C_7H_{13} + OH \quad .$$

Decomposition of alkenyl radicals to olefins and allyl radicals:

$$4\text{-}C_7H_{13} \rightleftharpoons C_4H_7 + C_3H_6 \quad .$$

Olefin decomposition:

$$2\text{-}C_7H_{14} \rightleftharpoons C_4H_7 + n\text{-}C_3H_7 \quad .$$

4.2.2 Low-Temperature Oxidation

At temperatures lower than about 900-1000 K, high activation energies of the β scission makes these processes slower. Under such conditions, most important reaction is the addition of molecular oxygen to alkyl radical to give alkylperoxy radical. This leads to a host of channels for further progress (H atom abstraction, subsequent decomposition to give 2 hydroxyl radicals and a carbonyl, second addition of O_2, or reactions involving tens of species.

The first addition of O_2 is the most important reaction at low temperatures. As an example:

$$1\text{-}C_7H_{15} + O_2 \rightleftharpoons 1\text{-}C_7H_{15}O_2 \quad .$$

Disappearance of the chain-branching agent at higher temperatures leads to an inverse temperature dependence of the overall reaction rate, termed as the "negative temperature coefficient".

Alkyl radical addition to an alkylperoxy radical to give two alkyloxide radicals:

$$1\text{-}C_7H_{15} + 1\text{-}C_4H_9O_2 \rightleftharpoons 1\text{-}C_7H_{15}O + 1\text{-}C_4H_9O \quad .$$

Isomerization of the alkylperoxy radical by internal H atom abstraction to form one of the 18 possible [75] alkenyl-hydroperoxide radicals.

$$1\text{-}C_7H_{15}O_2 \rightleftharpoons 1\text{-}C_7H_{14}OOH \quad .$$

The above path dominates in practical conditions and no distinct acceleration of ignition process can be seen as a result of first addition of O_2.

Reaction of alkylperoxy radicals with HO_2:

$$1\text{-}C_7H_{15}O_2 + 1\text{-}HO_2 \rightleftharpoons 1\text{-}C_7H_{15}O_2H + O_2 \quad .$$

Reaction of alkylperoxy radicals with hydrogen peroxide:

$$1\text{-}C_7H_{15} + 1\text{-}H_2O_2 \rightleftharpoons 1\text{-}C_7H_{15}O_2H + O_2 \quad .$$

It converts one stable species and a peroxy species into another stable species and another peroxy species.

Conversion of peroxy radicals to other fast decomposing radicals:

$$1\text{-}C_7H_{15}O_2 + 1\text{-}CH_3O_2 \rightleftharpoons 1\text{-}C_7H_{15}O + CH_3O + O_2 \quad .$$

Reaction of two alkylperoxy radicals to give alkoxy radicals:

$$1\text{-}C_7H_{15}O_2 + 1\text{-}C_4H_9O_2 \rightleftharpoons 1\text{-}C_7H_{15}O + 1\text{-}C_4H_9O + O_2 \quad .$$

Alkoxy radical produced in the oxidation process are unstable and undergo decomposition readily. Large alkoxy radicals decompose to smaller oxygenated species, primarily aldehydes or ketones, together with an alkyl species:

$$1\text{-}C_7H_{15}O \rightleftharpoons C_6H_{14} + CH_2O \quad .$$

Reactions of alkenyl hydroperoxides to give a) olefins & HO_2 or b) olefins plus carbonyl radicals or c) addition of O_2 or d) alkenoxy radicals or e) isomerization to ketohydroxyperoxide or f) ketohydroxyperoxide decomposition:

$$\begin{aligned}
1\text{-}C_7H_{14}OOH &\rightleftharpoons 1\text{-}C_7H_{14} + HO_2 \\
1\text{-}C_7H_{14}OOH &\rightleftharpoons 1\text{-}C_4H_9CHO + C_2H_4 + OH \\
1\text{-}C_7H_{14}OOH + O_2 &\rightleftharpoons O_2C_7H_{14}OOH \\
1\text{-}C_7H_{14}OOH &\rightleftharpoons 1\text{-}C_7H_{14}O + OH \\
O_2C_7H_{14}OOH &\rightleftharpoons OC_7H_{13}OOH + OH \\
OC_7H_{13}OOH &\rightleftharpoons C_4H_9CHO + CH_2CHO + OH \quad .
\end{aligned}$$

The addition of second O_2 leads to extensive chain branching. All the low-temperature processes described above are dependent on the size and structure of fuel molecule. Rates of the H atom abstraction vary with type of C-H bonds and number of atoms in the transition state [74]. Westbrook et al. [75] also give the sources for the reaction rate parameters for the reactions.

4.2.2.1 Suitable Mechanism for Use in ILDM Routines

The low-temperature processes of the mechanism are too slow (large time scales) to be used in ILDM treatment, because they would require much higher dimension of the ILDM manifold for their time-resolution. This would destroy the purpose of

automatic reduction. Additionally, they occur only during the auto-ignition period. Therefore they are treated separately in the ignition model, described in Section 5.8. Major portion of the combustion in Diesel engines occurs at high temperatures. Only the reactions described in the high-temperature oxidation section above are necessary for a full description of the combustion process. These reactions contain the $H_2/O_2/CO$ subsystem, the C_1/C_2 subsystem, the C_3/C_4 subsystem and system to link these subsystem to n-heptane. This link is based on the idea that alkyl radical decomposition by alkene elimination and subsequent alkene oxidation are not rate limiting processes in lower alkane oxidation. Therefore the complex alkyl radical decomposition path can be replaced by a simple reaction path leading to only one representative small alkyl radical and one representative small alkene, both of which should be present in the $C_1/C_2/C_3$-hydrocarbon subsystem [76].

CH_3 is chosen as the representative alkyl radical and largest alkene for which a reasonable detail chemistry is known is chosen as representative alkene, namely butene (C_4H_8). This forms the basis of the 393 reaction, 43 species reaction used in the ILDM treatment. The $H_2/O_2/CO$ subsystem, the C_1/C_2 subsystem, the C_3/C_4 subsystem contained in this mechanism have all the details necessary to get the sources for key intermediates (O, OH, C_2H_2, C_3H_3) including those required for predicting pollutants.

4.3 Pollutant Formation

Combustion in Diesel engine can lead to pollution in several ways. While sound pollution is a topic out of the scope of present work, toxic chemical releases as byproducts of combustion reactions are considered here. These include formation of nitrogen oxides and formation of soot. Both are a cause of major respiratory and health problems. The formation of sulfur oxides is not addressed in this work.

4.3.1 NO_x Formation

NO_x emission consists of mostly nitric oxide (NO), and to a lesser degree nitrogen dioxide (NO_2) and nitrous oxide (N_2O). NO_x is a precursor for photochemical smog, contributes to acid rain, and causes ozone depletion and hence is considered a pollutant. In turbulent combustion, the formation of NO_x can be attributed to four distinct chemical kinetic processes: thermal NO_x formation, prompt NO_x formation, fuel NO_x formation, and intermediate N_2O.

Thermal NO_x is formed by the oxidation of atmospheric nitrogen present in the combustion by radicals such as O, OH and O_2 to NO_x at very high temperatures.

Zeldovich [78] proposed following three principal reactions:

$$\begin{aligned}
\mathrm{O} + \mathrm{N_2} &\xrightarrow{k1} \mathrm{NO} + \mathrm{O} \quad k_1 = 1.8 \times 10^{14} \exp\left(\frac{-318\,\mathrm{kJ}\cdot\mathrm{mol}^{-1}}{RT}\right) \frac{\mathrm{cm}^3}{\mathrm{mol}\cdot\mathrm{s}} \\
\mathrm{N} + \mathrm{O_2} &\xrightarrow{k2} \mathrm{NO} + \mathrm{O} \quad k_2 = 9.0 \times 10^{9} \exp\left(\frac{-327\,\mathrm{kJ}\cdot\mathrm{mol}^{-1}}{RT}\right) \frac{\mathrm{cm}^3}{\mathrm{mol}\cdot\mathrm{s}} \\
\mathrm{N} + \mathrm{OH} &\xrightarrow{k3} \mathrm{NO} + \mathrm{H} \quad k_3 = 2.8 \times 10^{13} \frac{\mathrm{cm}^3}{\mathrm{mol}\cdot\mathrm{s}} \quad .
\end{aligned}$$

Zeldovich also suggested that the thermal NO_x reactions can be de-coupled from the fuel oxidation chemistry since overall rate of NO formation via above mechanism is comparatively slower than the rate of fuel oxidation. The name "thermal" is used to indicate that the reaction occurs only at high temperature because of the high activation energy due to the strong triple bond in the N_2 molecule. This reaction is the rate limiting reaction in the formation of thermal NO. The rate of formation of NO is given by

$$\frac{\mathrm{d}\,[NO]}{\mathrm{d}t} = k_1\,[O]\,[N_2] + k_2\,[N]\,[O_2] + k_3\,[N]\,[OH] \quad . \tag{4.14}$$

Nitrogen atoms are assumed to be in a quasi-steady state, since the first reaction is the rate determining step.

$$\frac{\mathrm{d}\,[N]}{\mathrm{d}t} = k_1\,[O]\,[N_2] + k_2\,[N]\,[O_2] + k_3\,[N]\,[OH] \approx 0 \tag{4.15}$$

$$\text{hence} \quad \frac{\mathrm{d}\,[NO]}{\mathrm{d}t} = 2k_1\,[O]\,[N_2] \quad . \tag{4.16}$$

The instantaneous chemical source term in the NO transport equation can be calculated using the above equation 4.16.

Prompt NO_x is produced by high-speed reactions at the flame front. Previous studies have concluded that a reaction sequence initiated by the rapid hydrocarbon radical s + N_2 reactions produces NO_x in the hydrocarbon combustion. This rapid NO_x in formed via mechanisms other than thermal NO_x is termed as prompt NO_x by Fenimore [79]. Prompt NO_x emissions range from a few ppmv to more than 100 ppmv and predominant in the fuel rich regions of the flame zone. They are favored at lower temperatures ($< 1000K$). Following are some of the reactions in the Prompt NO_x formation mechanism:

$$\begin{aligned}
\mathrm{CH} + \mathrm{N_2} &\rightleftharpoons \mathrm{HCN} + \mathrm{N} \quad , \\
\mathrm{CH_2} + \mathrm{N_2} &\rightleftharpoons \mathrm{HCN} + \mathrm{NH} \quad , \\
\mathrm{CH_2} + \mathrm{N_2} &\rightleftharpoons \mathrm{H_2CN} + \mathrm{N} \quad , \\
\mathrm{C} + \mathrm{N_2} &\rightleftharpoons \mathrm{CN} + \mathrm{N} \quad ,
\end{aligned} \tag{4.17}$$

where, overall

$$\mathrm{CH} + \mathrm{N_2} \xrightarrow{k_4} \approx 2\mathrm{NO} \quad k_4 = 1.8 \times 10^{14} \exp\left(\frac{-318\,\mathrm{kJ}\cdot\mathrm{mol}^{-1}}{RT}\right) \frac{\mathrm{cm}^3}{\mathrm{mol}\cdot\mathrm{s}} \quad . \tag{4.18}$$

Analysis shows that the individual contribution of the overall production and destruction of NO is that NO + CH_i reactions are relatively fast. They overwhelm the production of prompt NO. The consumption and production reactions occur in same spatial locations [80]. This explains why NO profiles exhibit peak values at the temperature maxima (verified in the simulation results in Section 7.8 and Fig. 7.11). Reaction of NO with CH_i produces HCN which can lead back to the formation of NO via same pathway as in prompt NO. Whether NO is actually removed or simply recycled depends on the fate of N atoms [81].

Fuel NO_x is produced by oxidation of nitrogen contained in the fuel. Studies have shown that most of the nitrogen present in fossil fuel is in the form of heterocycles like pyridine, quinoline and amines [82]. The extent of conversion to NO_x is dependent on the local characteristics and initial concentration of N-bound compounds. From thermal decomposition of these compounds, intermediates such as CH_3CN, CH_2CHCN and HCN can be formed which give rise to radicals such as CN, NH and N. These radical as then converted to NO_x. It is not a significant source of NO_x for most fuels other than coal due to low fuel-N content. At elevated pressures and oxygen-rich conditions, NO_x may also be formed from molecular nitrogen (N_2) via N_2O. This route is however not a significant source of NO [70]

From the considerations given above, it is clear that thermal NO_x is the significant path of NO_x formation in Diesel engines. It, along with prompt NO_x are calculated in this study. Inclusion of prompt NO_x in equation 4.16 gives

$$\frac{\mathrm{d}\,[NO]}{\mathrm{d}t} = 2k_1\,[O]\,[N_2] + k_4\,[CH]\,[N_2] \qquad . \tag{4.19}$$

The time scales involved in the NO formation reactions (see Fig. 5.2) are much slower than other chemical reactions. To decouple these time scales, the number of reaction progress variables needed would be very high to have enough time-resolution to get a solution using multi-dimensional PDF. Hence the NO_x chemistry is removed from the the mechanism used in ILDM calculation. Only the critically important intermediate species responsible for NO_x formation (viz. O, OH etc) are obtained from ILDM. The NO rates are then calculated in the main solver using the intermediate species concentrations received from ILDM.

The relationships among NO_x formation rate, temperature, and species concentration are highly nonlinear. Hence, if time-averaged composition and temperature are employed in any model to predict the mean NO_x formation rate, significant errors will result. Temperature and composition fluctuations must be taken into account by considering the probability density functions which describe the time variation. The rate constants k_1 and k_4 are functions of the species concentrations as well as ξ, T and b, c. Consequently, the mean source term is calculated by integrating the instantaneous source term by integrating over the joint PDF, such that

$$\widetilde{\frac{\mathrm{d}\,[NO]}{\mathrm{d}t}} = \int \frac{\mathrm{d}\,[NO]}{\mathrm{d}t} P(\tilde{\xi})\; P(\tilde{T})\; P(\tilde{b})\mathrm{d}\xi\;\mathrm{d}T\;\mathrm{d}b \qquad . \tag{4.20}$$

Zeldovich mechanism accounts for more than 75% of NO produced in turbulent natural gas flames. But it overpredicts N_2 consumption rates at low strain rates because it does not account for reburn. assuming this to be true in general for straight chain hydrocarbon fuels, in this work, the reburn is addressed in the following section. At high strain rates, Zeldovich mechanism overpredicts N_2 consumption because it does not account for prompt mechanism (discussed above).

Turbulence generates fluctuations of temperature and species concentrations and causes straining of flame structure. The intrinsic correlation of oxygen concentrations and temperature in the reaction zone is a key reason affecting the accuracy of NO prediction. A model proposed by Bowman et. al. for natural gas flames for such a correlation (assuming it to be valid in general for straight chain hydrocarbon fuels) is used in this work when the cells are treat using 1-step chemistry (as described in Section 5.5.3. This model has been validated using the results of DNS by Bowman et. al [83]. The correlation is applied as a correction to the O atom concentration in the PDF treatment, and is given by

$$\begin{aligned} C_{\mathrm{O}} &= 1.0 - 0.9\,\xi \quad \text{for lean mixtures} \ , \\ C_{\mathrm{O}} &= 0.05\,\xi \quad \text{for rich mixtures} \ , \end{aligned}$$

where C_{O} is the correlation coefficient.

4.3.2 NO_x Destruction

NO is consumed predominantly by three radicals viz. CH, CH_2 and CH_3. Reaction of NO with OH leads to formation of NO2 which is recycled back to NO. Moreover, for methane-air flames, it has been reported that the overall rate of reaction of NO with OH radicals is far lower than that with CH_i radicals [80]. Therefore the reactions of NO with CH_i radicals is included in the overall NO production rate calculation:

$$\begin{aligned}
\mathrm{CH} + \mathrm{NO} &\rightleftharpoons \mathrm{HCN} + \mathrm{O}: \quad k_{5\mathrm{a}} = 5.0 \cdot 10^{13} \\
&\rightleftharpoons \mathrm{NCO} + \mathrm{H}: \quad k_{5\mathrm{b}} = 2.9 \cdot 10^{13} \\
&\rightleftharpoons \mathrm{HCO} + \mathrm{N}: \quad k_{5\mathrm{c}} = 2.9 \cdot 10^{13} \\
\mathrm{CH_2} + \mathrm{NO} &\rightleftharpoons \mathrm{HCN} + \mathrm{OH}: \quad k_{6\mathrm{a}} = 2.9 \cdot 10^{14} T^{-0.69} \exp\left(\frac{-760}{RT}\right) \\
&\rightleftharpoons \mathrm{HNCO} + \mathrm{H}: \quad k_{6\mathrm{b}} = 3.1 \cdot 10^{17} T^{-1.38} \exp\left(\frac{-1270}{RT}\right) \\
&\rightleftharpoons \mathrm{HCNO} + \mathrm{H}: \quad k_{6\mathrm{c}} = 3.8 \cdot 10^{13} T^{-0.36} \exp\left(\frac{-580}{RT}\right) \\
\mathrm{CH_3} + \mathrm{NO} &\rightleftharpoons \mathrm{H_2O} + \mathrm{HCN}: \quad k_{7\mathrm{a}} = 9.6 \cdot 10^{13} \exp\left(\frac{-28800}{RT}\right) \\
&\rightleftharpoons \mathrm{H_2CN} + \mathrm{OH}: \quad k_{7\mathrm{b}} = 1.0 \cdot 10^{12} \exp\left(\frac{-21750}{RT}\right) \\
&\text{all activation energies in } \frac{\mathrm{cal}}{\mathrm{mol}} \text{ and rates in } \frac{\mathrm{cm}^3}{\mathrm{mol} \cdot \mathrm{s}} \quad .
\end{aligned}$$

overall:

$$\begin{aligned} \mathrm{CH} + \mathrm{NO} &\xrightarrow{k_5} \approx P: \quad k_5 = k_{5\mathrm{a}} + k_{5\mathrm{b}} + k_{5\mathrm{c}} \\ \mathrm{CH_2} + \mathrm{NO} &\xrightarrow{k_6} \approx P: \quad k_6 = k_{6\mathrm{a}} + k_{6\mathrm{b}} + k_{6\mathrm{c}} \\ \mathrm{CH_3} + \mathrm{NO} &\xrightarrow{k_7} \approx P: \quad k_7 = k_{7\mathrm{a}} + k_{7\mathrm{b}} \quad . \end{aligned}$$

4.3.3 Soot Formation

Incomplete combustion of fuel leading to formation of agglomerates of solid carbon particles is referred to as soot. It remains a challenging proposition to predict soot with accuracy due to the complex process [84] of condensation gaseous molecules and their further growth into solid particles. Models which are computationally expensive, but detail in description do exist [85, 86, 87]. Empirical correlations relating the engine operating parameters to exhaust gas soot concentrations [88] have limited validity. A semi-empirical model describing the formation of soot in few global steps, which capture critical species concentration from ILDM sets an ideal stage for prediction of soot concentration. The global steps of soot formation can be explained as give below;

1. C_3H_3 and C_2H_2 formation during scission for fuel molecule.
2. Recombination of C_3H_3 and C_2H_2 to an aliphatic C_6H_6 under fuel-rich conditions.
3. Polycyclic Aromatic Hydrocarbons (PAH), the precursors to the soot particles are formed from rearrangement of C_6H_6.
4. Enlargement of particles due to coagulation and surface growth. Surface growth is due to attachment of gas phase species to the surface of existing particles. Coagulation occurs when two particles combined to form a larger particle.
5. Oxidation of some of the soot particles predominantly by OH , but also by O and O_2

Only a small number of variables are used to characterize the process of soot formation. Soot volume fraction f_V, the soot number density N_S corresponding to the number of soot particles per unit volume are such two variables. For spherical articles , they can be related to each other through

$$f_\mathrm{v} = \frac{\pi}{6} N_\mathrm{s} d_\mathrm{s}^3 \quad . \tag{4.21}$$

The soot concentration C_S in terms of moles per unit volume therefore can be given using Avogadro's number N_A as

$$C_\mathrm{S} = \frac{N_\mathrm{S}}{N_\mathrm{A}} \quad . \tag{4.22}$$

The source of C_S is the soot particle generation while that of f_V is the growth phase of soot particles [24]. The simplified chemistry models are now described, which

are finally used to derive the balance equations for the two variables mentioned above. These simplification are based on combination of different processes in soot formation [89, 90, 91, 92, 93, 94]. The rate coefficients in the model are obtained empirically from experimental data for heptane oxidation in shock tube [95, 96].

Soot Concentration The primary positive source in the calculation of soot concentration is due to nucleation, a process believed to to initiated by the following reaction

$$C_3H_3 + C_3H_3 \rightleftharpoons C_6H_6 \rightarrow C_6H_6(\text{Benzene}) \quad . \tag{4.23}$$

An assumption is made that at least 10 Benzene molecules are required to form a single soot particle. Surface growth or oxidation processes does not alter the soot concentration. The primary negative source in the soot concentration expression is because of coagulation, described by a collision number β [97]. The overall rate of change of soot concentration is given as

$$\left(\frac{\mathrm{d}C_S}{\mathrm{d}t}\right) = \left(\frac{\mathrm{d}C_S}{\mathrm{d}t}\right)_N + \left(\frac{\mathrm{d}C_S}{\mathrm{d}t}\right)_C \quad , \tag{4.24}$$

$$\left(\frac{\mathrm{d}C_S}{\mathrm{d}t}\right)_N = \frac{\alpha}{10} \quad , \tag{4.25}$$

$$\left(\frac{\mathrm{d}C_S}{\mathrm{d}t}\right)_C = -\beta \cdot C_S^2 \tag{4.26}$$

$$\text{where} \qquad \alpha = 2.0 \times 10^6 \frac{\mathrm{m}^3}{\mathrm{mol}\cdot\mathrm{s}} \left(\frac{[C_3H_3]}{\mathrm{mol/m}^3}\right)^2 \quad , \tag{4.27}$$

$$\text{and} \qquad \beta = 1.0 \times 10^7 \frac{\mathrm{m}^3}{\mathrm{mol}\cdot\mathrm{s}} \left(\frac{T}{K}\right)^{1/2} \quad . \tag{4.28}$$

Soot Volume Fraction Soot volume fraction has source terms due to all three processes viz. nucleation, surface growth and oxidation. Coagulation does not affect the soot volume fraction. The nucleation source term is given as

$$\left(\frac{\mathrm{d}f_v}{\mathrm{d}t}\right)_N = \delta = V_N \cdot \alpha \quad [1/s] \quad , \tag{4.29}$$

$$\text{where} \quad V_N = m_{soot}/\rho_{soot} \quad , \tag{4.30}$$

and m_{soot} is the molecular weight of soot (approximated to that of $C_{60}H_{60}$ and ρ_{soot} is the density of soot (approximately 1.8 gm/cm3). Surface growth, resulting from attachment of C_2H_2, is a first order gas phase reaction [97] and is given as [95];

$$\left(\frac{\mathrm{d}f_v}{\mathrm{d}t}\right)_{SG} = \gamma \cdot f_v^{2/3} \cdot C_S^{1/3} \cdot N_A^{1/3} \cdot \frac{f_{v,\infty} - f_v}{f_{v,\infty}} \quad , \tag{4.31}$$

$$\text{with} \quad \gamma = \frac{\sigma_{SG}}{\rho_{soot}} \sqrt{\frac{N_A R_O m_G}{2\pi}} (36\pi)^{1/3} T^{1/2} C_G \quad , \tag{4.32}$$

where m_G and C_G are the mass and the concentration of species responsible for growth, i.e. C_2H_2. Finally, after substituting the constants, we have

$$\gamma = \sigma_{SG} \cdot 4.97 \times 10^{-4} \cdot \left(\frac{T}{K}\right)^{1/2} \cdot \left(\frac{[C_2H_2]}{\mathrm{mol/m}^3}\right) \left[\frac{\mathrm{m}}{\mathrm{s}}\right] \quad , \tag{4.33}$$

where σ_{SG} ($= 1.4 \times 10^{-3}$) is the sticking coefficient for C_2H_2. A curve fit gives the maximum volume fraction [95] as a function of the excess C atom concentration, termed as $C_{surplus}$, such that

$$f_{v,\infty} = 1.453 \times 10^{-6}\, C_{surplus}^{1.7} \quad . \tag{4.34}$$

The excess C atom concentration is obtained by computing the C atoms present above that of a critical C/O ratio. The ratio is dependent on fuel type and pressure, and a value of 0.5 is used in this work [98]. Reduction in the concentration due to oxidation is because of the reaction of soot with OH atoms. A single step reaction described the process as

$$\text{Soot} - \text{C} + \text{OH} \longrightarrow \text{Soot} + \text{CHO} \quad , \tag{4.35}$$

$$\text{where} \quad \left[\frac{\mathrm{d}f_v}{\mathrm{d}t}\right]_{ox} = \epsilon \cdot f_v^{2/3} \cdot C_S^{1/3} \cdot N_A^{1/3} \quad , \tag{4.36}$$

$$\epsilon = \sigma_{ox} \cdot 3.4 \times 10^{-4} \cdot \left(\frac{T}{K}\right)^{1/2} \cdot \left(\frac{[OH]}{\mathrm{mol/m^3}}\right) \left[\frac{\mathrm{m}}{\mathrm{s}}\right] \; . \tag{4.37}$$

Here, $\sigma_{ox}(= 0.1)$ [70] is the sticking coefficient of OH on the surface of soot particles. The change in soot volume fraction is given as

$$\frac{\mathrm{d}f_v}{\mathrm{d}t} = \delta + \gamma \cdot f_v^{2/3} \cdot C_S^{1/3} \cdot N_A^{1/3} \cdot \frac{f_{v\infty} - f_v}{f_v} - \epsilon\, f_v^{2/3} \cdot C_s^{1/3} \cdot N_A^{1/3} \quad . \tag{4.38}$$

The averaged source terms for the volume fraction and concentration are calculated by integrating the instantaneous values of the various coefficients ($\alpha, \beta, \epsilon, \delta \text{and} \gamma$) over the PDF described in 5.18 and 5.31. They can be described as

$$\begin{aligned} \widetilde{\dot{C}_S} &= \frac{1}{10} \int \alpha \cdot \tilde{P}\left(\xi, T, Y_{CO_2}\right) \mathrm{d}\xi\, \mathrm{d}T\, \mathrm{d}\left(Y_{CO_2}\right) \\ &- C_S^2 \int \beta \cdot \tilde{P}\left(\xi, T, Y_{CO_2}\right) \mathrm{d}\xi\, \mathrm{d}T\, \mathrm{d}\left(Y_{CO_2}\right) \quad , \end{aligned} \tag{4.39}$$

$$\begin{aligned} \widetilde{\dot{f}_v} &= \int \delta \cdot \tilde{P}\left(\xi, T, Y_{CO_2}\right) \mathrm{d}\xi\, \mathrm{d}T\, \mathrm{d}\left(Y_{CO_2}\right) \\ &+ \cdot f_v^{2/3} \cdot C_S^{1/3} \cdot N_A^{1/3} \cdot \frac{f_{v,\infty} - f_v}{f_v} \int \gamma \cdot \tilde{P}\left(\xi, T, Y_{CO_2}\right) \mathrm{d}\xi\; \mathrm{d}\left(Y_{CO_2}\right) \\ &- f_v^{2/3} \cdot C_S^{1/3} \cdot N_A^{1/3} \int \epsilon \cdot \tilde{P}\left(\xi, T, Y_{CO_2}\right) \mathrm{d}\xi\, \mathrm{d}T\, \mathrm{d}\left(Y_{CO_2}\right) \quad . \end{aligned} \tag{4.40}$$

The evaluation of the PDF is as described in the section 5.4.

The cells in which the Damköhler number exceeds the value of 1 amount to have reached equilibrium. However, such equilibrium is true for the major species. The pollutant species move slowly along the manifold. The precursors for the pollutants can still be obtained from ILDM and used to calculate the final pollutant concentrations. In the case of NO calculation, the concentration is calculated by integrating it over a temperature PDF.

Chapter 5

Turbulence - Chemistry Interactions

The approach toward modeling chemistry in flow systems has evolved significantly over the last several decades. The choice of an approach is decided by several factors. Computing time and storage of data puts severe restriction on the complex approaches using detailed reaction mechanisms. Such large mechanisms can be used in one- or two-dimensional systems and laminar flows [99, 74] with good success. The difficulty in use of such mechanisms is due to the range of time scales involved in the flow and chemistry phenomenon. It adds to the complexity of modeling three-dimensional flow with turbulence, such as that in a Diesel engine. While the flow equations are partial differential in nature, the chemistry equations are non-linear ordinary differential equations. Solution of a system which has these two forms of equations coupled with each other is extremely computing intensive and numerically unstable [100]. It is common to use simplified reaction schemes in Diesel engines [33] which have less than 10 species. However, simplified models can cost in terms of accuracy as well as their ability to predict trace species such as pollutants. Additionally, turbulent nature of flow requires that the interactions of chemistry with turbulence needs to be given a careful mathematical treatment.

5.1 Turbulence-Chemistry Interactions

Effects of turbulence on reaction zone structure in non-premixed as well as partially premixed flames have significant repercussions on combustion models. A complete understanding of the reaction zone dynamics is essential to elucidate the response of mass fractions of species, especially intermediates and minor but critical species, to turbulent fluctuations [101]. In several turbulent reactive flow studies, levels of intermediate species higher than predicted in steady laminar flames have been reported. CO levels measures in undiluted methane flames are significantly higher than those calculated for laminar flames [102]. Measurements of CO in bluff body flames have also shown higher levels than laminar flame calculations and PDF model predictions [103, 104]. OH concentrations are reported to be progressively increasing with increasing Reynolds number in methane/air jet flames [105], while elevated levels of OH and H_2 are reported in dilute methane flames [106]. Computational studies of Mauß et. al. [107] suggest that the higher concentration of CO are due to ignition-extinction processes. Unsteadiness and differential diffusion is also con-

sidered as a factor influencing the intermediate species [105]. All in all, turbulence and chemical reactions, when occurring together, require special attention.

Modeling approaches to turbulent reactive flows [108, 4] can be generally categorized according to two attributes; a) representation of flow & turbulence b) modeling of turbulence-chemistry interactions. The most common approaches to modeling flow and turbulence are [12]: Reynolds-averaged Navier-Stokes (RANS) turbulence modeling; large-eddy simulation (LES); and direct numerical simulation (DNS). At present, RANS is the dominant approach used in applications, whereas LES and LES-RANS hybrid is the focus of much research [109, 110]. While DNS is a powerful research tool [12], its range of applicability is severely limited (by computer power), much more so for reactive flows than for inert flows. It is interesting to note that the turbulence-chemistry interactions require modeling both in RANS and in LES [111]. The large-scale turbulent motions play dominant role in the transport of momentum, heat and species. These are well-represented in LES by the resolved fields. But in combustion, the essential processes of molecular mixing and reaction occur on the smallest (sub-grid) scales, and therefore require statistical modeling in RANS.

The fluctuations in species concentrations due to turbulence can be treated in two different ways to obtain the mean rates of reactions. In the first way, one can use the averaged concentration of species to calculate the mean reaction rate. In the second way, the instantaneous values can be used.

5.1.1 Mean Reaction Rates Using Average Concentrations

Consider a bimolecular reaction of the form (A + B $\longrightarrow$ Products) where A and B are two different species. When the flow conditions are such that the average concentration of A and B at a given location in space remains constant, then the rate of forward reaction can be given as

$$\dot{\omega}_{\mathrm{A}} = \dot{\omega}_{\mathrm{B}} = -k_{\mathrm{c}} Y_{\mathrm{A}} Y_{\mathrm{B}} \quad . \tag{5.1}$$

In a turbulent flow, where the concentrations are fluctuating, the mean reaction rate is given as

$$\overline{\dot{\omega}_{\mathrm{A}}} = -k_{\mathrm{c}} \overline{Y_{\mathrm{A}} Y_{\mathrm{B}}} = -k_{\mathrm{c}} \overline{Y}_{\mathrm{A}} \overline{Y}_{\mathrm{B}} - k_{\mathrm{c}} \overline{Y'_{\mathrm{A}} Y'_{\mathrm{B}}} \quad . \tag{5.2}$$

Three different scenarios are possible with respect to the phase of oscillations of the species concentrations. They can be oscillating in a) in phase b) overlapping or c) out of phase. These cases are shown in Fig. 5.1. When the species are in phase, then $\overline{Y'_{\mathrm{A}} Y'_{\mathrm{B}}} > 0$ and $\overline{Y_{\mathrm{A}} Y_{\mathrm{B}}} > \overline{Y}_{\mathrm{A}} \overline{Y}_{\mathrm{B}}$. When they are overlapping then $\overline{Y'_{\mathrm{A}} Y'_{\mathrm{B}}} < 0$ and $\overline{Y_{\mathrm{A}} Y_{\mathrm{B}}} < \overline{Y}_{\mathrm{A}} \overline{Y}_{\mathrm{B}}$. In the limiting case when the concentration of the two reacting species completely out of phase, we have a situation where $\overline{Y_{\mathrm{A}}} \neq 0$ and $\overline{Y_{\mathrm{B}}} \neq 0$ but $\overline{Y_{\mathrm{A}} Y_{\mathrm{B}}} = 0$. Thus the mean rate of reaction is zero in spite of the species concentrations being finite because the species are not present at the same location in space at the same time.

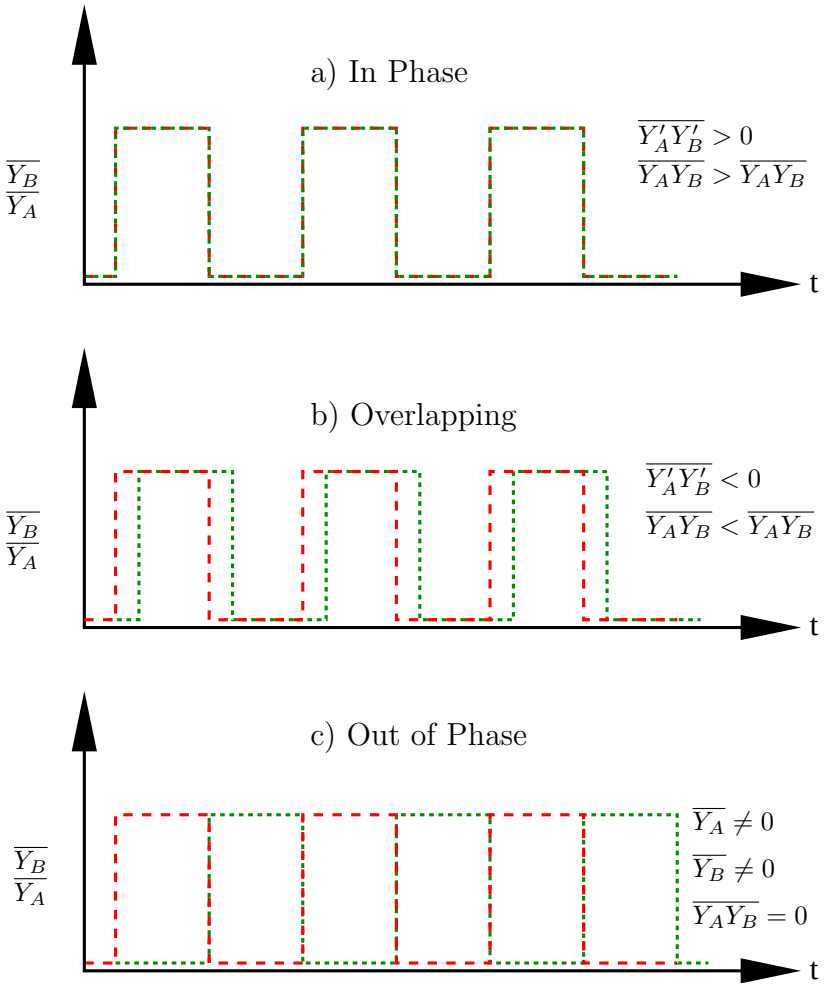

Figure 5.1: Hypothetical time behavior of species shows that reaction rates can be very high when the reacting species are in phase and negligible when out of phase.

If the oscillations in the temperature are also to be accounted for, then the rate coefficient cannot be evaluated at the average temperature as $k_c\left(\overline{T}\right)$. Instead, the rate coefficient at instantaneous values of temperature will have to be calculated and then averaged to give $\overline{k_c\left(T\right)}$. It has been shown [112] that the later has much higher values than the former for periodically oscillating systems.

5.1.2 Mean Reaction Rates Using Instantaneous Concentrations

Above discussion clearly indicates that there can be severe errors in estimating the mean reaction rates if they are calculated from the mean species concentrations. Instead, the instantaneous species concentrations needs to be used. Local mean reaction rates estimated from flame surface density, a measure of instantaneous flamelet reaction zone crossings of the turbulent flame brush, show good agreement with experimentally measurable variables [113]. It has been categorically stated that pollutants, such as NO, formation rates cannot be predicted from mean temperature and species concentration alone [83]. In a randomly oscillating field of species concentrations, statistical description can help to achieve this end. A joint probability

density function of the temperature and the scalar concentrations can capture the nuances due to the fluctuations. This function, when integrated over will give the required mean reaction rates. Evaluation of the moments (e.g., mean, variance or higher order moments) are required to completely characterize the PDF. There are two different ways this can be accomplished. Any one of the chemistry modeling methods discussed in Section 4.1 can be used with these two approaches, which are discussed in more detail below;

Joint PDF: The approach using multidimensional joint PDF involves solving the velocity-composition joint PDF or at least the composition joint PDF approach (when turbulence is modeled) [114, 115, 12]. A Monte-Carlo algorithm can be used to solve the transport equations. In this approach, the PDF is represented by ensembles of particles. Each particle contains information on the state variables affecting the chemical rate (e.g. mixture fraction, temperature, ...). To create the ensembles, a biased random number generator is used, which satisfies the physical constraints of the corresponding state variable. For example, it has to been ensured that mixture fractions are in the range $0 < \xi < 1$ and add up to unity. A random number generator creates ensembles of particles with given mean, variance and covariance of the state variables. To determine the mean reaction rate, the particle reaction rate has to be averaged over the ensemble. The rates obtained are stored in a look-up table for use in a subsequent CFD calculation as function of means and (co-)variances. In the CFD simulation, not only the flow field has to be solved but also transport equations for the mean and (co-)variance values of the parameters affecting the reaction rate. The corresponding chemical rates can easily obtained form a look-up table, which makes this approach fairly successful [116]. However, the molecular mixing terms remains unclosed and requires modeling. Therefore, its argued that the the closure problem associated with mean reaction rates is re-expressed in terms of molecular mixing term in the PDF closures [117]. This method requires substantial computer resources, and the effort is incommensurate with the information received about the flow [118].

Presumed PDF: Alternately, it is possible to assume the shape of the PDF as an analytical function. The parameters of the PDF are determined from the moments calculated from the transport equations [118]. The commonly used assumed shapes are the Gaussian functions [119], beta functions [120] or Dirac's delta function [121]. For the case of an adiabatic flame, an equilibrium chemistry model can be combined with the presumed PDF approach, giving the mean reaction rates as

$$\tilde{\dot{\omega}} = \int \dot{\omega}\left(\xi, T\right) \tilde{P}\left(\xi, T\right) \mathrm{d}\xi \, \mathrm{d}T \quad . \tag{5.3}$$

The transport equation for the variance of the mixture fraction is given by

$$\frac{\partial \overline{\rho}\widetilde{\xi''^2}}{\partial t} + \nabla\left(\overline{\rho}\tilde{\vec{\boldsymbol{u}}}\widetilde{\xi''^2}\right) = \nabla\left(\overline{\rho}D_{\mathrm{T}}\nabla\cdot\widetilde{\xi''^2}\right) + 2\overline{\rho}D_{\mathrm{T}}\left(\nabla\cdot\tilde{\xi}\right)^2 - 2\overline{\rho}\frac{\tilde{\epsilon}}{\tilde{k}}\widetilde{\xi''}^2 + 2\overline{\rho}\widetilde{\xi''^2}\frac{\dot{\tilde{\xi}}_{\mathrm{S}}}{\tilde{\xi}} \quad . \tag{5.4}$$

5.2 Reduced Reaction Mechanisms

If however, a detail reaction mechanisms composed of hundreds of reactions is to be used, the PDF will need to be expanded to take into account all the chemical species involved. The chemical source terms contain a wide range of time scales arising from various chemical reactions. In practice, this means the differential equations for the species are to be solved using implicit techniques. This leads to a large set of linearized algebraic equations solved using CPU-intensive Jacobian matrix computation task. The effort for Jacobian matrix computation is proportional to the square of the species involved. Handling the amount of data generated by such a PDF, the stiffness involved due to a wide range of times scales and the computational time required for solution, makes it of little practical use for 3-D industrial scale simulations of combustion. Therefore, much attention is being paid to the mechanism reduction techniques.

The easiest way to reduce a reaction system is to eliminate the less important species and the less influential reaction paths. The elimination procedure can be carried out, however only to a certain limit, to restrict the deterioration of performance (accuracy of predictions) with further reduction. A large reaction mechanism can also be split into two groups. One part of the mechanism can be solved with the flow equations while the second part is subjected to a variety of mathematical treatments. Splitting of the mechanism and decoupling of one part is the basis of all reduction techniques. Decoupling a part of mechanism rather than certain number of species has more advantage with respect to the computational effort.

Since the original set of mechanism is stiff, removing/reducing the stiffness becomes the core issue. Stiffness of a chemical reaction mechanism finds its roots in the width of the range of time scales of the system, often several orders in magnitude. The progress of a combustion process is however governed by the indispensable slow reactions. The range of time scales for a combustion system is illustrated in Fig. 5.2. The chemical source terms contains some fast time scale processes, but the entire reaction rate in practice is much slower. This implies that the reactions with much slower time scales shift to partial equilibrium soon after initiation and remain there during the subsequent process of combustion. This implies that the movements in the reaction space in certain directions are more or less frozen. As soon as the fastest groups approach to a steady-state situation, the combustion process is taking place through a manifold of the slower process, thus lower in dimension than the total number of species. This manifold, being a sub-space of the reaction space, can be described by a reduced number of *progress variables*.

The key problem now is to identify slow and fast processes.

5.2.1 Partial-Equilibrium Assumptions

A straight forward approach is to select reactions to eliminate. This accomplished by identifying fast processes with large reaction rates of elementary reactions [122]. This means that the net reaction rates of the fastest reactions are set to zero (al-

though the forward and backward reaction rates are not zero) leading to an algebraic equation. A major drawback of this method is that the reactions with fast rates change with time and space. Radicals are formed during initial phase while consumed in later phase of the process. Reactions producing and consuming the radicals are different. Therefore, knowledge of the chemical kinetics of all reactions is necessary for this method of elimination.

5.2.2 Steady-State Assumptions

Instead of identifying the fast time scales by reaction number, they are identified using species. A steady-state assumption for species which are produced and consumed fast, i.e., with negligible net source term, is made [123, 124]. For example, many radicals are produced very fast by one reaction and destroyed by another equally rapidly. If the source terms of these radicals are set to zero, the source term vector is frozen in those directions.

5.2.3 Decoupling of a Group of Species

In this approach, one group of species is solved with the flow equations, while the other group is solved in a post-processing mode. The mass fractions of the first group of species are important in the solution of flow, while that of the second group are negligible. However, the second group of species, with complex mechanisms, are solved in post-processing mode because of their importance as a design criteria, for example that of NO_x. CSP is one such strategy, that has been developed over the past couple of decades [125]. CSP is a procedure for analysis and reduction of chemical systems. It is used for automatic identification of fast and slow reaction processes and the elimination of fast/dormant modes. The method relies on the identification of a suitable set of basis vectors that enable the decoupling of fast and slow processes. A leading-order approximation of these vectors is provided by the eigenvectors of the Jacobian of the chemical source term. CSP provides a refinement procedure that iteratively adjusts the basis vectors to further improve the decoupling of the fast and slow sub-spaces [126].

5.3 Automatically Reduced Reaction Mechanisms - ILDM Chemistry

A dynamical approach, in contrast to the conventional approaches described above, tries to find out the directions in which the source term vector will rapidly reach a steady-state, is the ILDM approach [127,128,129]. The directions are not associated with any particular reaction or species and are not fixed throughout the combustion process. ILDM is a vector defined as the zeroth level-set (the set where the function takes on a given constant value) of a multidimensional function. As shown in Fig. 5.2, the chemical processes faster than the turbulent mixing time scales are assumed to be in dynamic equilibrium with the mixing processes and the slower chemical processes. This allows the fast processes to be expressed as combinations of slow processes, entailing considerable reduction in number of variables required

to describe chemistry [130]. Consider a detailed chemical mechanism with n_s species

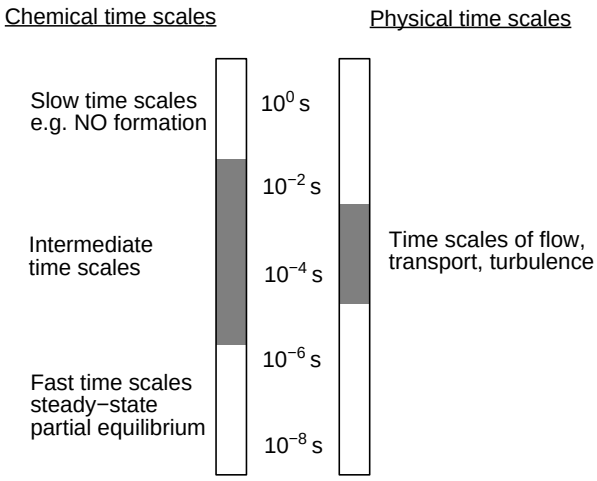

Figure 5.2: Time scales in a typical combustion processes [70].

representing a composition space. Then n_s different time scales govern the entire process. If n_f processes are assumed to be in equilibrium, the system can be described by $n_r = n_s - n_f$ degrees of freedom. If all the time scales are assumed to be relax, an equilibrium chemistry model emerges, corresponding to a zero-dimensional manifold. This manifold can be characterized by only two variables viz. mixture fraction and temperature. For a system where all except n_r timescales are relaxed, the characteristic parameters are mixture fraction, temperature, pressure and n_r number of other parameters called progress variables. Each progress variable stands for an additional dimension of the manifold on the composition space. Together they represent the low-dimensional manifold, a subspace of the composition space where only slow processes take place [131].

The manifolds have a property to attract reaction trajectories. Reaction paths in the detailed mechanism will proceed to the manifold rapidly, while the subsequent movement on the manifold will be slow. The progress variables parametrize this slow movement on the manifold. For discrete values of the progress variables, compositions are calculated and stored in a data base. An *in-situ* method of tabulation [132] using AVL trees facilitates creation of only the points required in the CFD simulation and a quick search methodology [133]. AVL tree is an self-balancing binary search tree, named after Adelson-Velsky & Landis [134], suited for data insertion, deletion and look-up intensive operations.

Fig. 5.3 shows the reaction trajectories for a stoichiometric CH_4-air system, projected on the H_2O-CO_2 plane. The equilibrium point is marked by a circle. Complete trajectories till equilibrium are shown in the third diagram. Each trajectory is for a distinct initial condition. The system takes approximately 5 ms to reach equilibrium, as shown in the second diagram. After a time of 50 μ s, a single line in the state space corresponding to one dimensional manifold is seen. All processes slower than 50 μs are described by the movement along this line. All processes faster than 50 μs are assumed to be in equilibrium. Higher dimensional manifolds are required

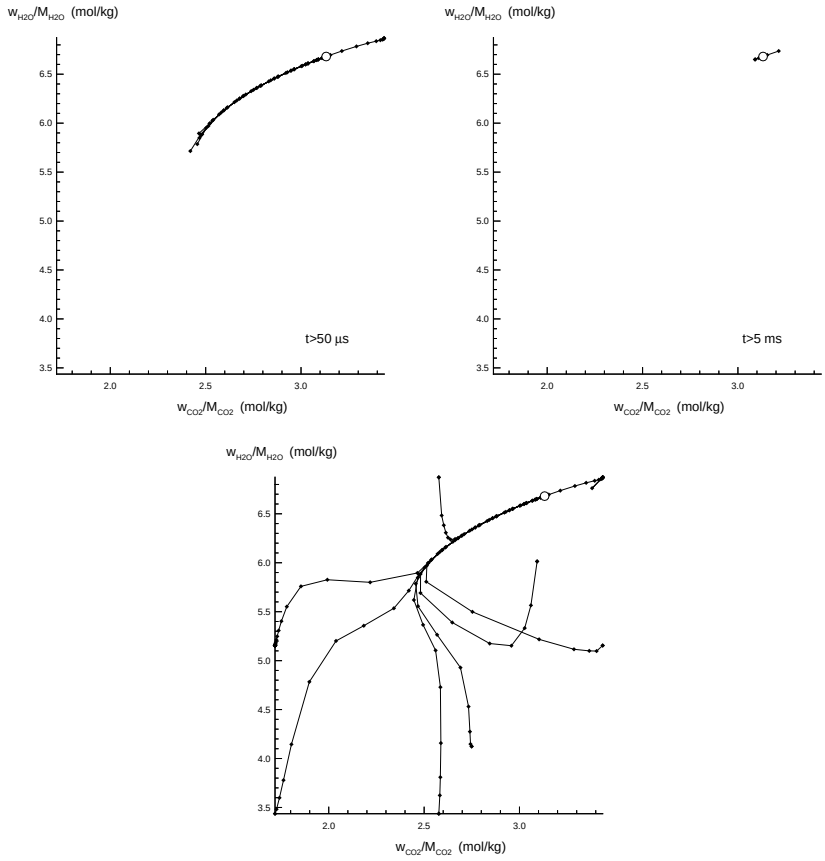

Figure 5.3: Reaction trajectories in a CH_4/air system [70]. Equilibrium point denoted by a circle.

to filter out processes which are faster than 50 μs. If however, all processes are to be slower than 5 ms, we would only see the trajectory as a point, corresponding to all processes being in equilibrium.

5.3.1 Mathematical Treatment of ILDM

The conservation equation of the species (Equation 2.5) can be rewritten (ignoring the spray source term) in terms of specific mole numbers $\phi_i = Y_i/M_i$ as

$$\begin{aligned} \rho\frac{\partial\phi_i}{\partial t} + \rho\nu\cdot\nabla\phi_i - \nabla\cdot(\rho D_i\nabla\phi_i) &= \rho w_i \quad , \\ w_i &= \frac{\dot{\rho}}{\rho M_i} \quad . \end{aligned} \tag{5.5}$$

For simplicity, in a homogeneous, isobaric and adiabatic system, the equation can be modified to

$$\frac{\mathrm{d}\phi_i}{\mathrm{d}t} = w_i \quad . \tag{5.6}$$

We can include the temperature and pressure also as variables to contain $n = n_{s+2}$ variables for n_s species plus pressure and temperature. This represents a n-dimensional state-space $\vec{\psi}$. A state of a system is represented by a point in the

state space. Linearizing the source term vector $\vec{\psi} = (T, p, w_1, w_2, ..., w_n)^{\mathrm{T}}$ around a reference composition ψ^0 leads to

$$\frac{\mathrm{d}\psi}{\mathrm{d}t} = \vec{\boldsymbol{F}}\left(\vec{\psi}\right) \quad , \tag{5.7}$$

$$\vec{\psi} \approx \vec{\psi}\left(\vec{\psi^0}\right) + \boldsymbol{J}\left(\vec{\psi} - \vec{\psi^0}\right) \quad , \tag{5.8}$$

$$\text{where} \qquad \boldsymbol{J} = \left(\frac{\partial\vec{\psi}}{\partial\vec{\psi}}\right)^0_\psi$$

denotes the Jacobian of the source term vector. Therefore the species balance equation 5.6 can be represented as

$$\frac{\mathrm{d}\vec{\psi}}{\mathrm{d}t} \approx \vec{\boldsymbol{F}}\left(\vec{\psi^0}\right) + \boldsymbol{J}\left(\vec{\psi} - \vec{\psi^0}\right) \quad . \tag{5.9}$$

To assess the local characteristics of the system, these equations are transformed into the basis of eigenvectors of the Jacobian matrix, given by;

Where the eigenvectors are defined by	$\boldsymbol{J}\boldsymbol{s_i} = \lambda_i \boldsymbol{s_i}$	(5.10)
Defining a transformation matrix $\boldsymbol{S}$ by	$\boldsymbol{S} = (\boldsymbol{s_1}, \boldsymbol{s_2}, ..., \boldsymbol{s_n})$	(5.11)
Assuming $\boldsymbol{J}$ is diagonizable, we have	$\boldsymbol{J}\boldsymbol{S} = \boldsymbol{S}\Lambda$	(5.12)
So that only diagonal elements are non-zero	$\Lambda = \mathrm{diag}\,(\lambda_1, ..., \lambda_n)$	(5.13)
Readjusting, one can easily get	$\Lambda = \boldsymbol{S}^{-1}\vec{\boldsymbol{J}}\boldsymbol{S}$	(5.14)

Eigenvectors and eigenvalues can be complex numbers. The state space vector can be re-written in terms an eigenvector basis [131]. Then each of the differential equation in the system is decoupled and solutions can be given by

$$\psi = \psi_0 + \frac{\vec{\boldsymbol{F}}\left(\psi^0\right)}{\lambda_i}\left[\exp\left(\lambda_i t\right) - 1\right] \quad . \tag{5.15}$$

If the magnitude of an eigenvalue is large, movements in the direction of corresponding eigenvectors will be fast. If the the eigenvalue is negative, the process will extinguish and arrive in a steady-state situation. And, if the eigenvalue is positive, the process will not relax to a steady-state. Thus, the reaction groups with large negative eigenvalues will rapidly approach a steady-state. At the equilibrium point, all eigenvalues are negative or zero [127]. A Schur decomposition of the Jacobian gives a matrix N such that the eigenvalues appear as the diagonal elements of N:

$$\boldsymbol{Q}^{\mathrm{T}}\boldsymbol{J}\boldsymbol{Q} = N \quad . \tag{5.16}$$

The low-dimensional manifold in the state space can be defined by the following condition

$$\boldsymbol{Q}_{\mathrm{L}}^{\mathrm{T}}\boldsymbol{J} = 0 \quad , \tag{5.17}$$

where $\boldsymbol{Q}_{\mathrm{L}}^{\mathrm{T}}$ is the matrix of left eigenvectors obtained by omitting the first $2 + n_{\mathrm{e}} + n_{\mathrm{r}}$ rows of $\boldsymbol{Q}^{\mathrm{T}}$ (n_{e} is the number of elements, n_{r} is the number of relaxed

processes). These rows correspond to the conserved scalar variables viz pressure, enthalpy/temperature, the element compositions plus the relaxed processes. If the conserved scalars are known, the above equation can be solved to obtain the rate of reaction of the progress variables. These rates can then be used in the transport equations of the progress variables, to compute a time step progress in the chemical system.

5.4 PDF Formulation with ILDM

Two progress variables, viz. CO_2 and H_2O are used for creating the ILDM table. Using two progress variables compared to a single progress variable allows a better resolution of time scales in cases when the gap between the physical and chemical time scales is narrow. The methodology for the use of 1 progress variable and 2 progress variables with corresponding PDF formulation is discussed in the following sections. The instantaneous rate of reaction of the progress variables $\left(\dot{Y}^{\mathrm{C}}_{\mathrm{CO_2}}\right)$ and $\left(Y^{\mathrm{C}}_{\mathrm{H_2O}}\right)$ is obtained from a query to the ILDM table. The Favre-averaged species equation however contains the mean chemical source terms. The source terms therefore need to be integrated over the probability density function.

5.4.1 One (1) Reaction Progress Variable

The average reaction rates are obtained by averaging the laminar rates from the ILDM tables using the probability density functions. For the case of a single progress variable where CO_2 is used as the progress variable, the mean rate is given by an integration over a three-dimensional PDF;

$$\widetilde{\dot{Y}^{\mathrm{C}}_{\mathrm{CO_2}}} = \int \dot{Y}^{\mathrm{C}}_{\mathrm{CO_2}}\left(\xi, T, Y_{\mathrm{CO_2}}\right) \tilde{P}\left(\xi, T, Y_{\mathrm{CO_2}}\right) \mathrm{d}\xi \, \mathrm{d}T \, \mathrm{d}\left(Y_{\mathrm{CO_2}}\right) \quad . \tag{5.18}$$

Now, the three dimensional PDF $\tilde{P}\left(\xi, T, Y_{\mathrm{CO_2}}\right)$ is to be specified. Construction of such a PDF requires the variances of all variables as well as the co-variances between them. although, there are methods to solve multidimensional PDFs, they are not very suitable for complex systems. Hence statistical independence between the variables is assumed. This assumption is not completely true since CO_2 depends on T and ξ. A special treatment needs to be given to CO_2 and is described below. The shapes of the one-dimensional PDFs can now be assumed and the mean moments can be used to construct the PDF. Choosing a shape which appropriately describes the variable over a range of operating conditions is important to get accurate results. Gaussian function [119], beta function [120] and Dirac's delta [121] function are the commonly used function shapes. The scalar PDF has been known to be of Gaussian shape in the final stages of mixing from experimental and DNS data [136]. During early stages of mixing, it resembles a double Dirac delta function. The shapes of PDFs reported in literature [135], for two-scalar mixing cases are shown in Fig. 5.4.

The β PDF has been shown to be extremely versatile depending on the value of the variance [136]. It can replicate the shapes found in DNS (see Fig. 5.4), and

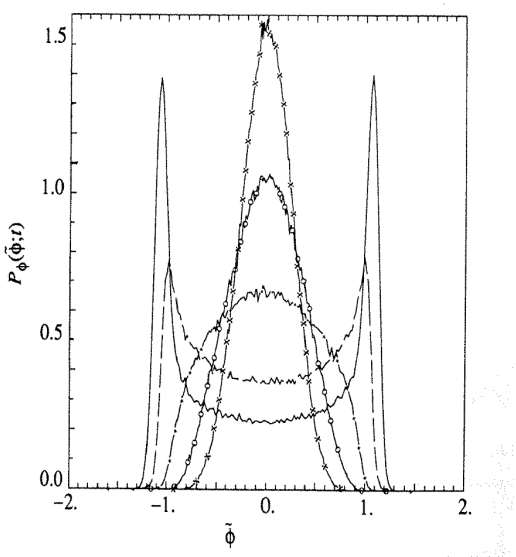

Figure 5.4: Evolution of scalar PDF due to mixing obtained from DNS data [135].

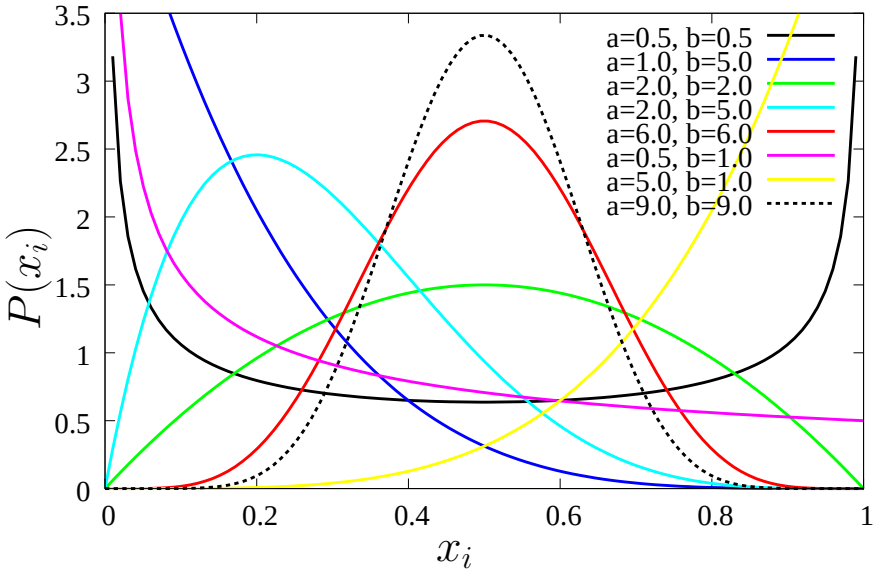

Figure 5.5: Shape of β PDF for various values of parameters a and b.

is shown as calculated from its Equation 5.20 in Fig. 5.5. In the initial stages of mixing, the β PDF resembles a dirac-delta function while in the later stages of mixing, it resembles a Gaussian function, and is in accordance with the experimental results [137]. A β PDF is very simple to construct due to being defined using only two parameters, say a and b, which can be determined from the mean and variance in a staightforward manner. The β function of a variable Z is given by

$$P(Z) = \gamma \cdot Z^{(a-1)} \cdot (1-z)^{(b-1)} \tag{5.19}$$

$$\text{where } \gamma = \frac{\Gamma(a+b)}{\Gamma(a)\,\Gamma(b)} \tag{5.20}$$

where $\boldsymbol{\Gamma}$ represents the Gamma function. The parameter γ is used as a normalization factor and is determined such than an essential property of the PDF is satisfied, i.e.,

$$\int_0^1 P(Z)\,\mathrm{d}Z = 1 \quad . \tag{5.21}$$

The parameters a and b are determined from the mean $\overline{Z}$ and variance $\overline{Z''^2}$ as [12];

$$b = \frac{\overline{Z}\left(1-\overline{Z}\right)^2}{\overline{Z''^2}} + \overline{Z} - 1 \quad , \tag{5.22}$$

$$a = \frac{b\overline{Z}}{1-\overline{Z}} \quad . \tag{5.23}$$

If the Favre mean $\tilde{Z}$ and variance $\widetilde{Z''^2}$ is used instead, the above definitions provide the Favre PDF $\tilde{P}(Z)$ [117].

Using the strategy outlined above, a PDF $\tilde{P}(\xi)$ of the mixture fraction ξ can be created using the mean $\tilde{\xi}$ and the variance $\tilde{\xi''^2}$. The mixture fraction is defined in the interval $[0;1]$. The value of 0 corresponds to pure air while that of 1 corresponds to pure fuel.

However for the case of temperature, the interval needs to be set as $[0;1]$ by normalizing with the range of temperature $T_{\max} - T_{\min}$. The mean of temperature is calculated from Equation 2.18. Unfortunately, the variance of temperature is not simple to calculate because one needs to first solve the variance transport equation of the energy. The variance transport equation of the energy has many unclosed terms due to chemistry. An easy formulation can be made based on the assumption that the intensity of the turbulence is same for the mixture fraction and the temperature [48], i.e.,

$$\frac{\widetilde{\xi''^2}}{\widetilde{\xi}} = \frac{\widetilde{T''^2}}{\widetilde{T}} \quad . \tag{5.24}$$

For the case of the reaction progress variable CO_2, a transport equation needs to be solved , given as

$$\frac{\partial \overline{\rho}\widetilde{Y_{\mathrm{CO_2}}}}{\partial t} + \nabla\cdot\left(\overline{\rho}\,\widetilde{\vec{u}}\,\widetilde{Y_{\mathrm{CO_2}}}\right) = \nabla\cdot\left(\overline{\rho}D_{\mathrm{T}}\,\widetilde{\vec{u}}\,\nabla\widetilde{Y_{\mathrm{CO_2}}}\right) + \overline{\rho}\,\widetilde{\dot{Y}^{\mathrm{C}}_{\mathrm{CO_2}}} \quad . \tag{5.25}$$

The mean CO_2 concentration is calculated from the above equation. The instantaneous source term due to chemistry $\widetilde{\dot{Y}^{\mathrm{C}}_{\mathrm{CO_2}}}$ is obtained from ILDM as described in Equation 5.18. If a β function for CO_2 is to be used, an equation for its variance is needed. such a variance equation would contain even more fluctuation terms requiring modeling. Instead, a δ function for CO_2 can be used. Before describing how the PDF of CO_2 is obtained, it has to be be noted that the CO_2 mass fraction is dependent on the mixture fraction and temperature. Hence, the assumption of statistical

independence described in Equation 5.27 can give erroneous results. The CO_2 concentration is zero for $\xi = 0$ and $\xi = 1$, while it is maximum for $\xi = \xi_{\text{stoichiometric}}$. All the possible CO_2 concentrations lie within these limits, as can be represented by the shaded area as shown in Fig. 5.6. If a δ function for CO_2 is used, then it will re-

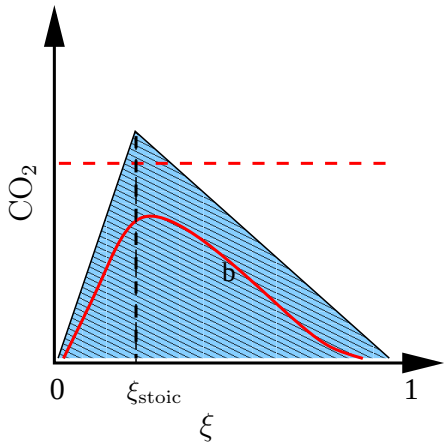

Figure 5.6: Schematic representation of normalization of CO_2. Dashed red line indicates integration boundary in absence of normalization, and has non-physical states. Area under the shaded triangle represents physical states. Dashed black line indicates location of stoichiometric composition.

quire an integration of the dotted red line (representing the distribution of CO_2 with varying mixture fraction, which is assumed to be independent of mixture fraction and temperature). This would mean integrating over unphysical points, outside the shaded area. This can be addressed by normalizing the CO_2 concentration by the maximum CO_2 concentration and defining a new variable b such that

$$b = \frac{Y_{\text{CO}_2}}{Y_{\text{CO}_2,\text{max}}} \quad . \tag{5.26}$$

The idea behind the normalization is that the maximum concentration of CO_2, occurring at equilibrium, is dependent on temperature and mixture fraction. Hence, the normalized variable b and the other two variables T and ξ can be approximated statistically independent of each other without introducing critical errors. The PDF $\tilde{P}(\xi, T, Y_{CO_2})$ can be transformed to $\tilde{P}(\xi, T, b)$. Also, it allows the splitting of a three-dimensional PDF into three one-dimensional PDFs and is given as;

$$\tilde{P}(\xi, T, b) = \tilde{P}(\xi)\ \tilde{P}(T)\ \tilde{P}(b) \quad . \tag{5.27}$$

The red curve in Fig. 5.6 shows how the distribution of CO_2 will look after normalization. It falls within the shaded area and can be integrated, as there are no unphysical points. The mean and variance of the variable b needs to be calculated ans is given as follows

$$\widetilde{b} = \left[\frac{\widetilde{Y_{\text{CO}_2}}}{Y_{\text{CO}_2,\text{max}}}\right] \approx \left[\frac{\widetilde{Y_{\text{CO}_2}}}{\widetilde{Y_{\text{CO}_2,\text{max}}}}\right] \tag{5.28}$$

. The mean CO_2 concentration $\widetilde{Y_{CO_2}}$ is obtained from the transport equation (5.25) ,

$$\widetilde{Y_{\mathrm{CO_2,max}}} = \int Y_{\mathrm{CO_2,eq}}\, \widetilde{P\left(\xi\right)}\widetilde{P\left(T\right)}\, \mathrm{d}\xi\, \mathrm{d}T \quad . \tag{5.29}$$

The local maximum $Y_{\mathrm{CO_2,eq}}$ concentration is only a function of the mixture fraction and the temperature. It is read from a table created using any standard equilibrium code [138] and integrated over ξ and T.

5.4.2 Two (2) Reaction Progress Variables

The procedure outlined above is extended to the case of two progress variable, where H_2O is additionally used as the second progress variable. The transport equation for H_2O is given as

$$\frac{\partial \overline{\rho}\widetilde{Y_{\mathrm{H_2O}}}}{\partial t} + \nabla \cdot \left(\overline{\rho}\, \widetilde{\vec{u}}\, \widetilde{Y_{\mathrm{H_2O}}}\right) = \nabla \cdot \left(\overline{\rho} D_{\mathrm{T}}\, \widetilde{\vec{u}}\, \nabla \widetilde{Y_{\mathrm{H_2O}}}\right) + \overline{\rho}\, \widetilde{\dot{Y}^{\mathrm{C}}_{\mathrm{H_2O}}} \quad , \tag{5.30}$$

while the PDF for H_2O is given as follows

$$\widetilde{\dot{Y}^{\mathrm{C}}_{\mathrm{H_2O}}} = \int \dot{Y}^{\mathrm{C}}_{\mathrm{H_2O}}\left(\xi, T, Y_{\mathrm{H_2O}}\right) \tilde{P}\left(\xi, T, Y_{\mathrm{H_2O}}\right) \mathrm{d}\xi\, \mathrm{d}T\, \mathrm{d}\left(Y_{\mathrm{H_2O}}\right) \quad . \tag{5.31}$$

Performing a normalization of the H_2O concentration to give a variable c,

$$c = \frac{Y_{\mathrm{H_2O}}}{Y_{\mathrm{H_2O,max}}} \quad , \tag{5.32}$$

The PDF $\tilde{P}\left(\xi, T, Y_{\mathrm{H_2O}}\right)$ can be transformed to $\tilde{P}\left(\xi, T, c\right)$. We can write the three-dimensional PDF as a product of three one-dimensional PDFs,

$$\tilde{P}\left(\xi, T, c\right) = \tilde{P}\left(\xi\right)\ \tilde{P}\left(T\right)\ \tilde{P}\left(c\right) \quad , \tag{5.33}$$

where the mean of c is given as

$$\widetilde{c} = \left[\frac{\widetilde{Y_{\mathrm{H_2O}}}}{Y_{\mathrm{H_2O,max}}}\right] \approx \left[\frac{\widetilde{Y_{\mathrm{H_2O}}}}{\widetilde{Y_{\mathrm{H_2O,max}}}}\right] \quad . \tag{5.34}$$

Consequently the mean H_2O concentrations can be calculated from the transport equation of H_2O while the mean maximum is calculated from

$$\widetilde{Y_{\mathrm{H_2O,max}}} = \int Y_{\mathrm{H_2O,_{eq}}}\, \widetilde{P\left(\xi\right)}\widetilde{P\left(T\right)}\, \mathrm{d}\xi\, \mathrm{d}T \quad . \tag{5.35}$$

The local maximum $Y_{\mathrm{H_2O,eq}}$ concentration is only a function of the mixture fraction and the temperature. It is read from a table created using any standard equilibrium code and integrated over ξ and T.

5.5 Application of ILDM

Physical processes, like diffusion or turbulent transport, try to pull the system off the manifold. However, fast chemical processes relax the system back to the manifold, if the time scale of the physical perturbation is longer than the time scale of the relaxing process. This perturbation can be decomposed into two components: one that rapidly relaxes back to the manifold, and one that leads to a net perturbation along the manifold. This behavior is taken into account by projecting the governing species conservation equations on to the manifold [128].

5.5.1 Challenges

The promising principles behind ILDM have been applied successfully to homogeneous reactors [128] and laminar premixed flames [140]. However, applicability of ILDM under any given range of operating conditions is still fraught with challenges, some them being listed below:

1. These systems are usually in the stoichiometric or near-stoichiometric region. Performance of ILDM in this region is very good, but in the rich and lean regions remains to be investigated.
2. ILDM does not perform well in the early stages of combustion (un-burnt gases) since resolving the time scales becomes extremely difficult due to slow ignition chemistry.
3. Higher hydrocarbon system introduce increased amount of stiffness, due low equilibrium radical concentrations, in the differential equations. Therefore, the behavior of ILDM may not be as it is seen for lower hydrocarbons.
4. Higher pressures in Diesel engines cause the time scales to be faster compared to atmospheric systems.

For the study conducted in this work, C_7H_{16} (n-heptane) is used as a fuel to model the Diesel fuel because it represents the ignition-delay timings very well (see Section 5.8). n-Heptane has a cetane number of 56, very close to that of Diesel (50). Miyamoto et. al. [141] have found that regardless of the specific molecular structure, nitric oxide emissions are linearly increased with C/H atomic ratio 0.53 for Diesel and 0.44 for n-heptane. This leads to a scaling factor of 1.2 for NO_x emissions. A detailed reaction mechanism consisting of 43 species and 393 elementary reactions [142] is used to produce ILDM tables with one and two reaction progress variables. The ILDM table is a 3-dimensional table for single progress variable case and a 4-dimensional table for the two- progress-variable case. All other species compositions, enthalpy, density and specific heat are functions of these defining dimensions.

The pressure can be used as an additional dimension, because pressure affects the reaction rates described by fall-off curves [70]. The rate coefficients are reported to rise with increasing pressure to a certain value after which they follow a plateau. There is considerable variation in the reaction rates between atmospheric pressure

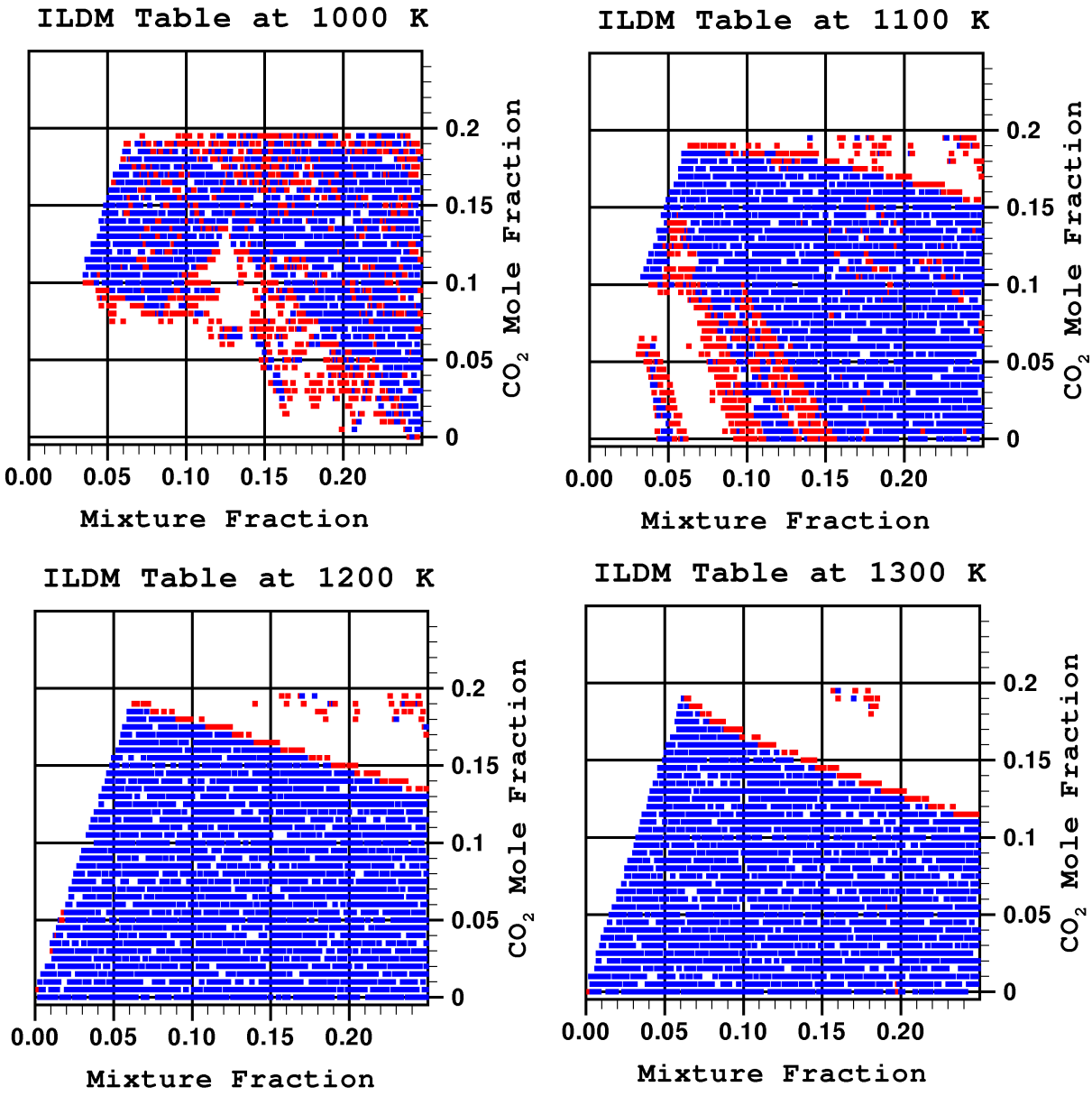

Figure 5.7: Slices of ILDM table with CO_2 as progress variable for heptane-air system at T=1000 K - 1300 K [139].

($\approx$ 1 bar) and 50 bar. But in the range of pressures in which the predominant portion of the reactions in Diesel engine take place, i.e. between 70 bar -100 bar, the rate coefficients almost remain constant. A representative pressure of 80 bar is used to reduce the dimension of ILDM without introducing any significant errors. Slices from the 3-D ILDM table at constant temperature are shown in Fig. 5.7- Fig. 5.10. The red squares denote points in state space where no ILDM points could be calculated, while the blue squares represent the successful calculation of an ILDM point. It can be seen (Fig. 5.7) that there are many failed points at low temperatures. As the temperature increases, ILDM is successful at more and more points.

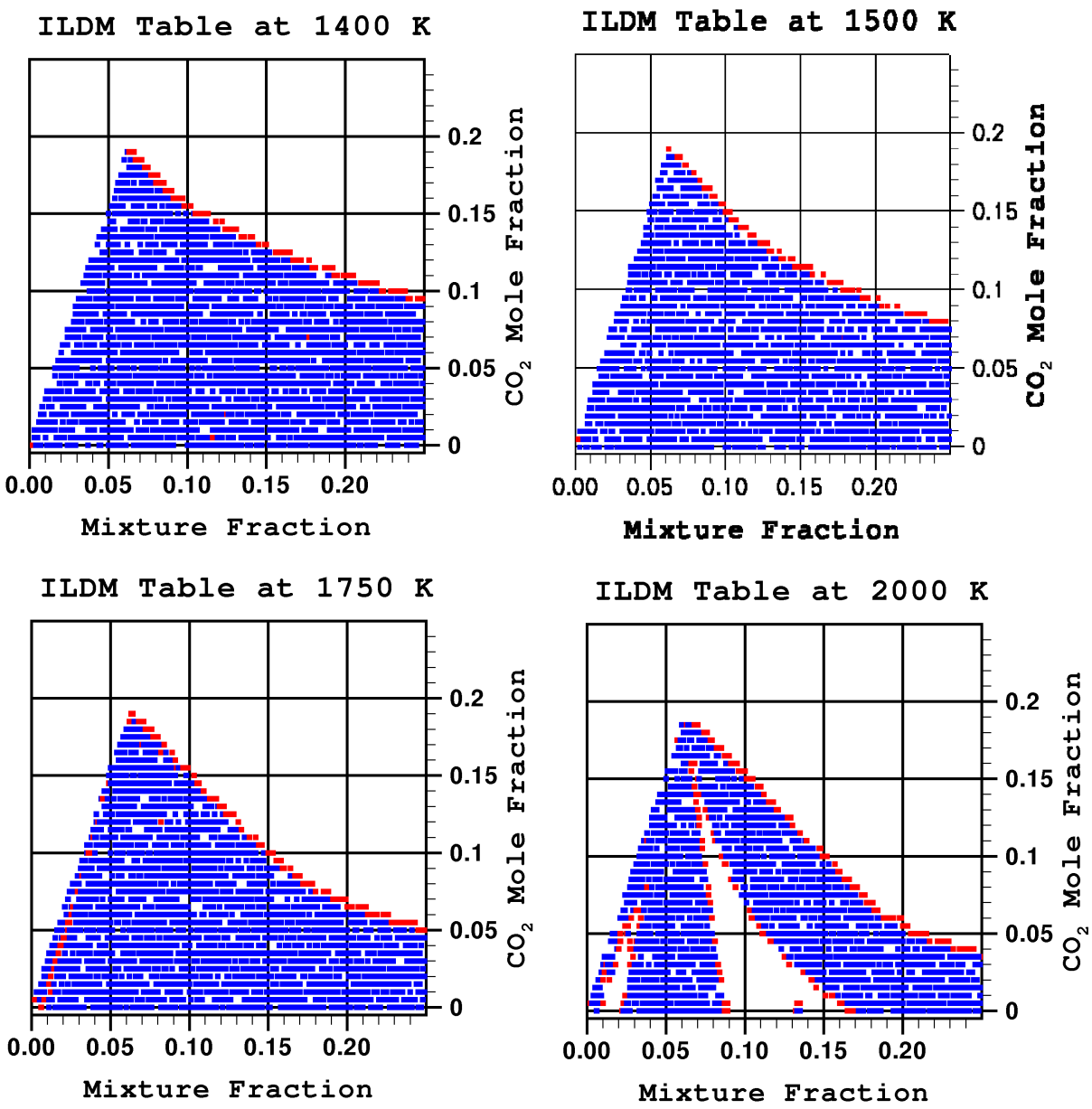

Figure 5.8: Slices of ILDM table with CO_2 as progress variable for heptane-air system at T=1400 K - 2000 K [139].

However, between 2000 K and 2500 K, a peculiar area (rich region with low CO_2 mole fractions) with failed ILDM points in the central region can be seen (Fig. 5.9). These could be because either no significant gap in the eigenvalue spectrum exists (mostly in the low temperature ignition regions) or due to numerical shortcomings in the resolution of time scales.

5.5.2 Strategy

A savvy strategy needs to be formulated in order to take advantage of the ILDM chemistry model where it gives good results and use other chemistry models (a one-step reaction) where ILDM cannot give good results. Ignitions in Diesel engines

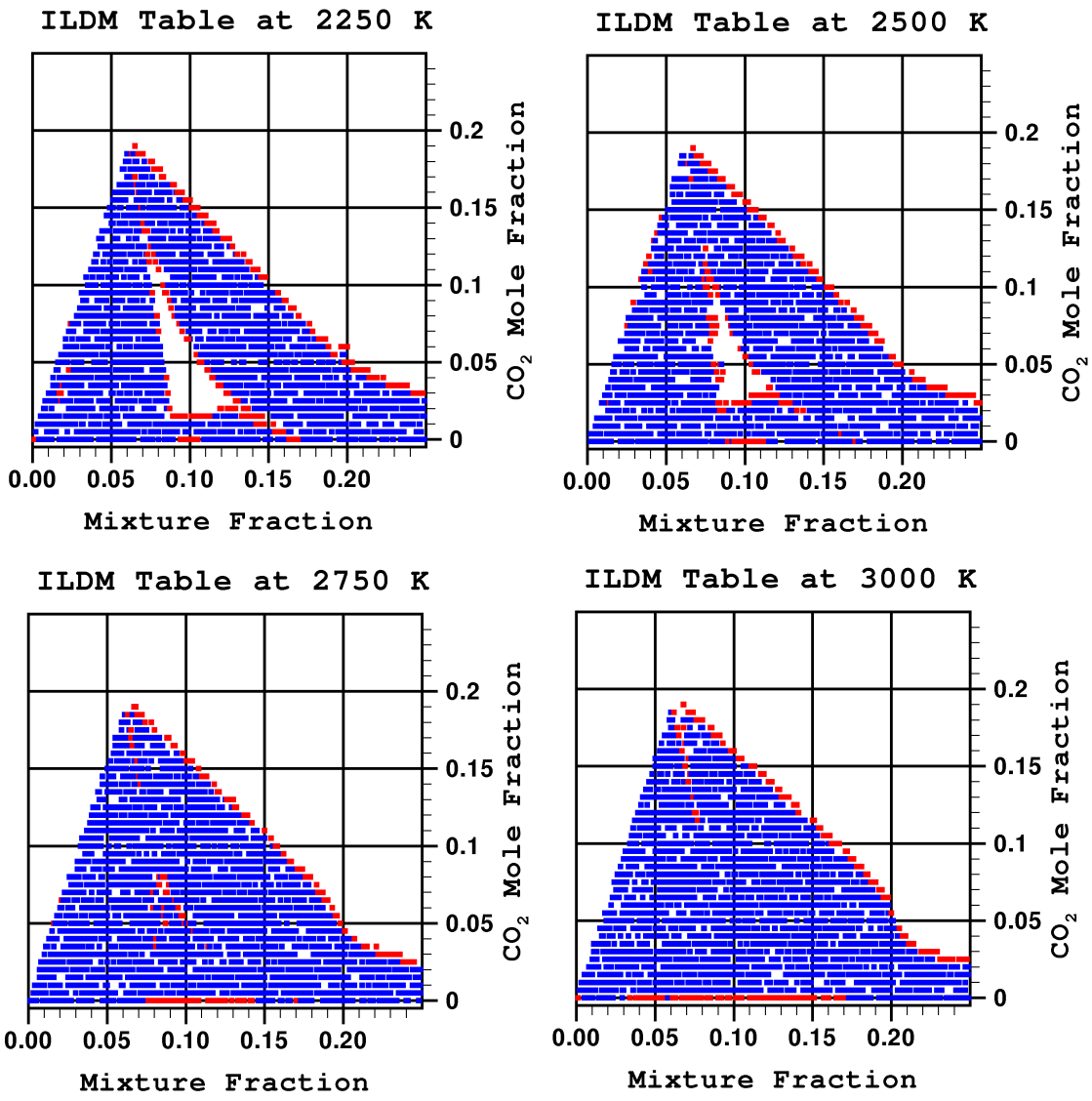

Figure 5.9: Slices of ILDM table with CO_2 as progress variable for heptane-air system at T=2250 K-3000 K [139].

takes place at pressures of 70 bar - 80 bar and temperatures of 900 K - 1000 K. ILDM chemistry models can be used above a temperatures of 1200 K in general and between 1000 K -1200 K only in certain range of progress variables and mixture fractions. The initial development of the flame needs to be addressed. The first cell in which ignition takes place can be placed on the manifold, with the assumption that it is immediately partially burned. To this effect, the temperature and species composition of this cell is set to lie on the manifold while the element composition is left unchanged. Alternately, a simple one-step global chemistry model also provides a convenient way. For the case of n-heptane, it is given as

$$C_7H_{16} + 11O_2 \longrightarrow 7CO_2 + 8H_2O \quad , \tag{5.36}$$

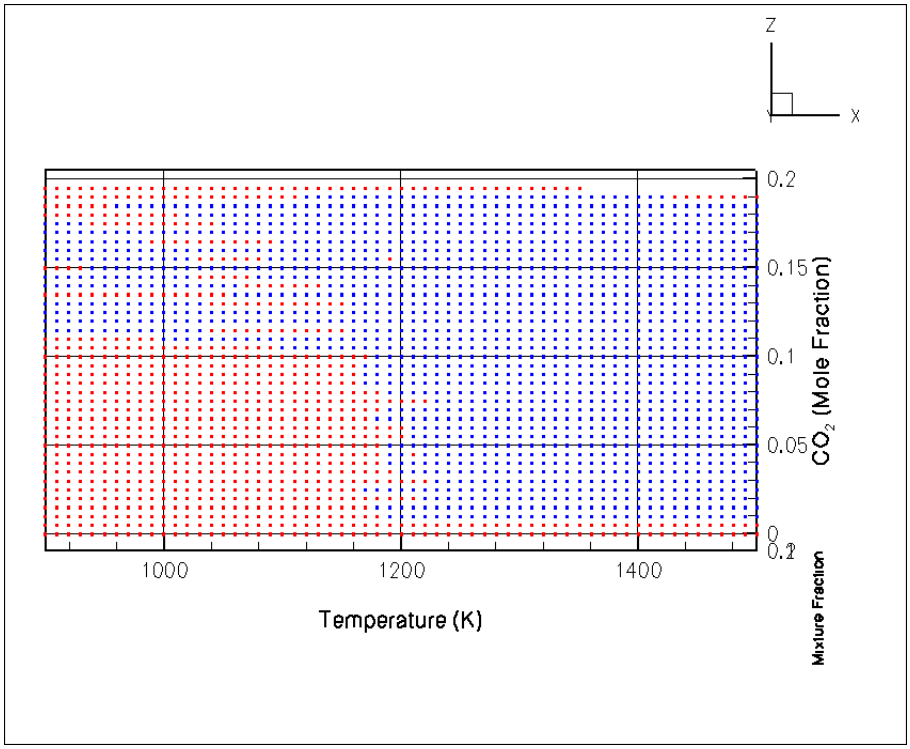

Figure 5.10: ILDM points table with CO_2 as progress variable for heptane-air system at T=900-1500 K [139]. Blue points are good points, red points are bad points.

where the kinetic rate coefficient for the reaction is given as

$$k = 4.6 \cdot 10^{11} \exp\left[\frac{-15780\text{K}}{T}\right] [C_7H_{16}]^{1/4} [O_2]^{3/2} \tag{5.37}$$

A suitable combination of the two is accomplished as follows: The first ignition cell is assumed to be partially burned and placed on the manifold. A representative temperature of 2200 K, CO_2 mass fraction of 0.1 and H_2O mass fraction of 0.8 is chosen to set this cell on the manifold. It is common to see secondary ignition spots in Diesel engines [24]. All the secondary ignition cells are subject to the global one-step chemistry model, if they are below 1200 K. If the cells are above a temperature of 1200 K, they are subject to the ILDM treatment. In practice, an overlap of 50 K in the cutoff limit of 1200 K is used to get a smoother transition, i.e., cells between 1150 K and 1200 K are treated with both global chemistry model as well as ILDM chemistry model.

It can be clearly seen from the Fig. 5.7 - Fig. 5.10 that there are regions within the state space where ILDM fails to deliver good results. These are indicated by the red points. In these region, the resolution of time scales is difficult due very narrow gaps. There are two ways this problem can be solved. Since these ILDM points are being used by the discrete points in a PDF, a global reaction cannot be used as a substitute. A model more consistent with the ILDM with PDF formulation needs to be devised. In these regions, the resolution of time scales is difficult due

very narrow gaps. That means the reaction is as slow as the physical processes, indicating that the reaction rate of the progress variables is zero, $\dot{Y}^{C}_{CO2} = 0$ and/or $\dot{Y}^{C}_{H2O} = 0$. Compositions of other species cannot be obtained when ILDM fails. However, compositions from neighboring good points can be used as a substitute, provided the following heuristically determined conditions are satisfied:

1. Since reaction rate of CO_2 is assumed zero, the CO_2 mass fraction of the chosen neighboring point should be approximately that of the failed point.
2. The mixture fraction ξ representing the element composition of the substitute or model point should also be equal to the failed point.
3. The dimension which can be varied to search the model point is temperature. Since ILDM succeeds in the higher temperature regimes, a higher temperature can be chosen for the model points.
4. The species compositions are heuristically adjusted in a fashion that the sum is equal to 1 and the elemental composition is kept constant.

Use of these model points can then make up for the failed areas of the ILDM table. Model points are calculated via an heuristic approach. It is however discovered that use of model points does not give good results and is unreliable. Very high temperatures are obtained during simulation as compared to the experiment. This probably occurs due to the fact that the model points are consistently placing the results at higher temperatures, resulting in overall higher temperatures. ILDM failure does not merely indicate that the chemical time scales are slow but may also mean that extinction of reaction is occurring. If a model point with higher temperature is substitute for such a cell with extinction, then this will alter the heat release of the system. Therefore, this method is abandoned.

In a new strategic formulation, the number of PDF points for a given cell are expanded from a previous limit of 20 to 40. The distribution of the points is fine-tuned in such way as to have more points around the stoichiometric regions (where ILDM is expected to succeed), for all three PDF's of mixture fraction, temperature and CO_2. Then at each point, the failure or success of ILDM is monitored. Only the successful points on the PDF are utilized whilst the failed points are expelled from the integration. If, however, the expelled points are greater than half the total number of points, then the ILDM treatment of the entire cell is abandoned. This cell is then subjected to a global one-step chemistry model.

5.5.3 Comparison of Physical and Chemical Time Scales

Mean scalar dissipation and mean rate of strain is calculated in each computational cell to evaluate the relative ratio of the flow time scale to that of the chemical time scale. The chemical time scale is obtained from the ILDM computation. It is important to note that the maximum reaction progress variable concentration ($CO_{2,eq}$ and H_2O_{eq} used in the normalization (and calculated from a typical equilibrium code) may be larger than the maximum possible for a given flow time. It implicitly meant an attainment of equilibrium regardless of local flow time scale, which is unrealis-

tic. This causes the normalized reaction progress variable concentration to be equal to (or greater than) 1. However, there may be flow regions where the flow time scale may be much less than the chemical time scale to reach equilibrium. If the Damköhler number, a ratio of flow time scale (eddy turnover time) to the chemistry time scale, is used to normalize the PDF integration, this formulation eliminates the unphysical states even if a non-equilibrium chemistry model is used. Effectively, the value of the $CO_{2,eq}$ and H_2O_{eq} used for normalization is scaled by the ratio of flow to chemistry time scales. When the ratio of flow time to chemical time is smaller than 1 for a given cell, the PDF integration calculation using chemistry source terms from ILDM is skipped and a simpler one-step reaction is used to calculate the chemistry and heat source terms. The results differ slightly when the inverse of the mean rate of strain is used to determine the flow time scale as against the scalar dissipation rate.

5.6 Scalar Dissipation

Strain Rate An easily calculable and measurable variable, viz., strain rate is used to define the structure and extinction characteristics of flames [143]. When the strain rate changes with time, any variation of the reactant stream is propagated instantly to the diffusion zone that surrounds the reaction zone. Therefore it is a good parameter to judge the variations in diffusive time scales. In the diffusive zones, mass fluxes are controlled by diffusion and conform to the velocity variations through a convective-diffusive balance, whereas in the reaction zone the chemistry responds to the variations in reactant supply imposed by the above mentioned convective-diffusive transport through a diffusive-reactive balance [144]. The magnitude of the rate of strain in a cell (i,j,k) is calculated from the stress tensor S_{lm}, which is given as

$$S_{lm} = \frac{1}{2}\left(\frac{\partial u_l}{\partial x_m}\frac{\partial u_m}{\partial x_l}\right)_{ijk} \quad , \tag{5.38}$$

where u_l represent the cell velocities in the respective directions.

Additionally, the scalar dissipation rate can also be used to characterize the diffusive-reactive balance in a flame. Accurate prediction of dissipative layer structures is possible, at least for the case of turbulent jets, if the unsteadiness in the strain field is taken into account [145]. Scalar dissipation structures thicken by the action of diffusion and thin out by the action of strain. However the time a structure takes to reach steady state depends only on the strain rate [146]. It has been observed, in both experiments as well as DNS, that largest scalar gradients tend to be aligned with the principal strain rate axis and hence dissipation layers are oriented orthogonal to this axis. At high frequency of oscillations, the scalar rate of dissipation is a better parameter to characterize the unsteady behavior of flames [147]. Local flame extinction can be explained by the scalar dissipation rate exceeding a critical value, thus making the residence (diffusion) time smaller than the chemical time of the local structure of the flame [148]. If scalar dissipation rates are much lower than the extinction limit, fluctuations of the dissipation rate caused by the turbulence do not influence the combustion process. But if the conditions are

close to auto-ignition or extinction, these fluctuations can have significant influence on the combustion process [149]. The scalar dissipation rate is defined and modeled using the following two equations

$$\chi = 2\,D\frac{\partial\xi}{\partial x_i}\frac{\partial\xi}{\partial x_i} \tag{5.39}$$

$$\widetilde{\chi} = 2\,\frac{\widetilde{\epsilon}}{\widetilde{k}}\widetilde{\xi^{"}} \quad , \tag{5.40}$$

where the last term in the second equation is the variance of mixture fraction.

Scalar Dissipation Rate Local instantaneous scalar dissipation rate, which describes the rate of molecular mixing of fuel and oxidizer, is considered as the most important parameter in non-premixed combustion [150]. It describes the departure from equilibrium. The structure of the reaction zone is strongly coupled to the underlying strain rate field through the influence of fluctuating strain on the scalar dissipation rate [151]. Scalar dissipation differs from energy dissipation because its less uniform in both space and time − a phenomenon called intermittancy [152]; described as intense localized fluctuations of any quantity in a turbulent flow. This can result in localized extinction and reignition of combustion processes.

5.7 Extinction

In the present work, the auto-ignition phenomenon is resolved using a separate ignition model described in the next section. However it is the extinction that is addressed as following. In a fashion similar to that described in Section 5.5.3, the comparison of the flow time scale to the chemistry time scale can be performed at every PDF point instead of just in a cell for the entire range of PDF points. Thus, either each cell as a whole (mean value) or each point on the T-ξ-rpv PDF is evaluated to check if $Da > 1.0$. If not, this point is skipped from the ILDM chemistry computation, amounting to an extinct location. Without the above formulation, the temperature keeps on increasing even in the later phase of combustion when the combustion in local structures is supposed to extinguish out. This is as shown by the light blue curve in Fig. 5.11. The cells where appropriate scaling cannot be found are treated using a one-step chemistry for heat release while the pollutant precursors are sought from ILDM with only the temperature PDF formulation. This combination gives a stable computing code and good results.

To perform the check on a cell as a whole is straight-forward. However, if the check is to be performed for each point of T-ξ-rpv PDF, then a corresponding PDF for scalar dissipation need to be formulated. The scalar dissipation in turbulent flames is known to have a log-normal distribution [137]. A beta PDF of the scalar dissipation [146] is used for this purpose. The mean of the scalar dissipation beta PDF being the value calculated for the cell and the maxima is the maximum scalar dissipation in the entire flow domain. The variance for the scalar dissipation is taken from the variance of the mixture fraction.

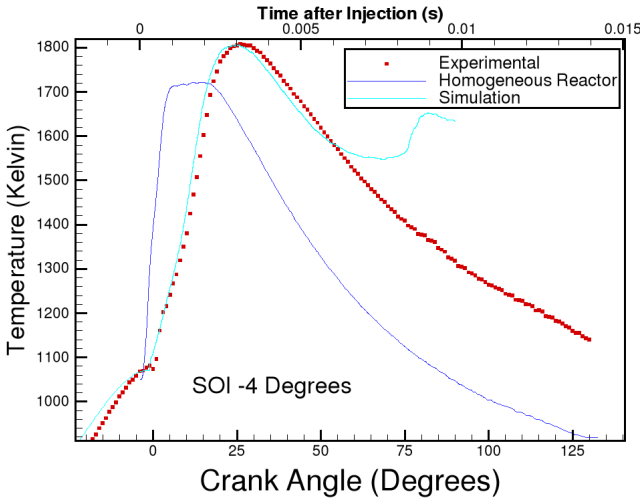

Figure 5.11: Temperature behavior in absence of time-scaling (light blue). Results for a homogeneous case (dark blue) given for comparison.

Alternately, a PDF of the scalar dissipation can be used in the integration of the mean chemical source term. It is hypothesized that such a formulation will not require a check as decribed in the paragraph above, but will increases the dimension of the PDF to 4 for single progress variable and 5 for two progress variable case. The methodology is based on statistical independence of PDF's, similar to that described in Sections 5.4.1 and 5.4.2 is used. Due to the higher dimension of the PDF, this path however is not adopted in the present work.

5.8 Ignition

Ignition is the beginning of the combustion process determining the flame development, power output and level of emissions [24]. It therefore requires a reliable model to predict ignition location and timing. The key parameter characterizing the ignition is the delay-time between the start of injection and beginning of combustion, indicating a period of relatively slow reaction. Auto-ignition occurs when the fuel-air mixture ignites without supply of external energy (like in the form of a spark). This occurs due to the amount of heat released by the reaction exceeding that lost to the surroundings, resulting in an explosion. DNS studies have reported that ignition spots occur where the scalar dissipation rate is low and mixture fraction is close to most reactive value viz. stoichiometric [153].

5.8.1 Ignition Chemistry

Diesel fuel is a mixture of several hydrocarbons viz. n-alkanes, branched and cyclic saturates as well as aromatics. The cetane number, indicating the ignition quality of a fuel, of n-heptane ($\approx$ 56) matches well with most Diesel fuels, making it a good choice as model fuel for Diesel engines. Auto-ignition in Diesel engine occurs between 750 K - 1100 K. It is characterized by development of a radical pool following initiation, propagation and chain-branching of several reactions. A detail mechanism containing 1200 elementary reactions and 200 species has been reported

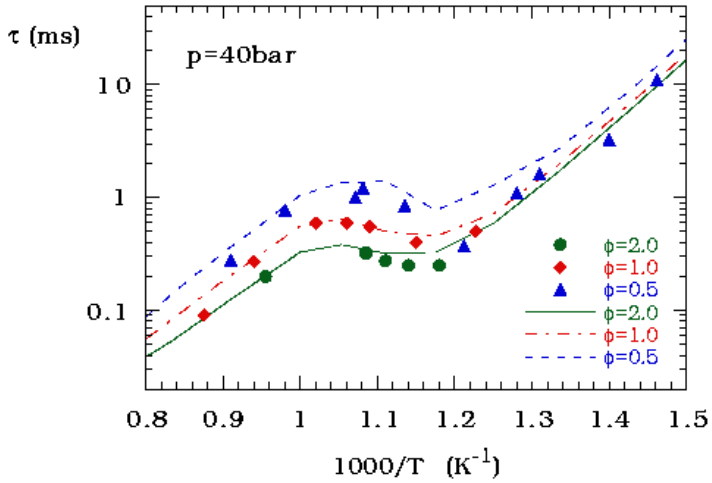

Figure 5.12: Ignition-delay calculations (lines) compared to experiments (symbols) for various equivalence ratios ϕ.

to accurately reproduce the ignition-delay times τ and laminar flame speeds of n-heptane [154] over a wide range of equivalence ratios (see Fig. 5.12). More details of the ignition chemistry and various reactions occurring during the low-temperature induction period is given in Section 4.2.2.

5.8.2 Ignition and Turbulence

Use of such mechanisms is unrealistic in a 3-dimensional engine code. The physical processes in auto-ignition are even more tedious to model, and only research oriented DNS studies exist [153]. An easier way to track the development of the radical pool is not to track all the species, but to pick a representative species. The representative species should monotonically increase until ignition and a rapid increase should be seen to signify ignition. CO is found to possess these characteristics [154]. A typical plot is shown in Fig. 5.13. For this species, a transport equation is required to be solved, and is given by

$$\frac{\partial \overline{\rho}\widetilde{Y_{\mathrm{CO}}}}{\partial t} + \nabla \cdot \left(\overline{\rho}\, \widetilde{\vec{u}}\, \widetilde{Y_{\mathrm{CO}}} \right) = \nabla \cdot \left(\overline{\rho} D_{\mathrm{T}}\, \widetilde{\vec{u}}\, \nabla \widetilde{Y_{\mathrm{CO}}} \right) + \overline{\rho}\, \widetilde{\dot{Y}^{\mathrm{C}}_{\mathrm{CO}}} + \overline{\rho}\, \widetilde{\dot{Y}^{\mathrm{S}}_{\mathrm{CO}}} \quad , \tag{5.41}$$

where $\widetilde{\dot{Y}^{\mathrm{C}}_{\mathrm{CO}}}$ and $\widetilde{\dot{Y}^{\mathrm{S}}_{\mathrm{CO}}}$ is the source term due to chemistry and spray, respectively. The chemistry source term is obtained from a pre-fabricated table of source terms calculated using a detail mechanism (with 200 species and 1200 reactions) in a homogeneous, isothermal, isobaric reactor. The CO reaction rates are tabulated as a function of CO concentrations for a variety of mixture fractions and pressures. They are interpolated as required in the main solver. A PDF integration procedure similar to that outlined in Section 5.4.1 is utilized. However, a beta PDF is used for CO and a transport equation for its variance is defined as [155]

$$\frac{\partial \overline{\rho}\widetilde{Y''^2_{\mathrm{CO}}}}{\partial t} + \nabla \cdot \left(\overline{\rho}\, \widetilde{\vec{u}}\, \widetilde{Y''^2_{\mathrm{CO}}} \right) = \nabla \cdot \left(\overline{\rho} D_{\mathrm{T}}\, \nabla \widetilde{Y''^2_{\mathrm{CO}}} \right) + 2\overline{\rho} D_{\mathrm{T}} \left(\nabla \cdot \widetilde{Y_{\mathrm{CO}}} \right)^2 - 2\overline{\rho} \frac{\widetilde{\epsilon}}{\widetilde{k}} \widetilde{Y''^2_{\mathrm{CO}}} \quad . \tag{5.42}$$

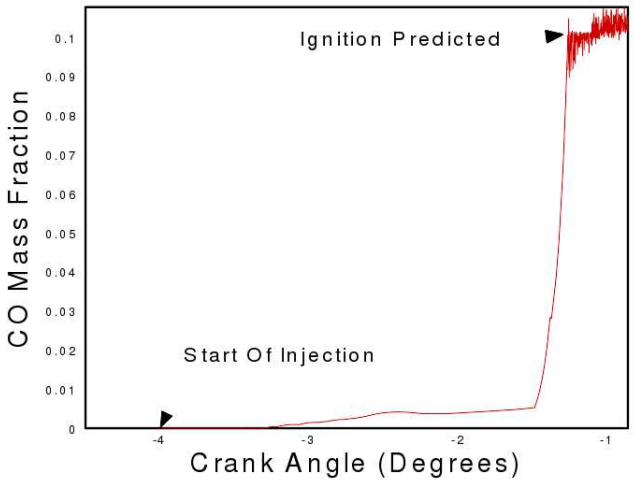

Figure 5.13: Rise in CO concentration leading to ignition using the representative species autoignition model, for the case of SOI -4° ATDC in a Caterpillar-3401 engine.

Here, the fluctuations in the source terms have been neglected. The mean source term due to spray is defined as a very small initial mass fraction of CO $=1.0^{-10}$. This is to provide a non-zero starting point so that the CO concentration can build up to ignition and does not affect the prediction of ignition. The criteria used to decide whether a cell is ignited or not is set as a mass fraction of 0.1, which is based on results from homogeneous reactor calculations.

It has been reported in literature [156] that during autoignition of n-heptane in counterflow diffusion flames, high-temperature chemistry is dominant for highly strained flames. When the strain rates are low, the low-temperature chemistry is the dominant pathway for ignition. The high-temperature chemistry is responsible for formation of OH radicals. A plot of strain rate and a corresponding values of OH radicals can then show the process responsible for autoignition in Diesel engine.

Chapter 6

Numerical Solution Techniques

The discretization of the governing equations of the combustion in KIVA involves a combination of the ALE (Arbitrary Lagrangian Eulerian) method for spatial discretization and a variably implicit time discretization method (variable theta methods)

6.1 Spatial Discretization with ALE method

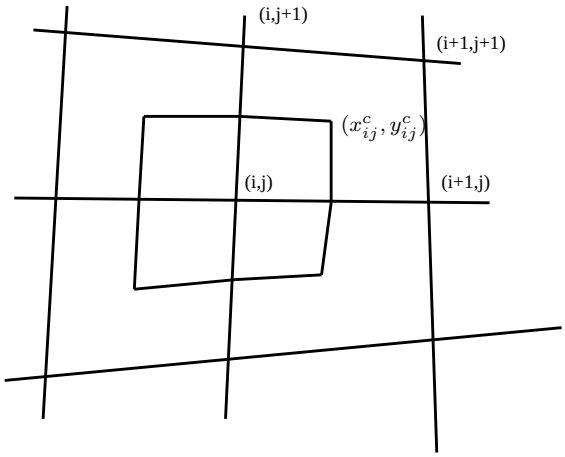

Figure 6.1: Two-dimensional ALE mesh.

ALE method is a finite volume method, for arbitrary hexahedrons in 3-D and four sided polygons in 2-D. The equations of motion are formulated with a moving velocity $\boldsymbol{U}$ of the grid, varying between 0 and u. Thus the formulation varies between continuously between Eulerian ($\boldsymbol{U} = 0$) and Lagrangian ($\boldsymbol{U} = u$). The normal equations 2.30, 2.31 and 2.32 are reformulated in an integral form with the introduction of parameter $\boldsymbol{U}$. In two-dimensions, the mesh for the ALE algorithm is defined as a polygon (See Figure 6.1) with 4 vertices, and the cell center is computed

as

$$x_{ij}^c = \frac{1}{4}\sum_{\alpha}^{4} x_\alpha \quad ,$$
$$y_{ij}^c = \frac{1}{4}\sum_{\alpha}^{4} y_\alpha \quad ,$$

where α ranges over the four cell vertices.

Momentum cells are defined as surrounding a vertex x_{ij}, with cell edges meeting the midpoint of the surrounding normal cell edges, and vertices places appropriately within the surrounding normal cells to cover one quarter of the surrounding cells. There are four faces or edges for a normal cell and eight for a momentum cell. The coordinates, velocity and areas of surrounding momentum cell are assigned to the mesh points. Cell areas, pressure, internal energy, mass density are assigned to the cell centers. In KIVA, this two-dimensional formulation is extended to three dimensions. Each vertex is denoted by three indices $x_{i,j,k}$. Areas in the above become volumes, while edges become cell faces.

In a finite-volume discretization scheme, all the quantities related mesh are re-computed for each movement in the mesh for a Lagrangian mode. These quantities are:

V_{ijk} = Volume of normal cell computed from vertex position.
V'_{ijk} = Volume of momentum cell.
M_{ijk} = Mass of normal cell, $M_{ijk} = \rho_{ijk} V_{ijk}$.
M'_{ijk} = Mass of momentum cell, $M'_{ijk} = \rho_{ijk} V'_{ijk}$.
A_α = Area vector (outward) associated with a normal cell.
A'_α = Area vector (outward) associated with a momentum cell.
$(uA)_\alpha = u_\alpha \cdot A_\alpha$, cell face velocity in the normal direction.
$(uA')_\alpha = u_\alpha \cdot A'_\alpha$, momentum cell face velocity in the normal direction.

For spatial discretization, the volume integrals are converted to surface integrals using the divergence theorem, i.e., volume integrals are equated to integral of a given over the surface times the unit normal. The integrals are approximated with quadrature rules, i.e., function value at the cell center times the cell volume to approximate the volume integral. For example, consider the momentum equation 2.31. The Lagrangian form of this equation for a cell D is, in integral form

$$\begin{aligned}\frac{\mathrm{d}}{\mathrm{d}t}\int_{D(t)} \rho \boldsymbol{u}\,\mathrm{d}x &= \int_{D(t)} \rho \boldsymbol{g}\,\mathrm{d}x + \int_{D(t)} \boldsymbol{F}^{\mathrm{S}}\,\mathrm{d}x - \frac{1}{\alpha^2}\oint_{\partial D(t)} p\boldsymbol{n}\,\mathrm{d}s \\ &+ \oint_{\partial D(t)} \boldsymbol{n}\cdot\overline{\sigma}\,\mathrm{d}s - A_0\frac{2}{3}\oint_{\partial D(t)} \rho k \boldsymbol{n}\,\mathrm{d}s \quad . \end{aligned} \tag{6.1}$$

Approximating the integrals with the function evaluated at the mesh point x_{ijk} times the volume of the momentum cell D and the surface integrals by summation

of the area integrals over the faces of cell D (where the area integral is the function value at face center times the face area), we get

$$\begin{aligned}\frac{\mathrm{d}}{\mathrm{d}t}\left[\left(\rho_{ijk}\boldsymbol{u}_{ijk}\right)V'_{ijk}\right] &= \rho_{ijk}\boldsymbol{g}_{ijk}V'_{ijk} + \boldsymbol{F}^{\mathrm{S}}{}_{ijk}V'_{ijk} - \frac{1}{\alpha^2}\sum_{\beta} p_\beta \left(A'\right)_\beta \\ &+ \sum_{\beta}\overline{\sigma}_\beta \cdot \left(A'\right)_\beta - A_0\frac{2}{3}\sum_{\beta}\rho_\beta k_\beta \left(A'\right)_\beta \quad . \end{aligned} \tag{6.2}$$

Setting the momentum cell mass as $M'_{ijk} = \rho_{ijk}V'_{ijk}$, we get

$$\begin{aligned}\frac{\mathrm{d}}{\mathrm{d}t}\left[\left(M'\right)_{ijk}\boldsymbol{u}_{ijk}\right] &= \boldsymbol{g}_{ijk}M'_{ijk} + F^{S}{}_{ijk}V'_{ijk} - \frac{1}{\alpha^2}\sum_{\beta} p_\beta \left(A'\right)_\beta \\ &+ \sum_{\beta}\overline{\sigma}_\beta \cdot \left(A'\right)_\beta - A_0\frac{2}{3}\sum_{\beta}\rho_\beta k_\beta \left(A'\right)_\beta \quad . \end{aligned} \tag{6.3}$$

The remaining equations for species, total mass and energy are discretized in a similar fashion. The time derivative will introduce the usual advection term via the Reynold's transport theorem.

6.2 Temporal Discretization with the ALE method

The temporal differencing is performed with respect to a sequence of discrete time steps. Each time interval represents a cycle of calculation. Each cycle is completed in three phases. Phase A and B constitute the Lagrangian calculation in which the computational cells move with the fluid. In phase C, the flow field is frozen and remapped to a new computational mesh in order to account of compression or expansion. Such a cycle is shown in Figure 6.2. Phase A involves the calculation of spray droplet collisions and breakup, mass and energy source terms due to chemistry. The PDF generation and integration to calculate the source terms is performed in this phase.

6.2.1 Temporal Differencing for Chemistry Source Terms

The progress variables, mixture fraction and temperature define a point in the ILDM table. Each point also has a rate for the progress variable, which is used to explicitly calculate the values at next time step,

$$Y^{n+1}_{\mathrm{CO_2}} = Y^{n}_{\mathrm{CO_2}} + \dot{Y^{n}_{\mathrm{CO_2}}} \cdot \Delta t^n \quad . \tag{6.4}$$

For the new ILDM state at time $n+1$, the concentrations for the rest of the species are looked up from the ILDM table. The time step for chemistry is obtained from the ILDM characteristic time (see Section 5.3) termed as Δt^{ILDM}. So the above equation transforms to

$$Y^{i+1}_{\mathrm{CO_2}} = Y^{n}_{\mathrm{CO_2}} + \dot{Y^{i}_{\mathrm{CO_2}}} \cdot \Delta t^{\mathrm{ILDM}} \quad . \tag{6.5}$$

This time stepping is performed several times sequentially to obtain the CFD time step, such that

$$\sum_{i=1}^{k} \Delta t_i^{\mathrm{ILDM}} = \Delta t^n \quad . \tag{6.6}$$

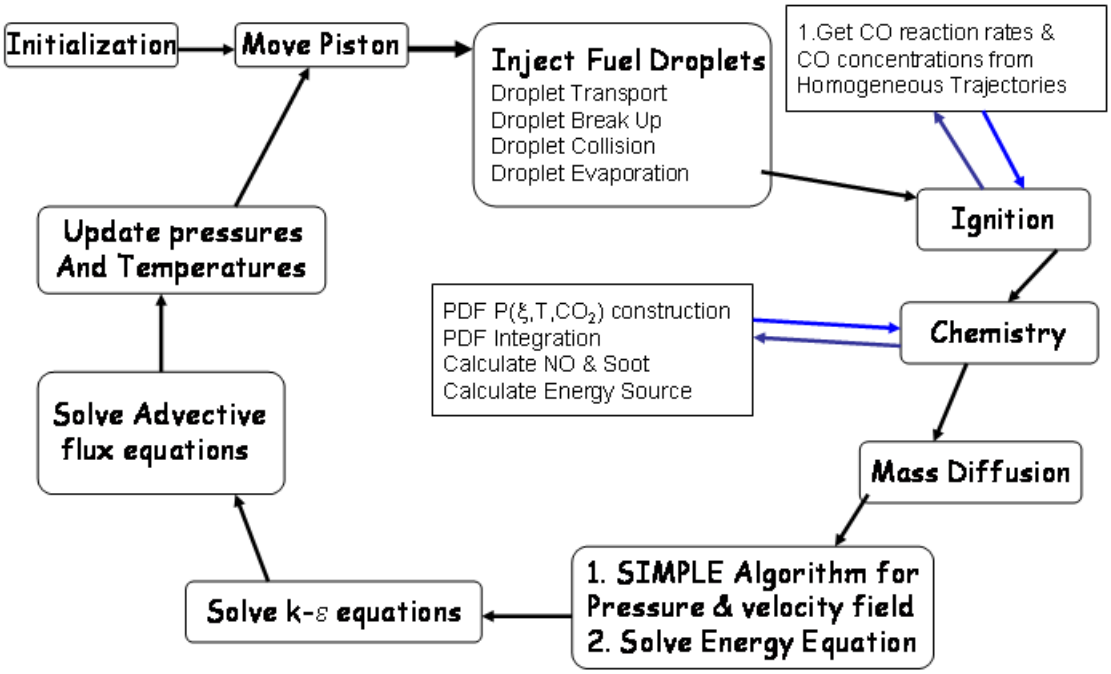

Figure 6.2: The overall sequence of calculations with the ILDM coupling for one time cycle after initialization.

6.2.2 KIVA - ILDM Coupling

The chemistry model uses the means of mixture fraction, temperature and the progress variables plus the variance of mixture fraction. All quantities are obtained by solving their respective transport equations. They are used to construct a joint PDF. The joint PDF is approximated by individual PDFs for mixture fraction, temperature and CO_2 mass fraction. Each PDF is discretized with the help of 40 points. The number of points can be varied as an input parameter. The joint PDF therefore consists of 40x40x1 points (since a delta PDF is used for CO_2 mass fraction). For each of these points, which represent instantaneous values, the reaction rate of the progress variable is read from the ILDM table. Using the rate, the value at the next time step is calculated explicitly. At the new value of the progress variable, the remaining species are read from the ILDM table. These are integrated by a Gaussian quadrature method to give the mean values. The mean values thus obtained are fed back to the flow solver.

6.2.3 Temporal Differencing of Flow Variables

All time derivatives in KIVA are approximated with first order difference, i.e.,

$$\frac{\partial Q}{\partial t} \approx \frac{Q^{n+1} - Q^n}{\delta t^n} \quad . \tag{6.7}$$

Each time step computation is performed in three phases. The results from phase A are denoted with Q^A and used in phase B producing results Q^B. The flow of time computation is

$$Q^n \longrightarrow Q^{\mathrm{A}} \longrightarrow Q^{\mathrm{B}} \longrightarrow Q^{\mathrm{B}} \longrightarrow Q^{\mathrm{C}} \longrightarrow Q^{n+1} \tag{6.8}$$

The time discretization in KIVA is performed in a variably implicit fashion using an implicitness parameters Φ_i, where i denotes any of the variables. It allows to produce a continuous range of approximations from fully implicit to fully explicit. For the case of momentum equation, we get

$$\begin{aligned}
\frac{(M')^{n+1}_{ijk}\boldsymbol{u}^{n+1}_{ijk} - (M')^n_{ijk}\boldsymbol{u}^n_{ijk}}{\Delta t} &= \boldsymbol{g}_{ijk}{M'_{ijk}}^n + \left(\boldsymbol{F^S}_{ijk}V'_{ijk}\right)^n \\
&- \frac{1}{\alpha^2}\sum_\beta \left[\Phi_{\mathrm{p}} p^{n+1}_\beta + (1-\Phi_p)\, p^{n+1}_\beta\right](A')^n_\beta \\
&+ \sum_\beta \left[\Phi_D \overline{\sigma}\left(\boldsymbol{u}^{n+1}\right) + (1-\Phi_D)\,\overline{\sigma}\left(\boldsymbol{u}^{n+1}\right)\right]_\beta \cdot (A')^n_\beta \\
&- A_0\frac{2}{3}\sum_\beta \rho^n_\beta k^n_\beta\,(A')^n_\beta
\end{aligned} \tag{6.9}$$

The parameters Φ_p and Φ_{D} are the implicitness parameters for pressure and strain. An advection term is required to be added on the left hand side of this equation. This term is calculated explicitly in the Phase C of the time computation. All other transport equations are discretized in a similar manner.

6.3 Coupled Implicit Solution

To obtain the time-advanced pressure forces in the Lagrangian part of the calculation, an implicit diffusion iteration is performed. It is called the outer iteration. In an explicit method, pressure forces can advance one cell at a time. If the time step is too large, inaccuracy and instability results. In an ideal situation, velocities at a new time step would be computed from time-advanced pressure gradients. This requires an iterative solution because pressure gradient themselves depend on velocity field and acceleration. Therefore, the popular SIMPLE algorithm [157] is used, which works as follows:

1. Compute the volume V^* after moving the cell with current velocity $\boldsymbol{u}$,
2. Compute approximations for density using V, V^*, pressure,
3. Compute a corrected pressure p^c using current pressure, density , internal energy and velocities,

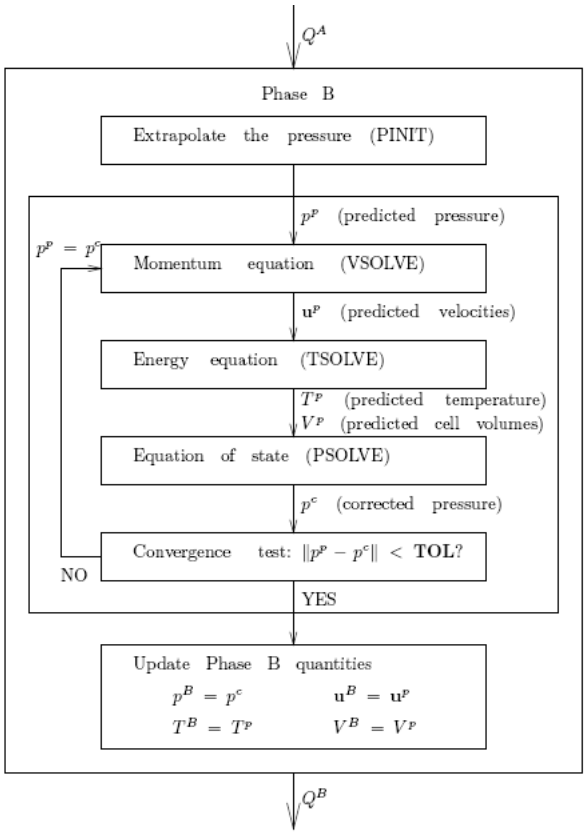

Figure 6.3: The modified SIMPLE algorithm for the case of KIVA. Names in brackets indicate the names of subroutines in the code.

4. Compute new velocities using corrected pressure,
5. If $(\|p - p^c\|) < TOL$ i.e the error is within tolerance limits, then quit, else go back to 1.

The modified version of the SIMPLE algorithm is shown in Fig. 6.3. The modification is extrapolation of the pressure followed by iterative solution for the velocities, temperature and finally pressure [18]. This modification is employed to update the pressures to time level in phase B using a linear extrapolation. The pressure is predicted according to

$$p^p_{ijk} = \left(p^{\mathrm{B}}_{ijk}\right)^{n-1} + \frac{\Delta t^n}{\Delta t^{n-1}}\left[\left(p^{\mathrm{B}}_{ijk}\right)^{n-1} - \left(p^{\mathrm{B}}_{ijk}\right)^{n-2}\right] \quad , \tag{6.10}$$

where p^{B}_{ijk} is the phase B pressure from the previous time step $n-1$. The predicted velocities are computed by solving the momentum equations after employing the previously predicted pressures(see Appendix L of [18]). An alternating node coupler strategy is used to control parasitic pressure modes. The implicitness factor is

computed dynamically (see Appendix H of [18]).

$$\begin{aligned}\frac{(M')^{n+1}_{ijk}\boldsymbol{u}^{\mathrm{p}}_{ijk} - (M')^{n}_{ijk}\boldsymbol{u}^{n}_{ijk}}{\Delta t} &= \boldsymbol{g}\,(M')^{n}_{ijk} + \frac{\left(R'_{ijk} + S'_{ijk}\boldsymbol{u}^{\mathrm{p}}_{ijk}\right)}{\Delta t} \\ &- \frac{1}{\alpha^n}^{2}\sum_{\beta}\left[\Phi_{\mathrm{p}}p^{\mathrm{p}}_{\beta} + (1-\Phi_{\mathrm{p}})\,p^{n}_{\beta}\right](A')^{n}_{\beta} \\ &+ \sum_{\beta}\left[\Phi_{\mathrm{D}}\overline{\sigma}\,(\boldsymbol{u}^{p}) + (1-\Phi_{\mathrm{D}})\,\overline{\sigma}\,(\boldsymbol{u}^{n})\right]_{\beta}\cdot(A')^{n}_{\beta} \\ &- A_0\frac{2}{3}\sum_{\beta}\rho^{n}_{\beta}k^{n}_{\beta}\,(A')^{n}_{\beta} - \frac{(M')^{n}_{ijk}\,(ANC)_{ijk}}{\Delta t} \quad (6.11)\end{aligned}$$

The quantity ANC represents the alternate node coupler used to control parasitic modes, described in Appendix L of [18]. The R_{ijk} and S_{ijk} terms arise through the gas and droplet velocity source terms. The linear system of momentum equations is solved using a conjugate residual method.

The predicted temperature is computed by solving the equation obtained from the energy equation and an equation of state in addition to the momentum equation. The solution also produces new cell volumes using the equation of state.

The calculation of corrected pressure involves the simultaneous solution of the equations for corrected cell face velocities, corrected cell volumes and corrected pressure. A linearized form of the state equation connects the cell face velocities and cell volumes. These equations are solved in a coupled fashion using the conjugate residual method. A description on the conjugate residual method can be found in [158]

6.4 Computer Code

The original computer code was modified by adding several subroutines to incorporate the PDF formulation, calls to ILDM libraries, PDF integration, NO and soot calculations and the calls to one-step chemistry with temperature PDF for pollutant calculation for the cases of ILDM failure. A customized input file is used to control the code which has choices for:

1. ILDM or 1-step chemistry.
2. Number of progress variables (1 or 2).
3. NO and soot modeling.
4. Including prompt NO calculation.
5. Turning the radiation on or off.
6. Number of PDF points.
7. Time step during ignition.
8. Representative ILDM pressure.
9. Wall emissivity in radiation calculations.

Chapter 7

Results and Discussions

Results from any simulation are only as good as the input given to the modeling code. A comparison with experimental data can reveal the accuracy and validity of the results. A set of experimental data for a Caterpillar 3406 heavy-duty truck engine is available [159] for this purpose. Specifications of this engine are given in the next section. The measured quantities include average pressure, average temperature, heat release rate, NO_x and soot concentrations. Additional qualitative description of the engine can be performed by analyzing the flame propagation, flame shape, scalar dissipation rates, ignition locations and ignition-delay.

In any CFD simulation, it is vital to ensure that the results are not dependent on the utilized mesh. This can be accomplished by using successively denser meshes and halting at the step after which no change in results is found. Meshes of three different densities are utilized in this study, and the medium dense mesh is found suitable for the computations. A brief description is given in the next section. The effect of several parameters is studied and is evident from the titles of the following sections.

7.1 Engine Specifications and Mesh

The Diesel engine simulated is rated 54 kW at 2100 rpm (rotations per minute). The design details and initial conditions are given in Tables 7.1 and 7.1. Experimental data is available for partial load condition with an rpm of 1600. All walls are maintained under constant temperature. The temperature measurement of inlet air had an error of about 10-15 K, which is adjusted to match to the temperature at injection from simulation to that of experiment under cold flow condition. Homogeneous turbulence is assumed at the time of intake valve closure, occurring at -137^o ATDC (After Top Dead Center). The exhaust valve opens at 130^o ATDC, and simulations are performed only for the duration between these two valve events. Initial values of the turbulence parameters k are calculated based on a recommended 10% turbulence level. The value of ϵ is calculated fom the value of k and a length of 1.432 cm. The results are insensitive to these values as reported previously [33].

A $1/6^{\text{th}}$ sector is used to take advantage of the periodic symmetry, established due to the 6 injector nozzles, since it reduces the computation time. The numerical

Bore	137.16 mm
Stroke	165.1 mm
Connecting Rod Length	263 mm
Engine Speed	1600 rpm
Number of Nozzle Orifices	6
Injection Timing	-7°, -4°, -1°, 2°, 5° ATDC
Duration of Injection	19.75°
Fuel Injected	0.168 g/cycle
Cylinder Wall Temperature	433 K
Piston Wall Temperature	553 K
Head Temperature	523 K
Initial Gas Temperature	361±15 K
Spray Temperature	341 K

Table 7.1: Caterpillar-3401 engine specifications.

Initial Gas Composition (g/cm^3)			
O_2	N_2	CO_2	H_2O
4.6012×10^{-4}	1.5337×10^{-3}	2.8579×10^{-6}	1.2579×10^{-6}

Table 7.2: Engine conditions at the time of inlet valve closure.

mesh used is shown in Fig. 7.1 and Fig. 7.2. All meshes are created using the K3-prep preprocessor for KIVA. The coarse mesh contained about 15780 cells, while the medium dense mesh had 23325 cells and the dense mesh had 35929 cells at BDC, for a 1/6 sector of the geometry. Cold flow simulation is the simulation of the engine

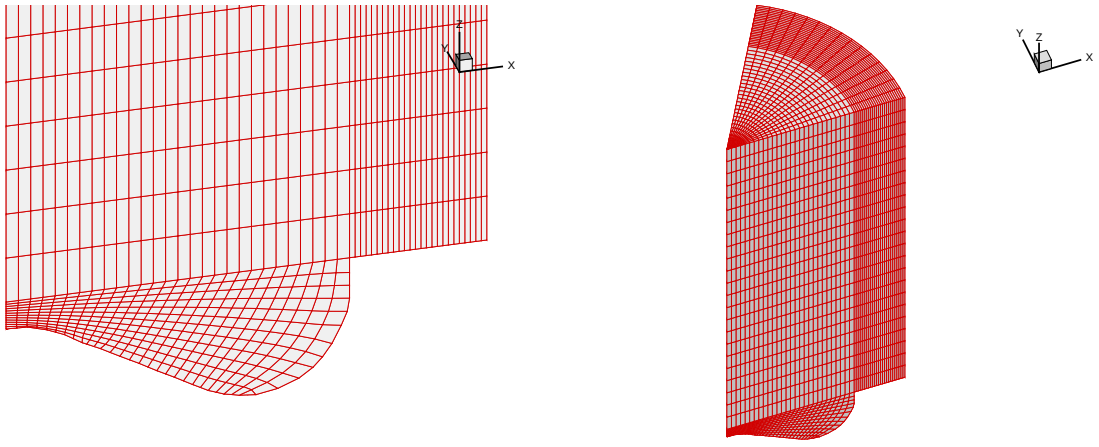

(a) Bowl Region (b) Full View

Figure 7.1: A medium-density numerical mesh.

process from the BDC (Bottom Dead Center) to the point of injection. As the air in the combustion chamber is pressurized due to the movement of the piston, its temperature also rises. A rise in the turbulence parameters like k and ϵ can also occur.

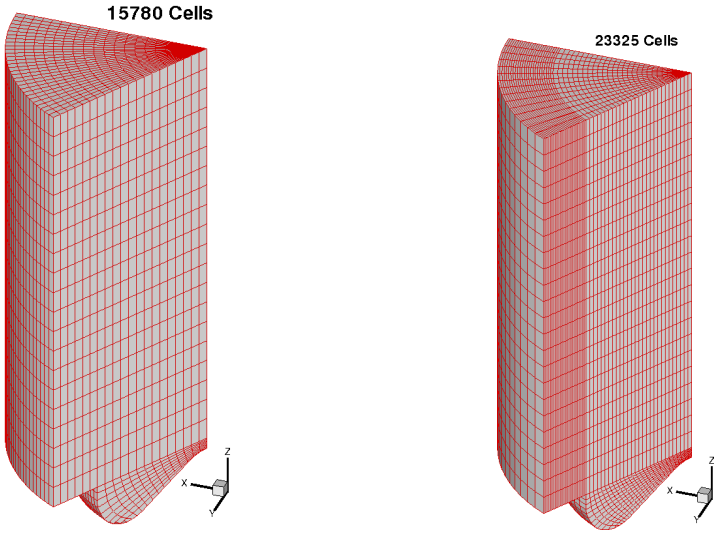

(a) Medium Dense Mesh

(b) Medium Dense Mesh with Fine Boundary Layer

Figure 7.2: Meshes of different densities.

7.2 Ignition and Flame Propagation

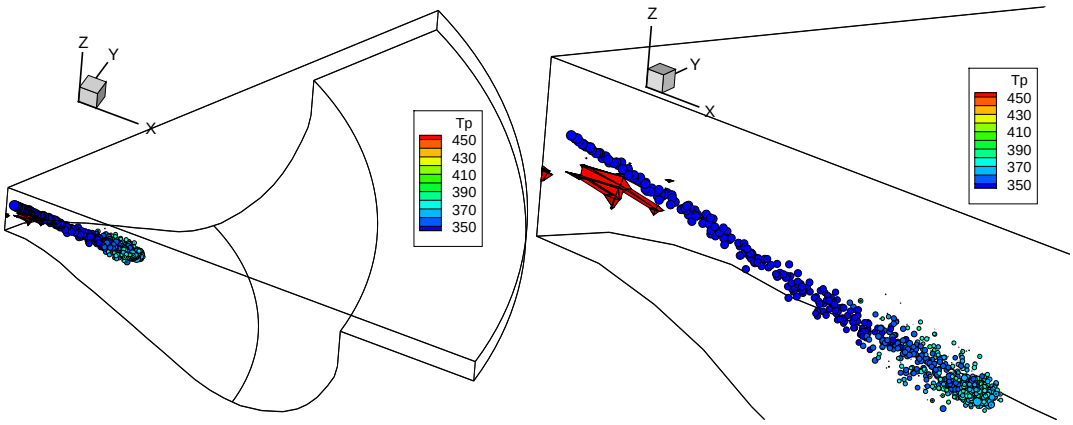

(a) Ignition Cell

(b) Close-up View

Figure 7.3: Location of the first ignition cells relative to the spray for the case of SOI -7° ATDC. Scale shows droplet temperatures T_{p}.

The hydrocarbon fuel (n-heptane in this case) decomposes to intermediate species such as alkylperoxy radicals and alkyl peroxides. After the radical pool is built-up during the ignition-delay time, a sudden rise in temperature due to heat release

from rapidly progressing reactions marks the beginning of ignition. The very first few cells where ignition occurs can be traced and are shown in Fig. 7.3.

The larger and colder droplets are closer to the injection. As they travel downstream, they are broken down or are evaporated due to rise in temperature by absorption of heat from surrounding gas, and finally release the fuel in gaseous form. As can be seen, ignition occurs in a location on the fringes of the spray, and some distance downstream. The residence time and the temperatures close to the injector are too small for ignition to occur. It has been reported in previous studies that oxidation of the initial mixture takes place on the side surface of the spray relatively close to the nozzle, even before the spray fully develops [160], and is confirmed in this study. The circles denote spray droplets colored by temperature and are sized by the droplet diameter. Literature reports that, when more than one reaction con-

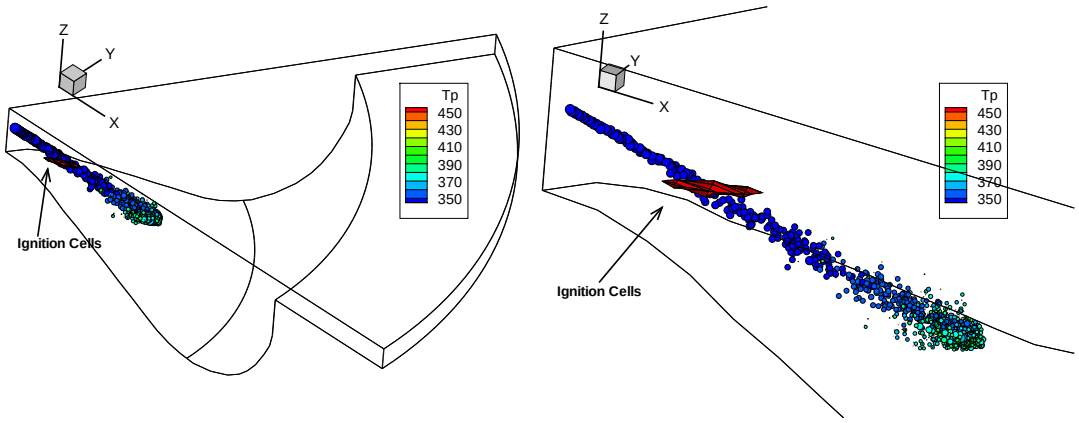

(a) First Ignition Cell (b) Close-up view

Figure 7.4: Location of the first ignition cells relative to the spray for the case of SOI +5° ATDC. Scale shows droplet temperatures T_p. The size of circles reflects drop size.

tributes to heat release, the most reactive mixture fraction (defined loosely as the mixture fraction where ignition occurs) varies with time. The mixture fraction of the cells where ignition is reported is seen to vary with time and is in a range of few points on the leaner and richer side of the stoichiometric mixture fraction. It predominantly lies in the leaner side for late injection cases and rich side for early injection cases.

OH is one of the most important radical formed by the reaction of H atoms with molecular O_2. 80% of the O_2 is consumed via this route [161]. It is present predominantly in the flame front. Fig. 7.5, *a* through *f*, show a representative flame propagation in terms of an iso-surface of the mass fraction of OH radical. One can see that in the early stages the flame is on the outer edges of (see *a*) where the spray particles are (not shown in figure). It evolves in accordance with the shape of the piston head.

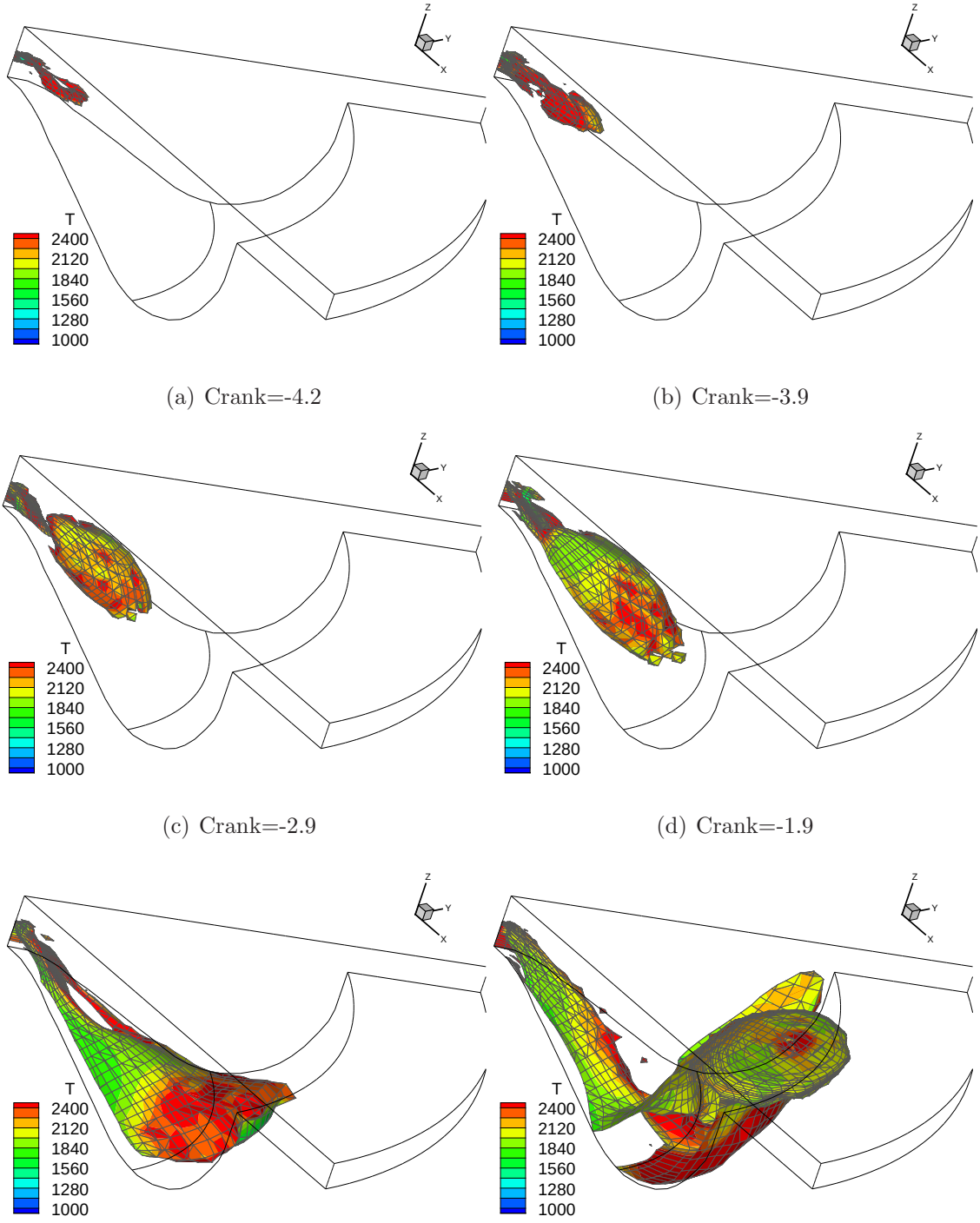

(a) Crank=-4.2

(b) Crank=-3.9

(c) Crank=-2.9

(d) Crank=-1.9

(e) Crank=+2.1

(f) Crank=+8.1

Figure 7.5: Propagation of the flame in terms of the iso-surface of mass fraction of OH radical at an arbitrarily chosen value of 1.0×10^{-3}. The surface is colored by temperature (K).

As the crank progresses, the flame spreads rapidly to engulf the entire space, turns upward and licks the cylinder head (see *f*) at a crank angle of +8° ATDC. The iso-surface is colored by the temperature, where one can notice the highest temperatures on the leading edge.

7.2.1 Ignition-Delay Timings

SOI (degree ATDC)	Engine simulation (seconds)	Homogeneous system (seconds)	Pressure @ignition (atm)
-7	3.53e-4	3.53e-4	79
-4	3.34e-4	3.66e-4	84
-1	3.07e-4	1.18e-4	85
+2	3.52e-4	1.3e-4	77
+5	3.75e-4	1.44e-4	69

Table 7.3: Ignition-delay timings in seconds.

The ignition-delay timings for the 5 case studies is listed below and is compared with the ignition-delay timings in a homogeneous system following a pressure profile of that of a Diesel engine. The pressure dependence of the ignition-delay time is

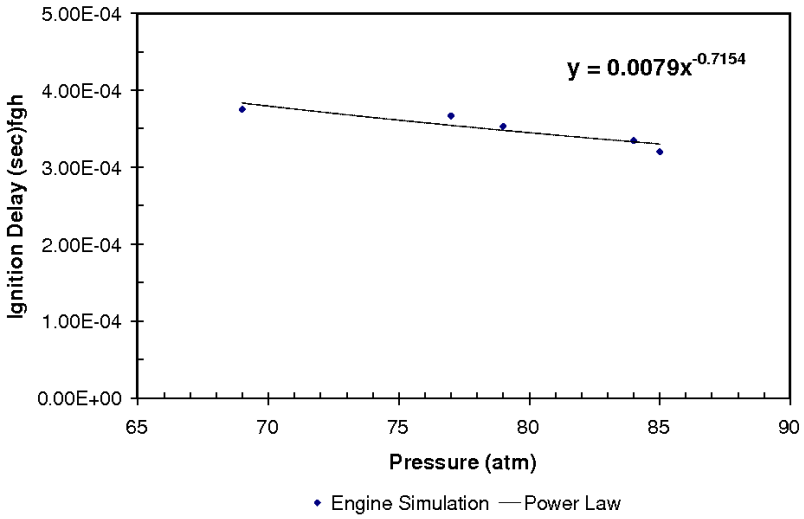

Figure 7.6: Ignition-delay as a function of pressure.

shown in Fig. 7.6, with the corresponding power relationships for engine simulation as well as homogeneous system. The observed dependence is consistent with those

reported by Liu et al. [162] for counterflow laminar jets and analytical solutions of Sheshadri et al. [163]. Increasing pressure results in an increase in reaction rates but also a shift from high-temperature ignition chemistry to low-temperature ignition chemistry. However, the former is much more significant, as reported by Liu et al. [162]. The autoignition model used thus captures this phenomenon well.

7.3 Temperature and Pressure Profiles

A comparison of pressures near the top dead center is as shown in Fig. 7.7. The pressures are slightly under-predicted near the top dead center but accurately predicted in the rest of the cycle. Experimental results show that the peak temperatures

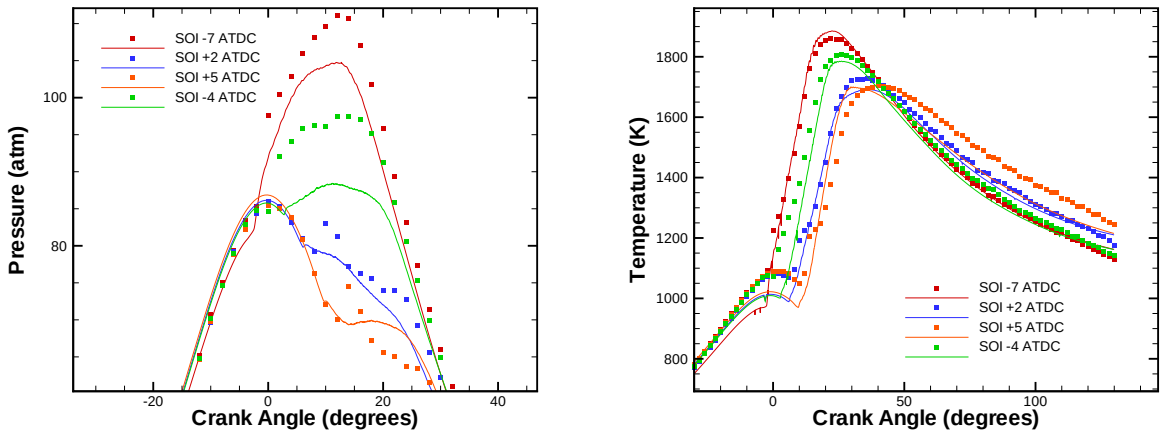

Figure 7.7: Variation in pressure and temperature profiles with SOI.

decrease (see Fig. 7.7) as the SOI (Start of Injection) is advanced. When fuel is injected prior to reaching the TDC, it is introduced in a flow that is further compressed. There is more amount of mass packed in the same amount of volume, and as heat is released after ignition, the peak pressures are also higher compared to the case of fuel injected after the TDC. This trend is very well predicted by the model as seen in the adjoining figure. When fuel is injected, the piston is in the downward motion, it faces velocities away from the TDC, consequently causing higher mixing levels. The level of mixing in such a case can be said to lie somewhere between premixed and non-premixed. It is then obvious that such a configuration will result in lower peak temperatures and lower NO_x concentrations. The streamlines for the cases of SOI2+ and SOI7- are shown in Fig. 7.8. The figure on the left shows a considerable upflow toward the engine head (i.e. velocity in the Z direction) in the region close to the nozzle. Contrastingly, the case of SOI 5+ shows a down-flow into the bowl. This flow behavior through its effect on mixedness at the time of injection is ultimately responsible for the differences in ignition-delay and pollutant concentrations.

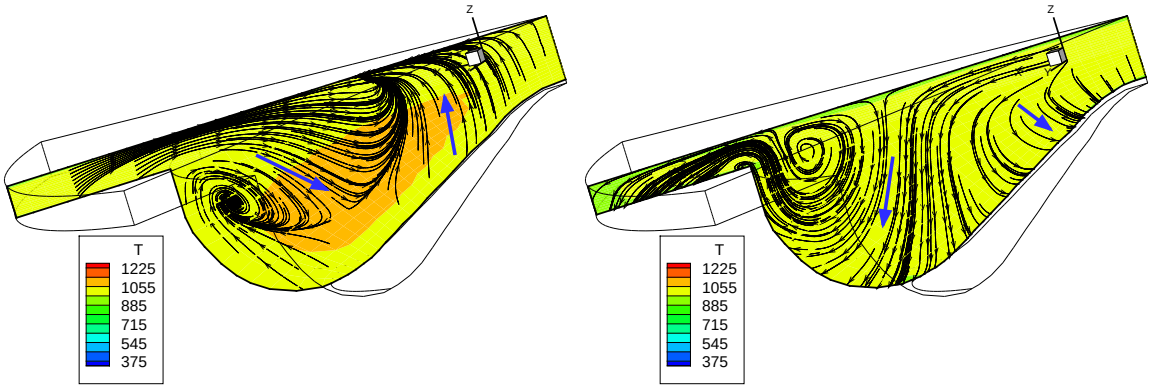

(a) SOI -7° ATDC (b) SOI +5° ATDC

Figure 7.8: Comparison of streamlines on a slice passing through the spray at the time of injection.

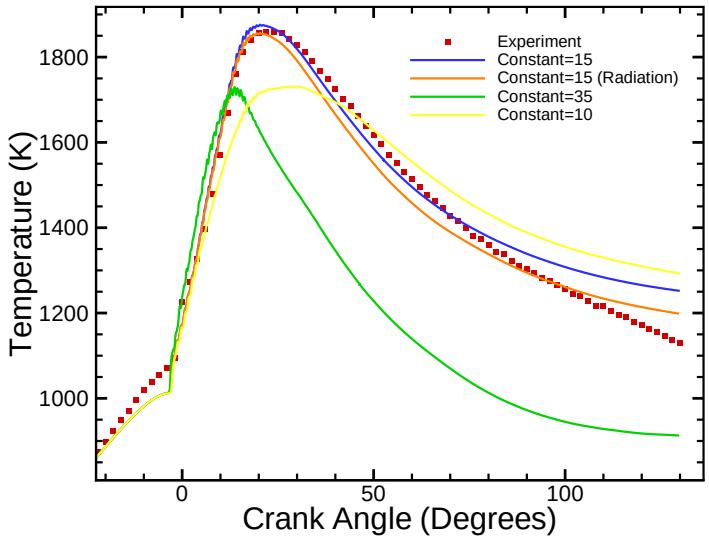

Figure 7.9: Effect of spray model constant on combustion.

7.4 Effect of Spray Model Constant

The typical range for the spray model constant B_1 is between 10 and 60 (see Section 3.3.2). Increasing the constant delays the ignition but reduces the peak temperatures. This is because a higher constant represents less disturbance in the droplets. Consequently, the droplets evaporate late and assure a fuel supply during the peak temperature regime. A decrease of the constant represents a higher instability in the droplets. As a result, droplets disintegrate faster and consequently have a higher rate of evaporation. The effect of this can be seen as a shortening of the ignition-delay time. It is also worth mentioning that the ignition-delay can additionally vary due to some other parameters such as the inlet spray temperature. A study with a one-step reaction mechanism for the case of SOI -7 degrees, with a mesh size of

about 15000 cells, is performed to study the effect of the spray model constant. It is found that a spray constant B_1= 15 (see Section 3.3.2) gave the most optimum results in terms of the average temperature profile. This value is used for all subsequent calculations.

7.5 Species Profiles

The time profile of various species reveals useful information about the progress of reaction. In this section, various species profiles from simulation results are discussed for the case of SOI -1° ATDC, as they evolve with increasing crank angle, reflecting progression of time. Fig. 7.10a shows the profiles (note the different axes for different species) for the major species CO, CO_2 and H_2O. The profile of fuel (C_7H_16) is shown as reference. As the injection proceeds, the fuel concentration rises to a peak value before being consumed by combustion. Some of the fuel is being consumed even when its overall concentration is rising, and is evident from the rapidly rising CO concentration.

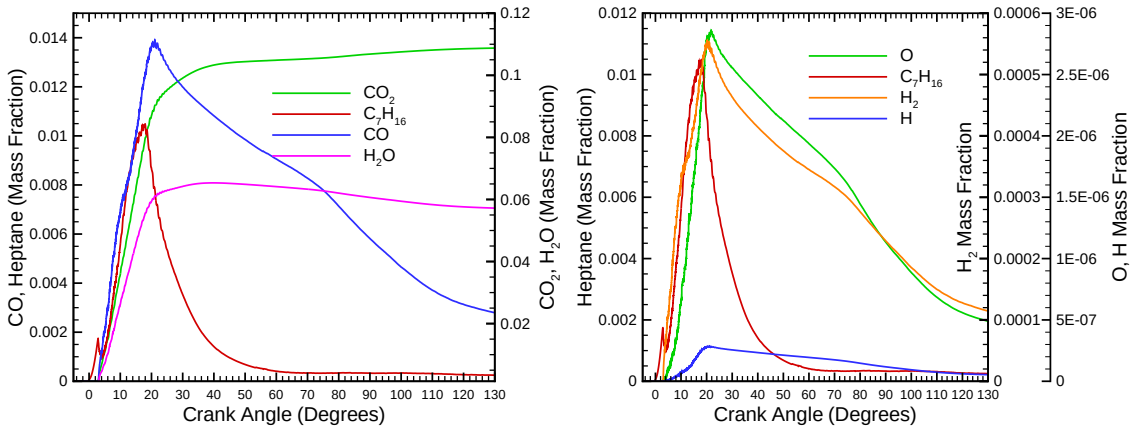

(a) CO, CO_2 and H_2O profile

(b) O, OH radical profile

Figure 7.10: Time profiles of CO, CO_2, H_2O, O, H and H_2 species for the case of SOI -1° ATDC.

At low temperatures (below 1000 K), n-heptane undergoes combustion via formation of peroxide radicals, its isomerization to hydroperoxy radicals and subsequent destruction of peroxide radicals (see Section 4.2 for details). The low-temperature chemistry was modeled in this work using a single representative species and details of the results are presented in 7.2. In the subsequent stage of high temperatures, combustion of n-heptane proceeds via the following processes:

1. Thermal decomposition of fuel by chain-initiation step in which the C-C bond is broken to form hydrocarbon radicals, the C-C bond being weaker than the C-H bond. This is the first stage of combustion.
2. Attack of O, OH and H atoms on the fuel and hydrocarbon radicals leading to the formation of alkyl radicals. The competing reactions with O and O_2 are less important. C_2H_4, CH_4, H_2 is the "actual fuel" that burns [161]

3. Thermal decomposition of alkyl radicals to form smaller alkyl radicals or H atoms by alkyl elimination, formation of CH_2O and CO. Item 2 and 3 comprise the second stage of combustion.
4. In all figures, the falling concentrations of intermediate species indicate the final self-accelerated stage of combustion.

Alkyl radicals (described in 2 above) give rise to methyl radicals by H atom abstraction. CO is an important intermediate species in the step to final conversion of the alkyl radicals to CO_2. It is formed by the reaction of CH_2O, which itself is produced from the methyl radicals. The CO concentration reaches a peak at a time slightly later that the peak fuel concentration, and then drops slowly, as it gets converted to CO_2. CO_2 concentration rises rapidly (but slower than CO) initially and at slow rate in the later part of the power stroke of the engine. It flattens out as combustion reaches completion.

Fig. 7.10b shows the profiles for the minor but important species H_2 (orange line), O (green line) and H atoms (blue line). As with any intermediate species, they rise rapidly (H_2 much more rapidly than O radical) and decompose slowly. The shape of OH profile resembles that of CO profile. The rapidly rising H_2 profile indicates that the C-H bonds are broken by abstraction of H atom at high temperatures leading to formation of H_2. Fig. 7.11a shows the profile of NO, for the same case SOI -1°

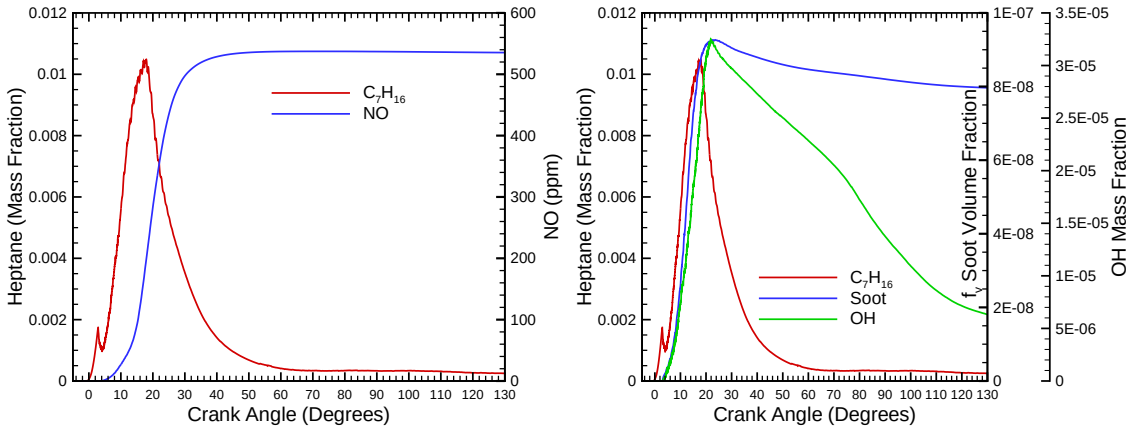

(a) NO_x profile (b) Soot profile

Figure 7.11: NO_x and soot profile for the case of SOI -1° ATDC.

ATDC. NO rises rapidly in the high-temperature portion of the cycle and reaches the peak value at +30° ATDC. It then levels off as combustion reaches completion, and the temperature drops in the later stages of the power stroke due to expansion of burned gas. The peak of NO also corresponds to the peak of temperature. The adjacent Fig. 7.11b shows the profile for soot volume fraction and OH radicals. Soot is produced via the formation of PAH (poly-aromatic hydrocarbons) from its precursors: C_2H_2 and C_3H_3. These precursors are formed during the decomposition of fuel. The peak soot value is seen at about +20° ATDC, which also corresponds to

the peak of most radical species and occurs before the peak of cylinder temperature. Thereafter, soot is oxidized by OH radicals, causing a decrease in both soot and OH radical concentration. However, OH is predominantly consumed by its reaction with CO, alkyl and formyl (HCO) radical species.

7.6 Soot Predictions

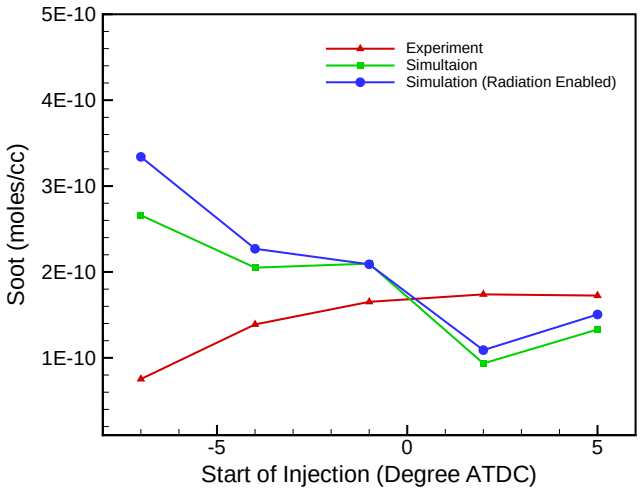

Figure 7.12: Soot values for several SOI timings.

Soot formation takes place in the rich regions of a flame where temperatures are between 1000 K - 2800 K. The fuel concentration peaks right after completion of injection. Usually the downstream regions of spray are richer in fuel and show a region of high soot formation. The soot concentration rises rapidly after injection, and a peak seen slightly after the peak of fuel concentration appears. As time progresses, diffusion of fuel and air leads to oxidation of some of the soot particles. As the valve closure approaches, combustion is near completion and only reduction in the soot concentration due to oxidation and coagulation can be seen in Fig. 7.12. A delayed injection timing causes higher peak fuel concentrations. Consequently one expects to see a rise in the soot peak and final concentrations. The model predicts the soot concentrations within the order of magnitude of the experimental data, although the variation with SOI does not show a clear trend.

In this work, only a representative pressure is used irrespective of the different pressures encountered in the five cases. This could be one of the reasons for the discrepancy in the sooting trend. The representative pressure (80 bar) used is closer to the pressures encountered in the last 3 cases, thus explaining their better match with experimental values.

Fig. 7.13a shows a slice through the engine cylinder for the case of SOI -1° ATDC at the time of peak soot concentration i.e at +30° ATDC. After comparing this figure with Fig. 7.13b one can see that peak soot concentrations are occurring in the high temperature zone. High soot concentrations are also seen in the fuel rich

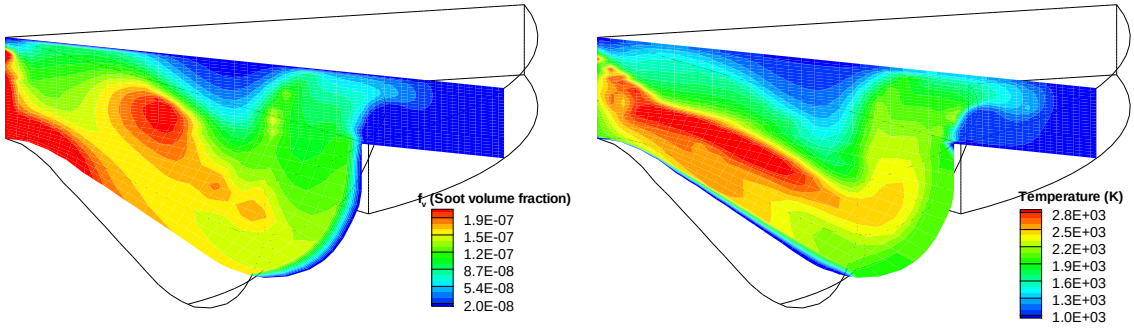

(a) Soot Volume Fraction (b) Temperature (K)

Figure 7.13: A slice showing soot volume fraction and temperature for the case of -1° SOI at the time of peak soot concentrations (19.9° ATDC).

areas (see Fig. 7.14a), while very low concentrations are seen in regions with high OH concentrations and high enough temperatures (see Fig. 7.14b), where soot can undergo oxidation reactions.

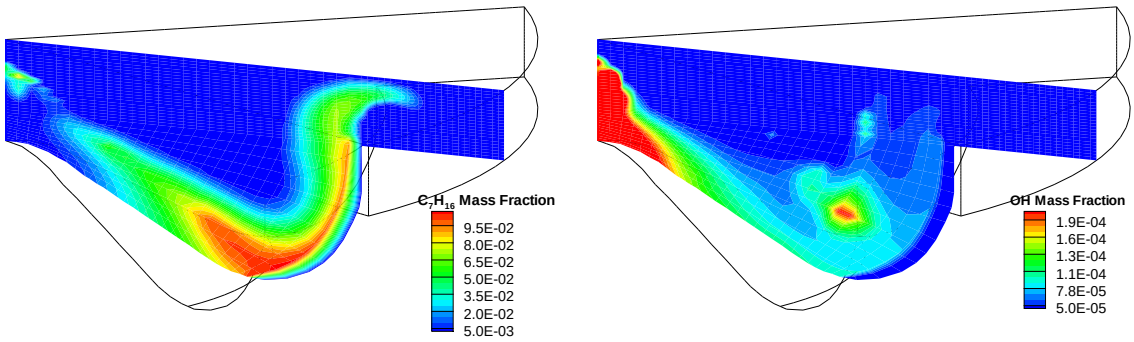

(a) Fuel Mass Fraction (b) OH Radical Mass Fraction

Figure 7.14: A slice showing fuel and OH radical mass fraction for the case of SOI -1° ATDC at the time of peak soot concentrations (19.9° ATDC).

7.7 Effect of Heat Transfer Models

Fig. 7.15(a) and (b) shows the comparison for old and new heat transfer model. The heat release rate is calculated for each cell by adding the incremental heat released for a given time step, obtained from the one-step or ILDM chemistry calculation. The average temperature profile in (a) indicates that the new models gives better results, provided the heat release rate for the new and old heat transfer models (HTM) being comparable, as is seen in (b). In the new model, the assumption of Reynolds' analogy is modified to account for the fluctuating nature of the flow (described in Section 3.2.2).

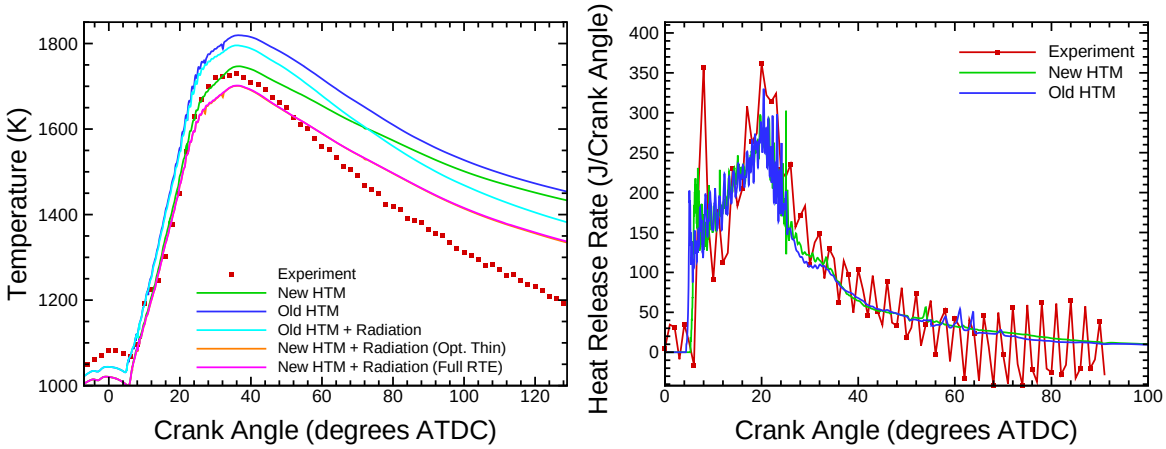

(a) Heat Transfer Models

(b) Heat Release Rate

Figure 7.15: Effect of heat transfer and radiation models on combustion. HTM stands for heat transfer model.

The increase in Prandtl number due to such oscillations leads to an enhanced level of heat transfer to the wall. This would mean more heat is removed from the bulk, consequently giving lower average temperatures. In line with this prediction, lower temperature is seen in the post TDC portion, where majority of heat release occurs, while the heat release rate remaining constant as seen in the adjoining figure. The trend remains true even after enabling radiation (both with optically-thin and the full RTE solution) shown by the corresponding light blue and pink lines lying on top of each other. The optically-thin medium assumption, which is used in this work, is known to over-predict radiative heat losses because it assumes that the heat transfer medium only emits radiation, and without absorbing any [46]. No difference is seen in the results for the optically thin- or thick-medium assumption. Therefore, all other calculations were performed using the optically-thin medium assumption.

7.8 NO Predictions

The radiation model adds a third mode of heat transfer. Radiation allows the transfer of heat without a medium and depends on the temperatures attained and the concentrations of radiating species. In spark-ignition engines, due to the small amount of soot formed, radiation is not an important mode of heat transfer. In Diesel engines, this situation is changes due to presence of significant soot. Since soot is predicted with much greater accuracy in the present work, and soot particles are considered to have a major effect on radiative heat transfer, it was expected that an enhanced heat transfer will be observed. The curves for temperature with and without radiation with a spray constant B_1 of 15 are shown in Fig. 7.15.

In Fig. 7.16, one can see how enabling radiation affects NO_x prediction. Since radiation enhances the rate of heat transfer away from high temperature regimes to the wall, it has the ability to reduce peak temperatures. Reduced peak temperatures slow down the temperature-dependent NO_x formation reactions. It is expected that

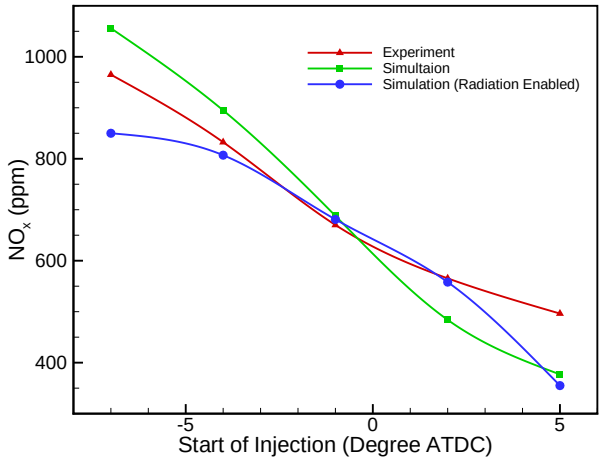

Figure 7.16: NO_x values for several SOI timings.

this would reduced the total amount of NO_x predicted. This is seen in the figure, at least for the injection timings occurring prior to TDC, due to the fact that the system has more flow time for these injection cases. For the cases of injection after the TDC, the effect of radiation is subdued.

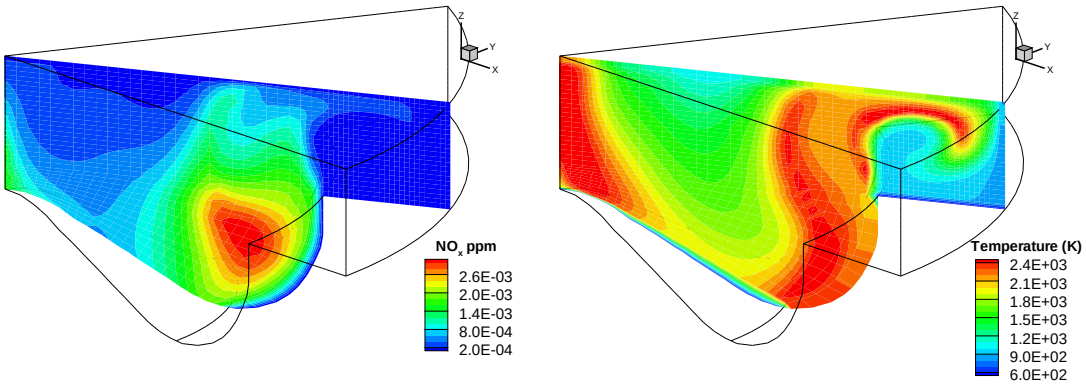

(a) NO Mass Fraction (b) Temperature (K)

Figure 7.17: A slice showing NO mass fraction and temperature for the case of -1 SOI at the time of peak NO concentrations (29.9° ATDC).

Thermal and prompt NO was predicted in the simulation using the reactions described in Section 4.3. Prompt NO is known to occur in the low-temperature stages and contribute only a minor portion to the total NO. The regions of NO formation can be examined by looking at contours of NO, temperature and fuel. A sectional view of the NO mass fraction distribution is shown in Fig. 7.17a for the case of -1 SOI at the time of peak NO concentrations (29.9° ATDC). Thermal NO is extremely sensitive to the temperature due to the large activation energy of the rate-controlling reaction. A comparison with the temperature distribution at the same location, shown in 7.17b, indicates that NO occurs wherever there is high temperature and lean fuel mixtures (see Fig. 7.18). Rich fuel mixtures have

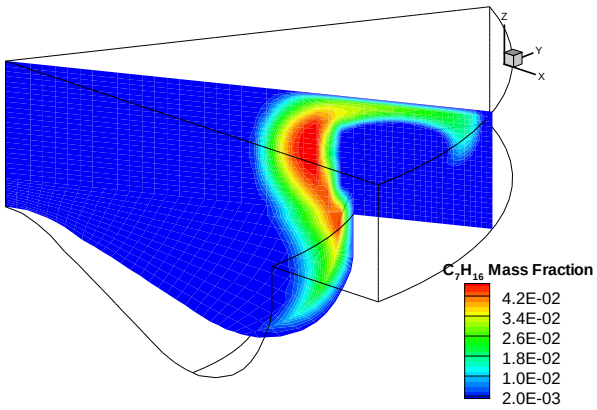

Figure 7.18: A slice showing fuel mass fraction for the case of -1 SOI at the time of peak NO concentrations (29.9° ATDC).

enough combustible species to compete with NO for reaction with O and O_2 species, preventing NO formation.

7.8.1 Parametric Comparison

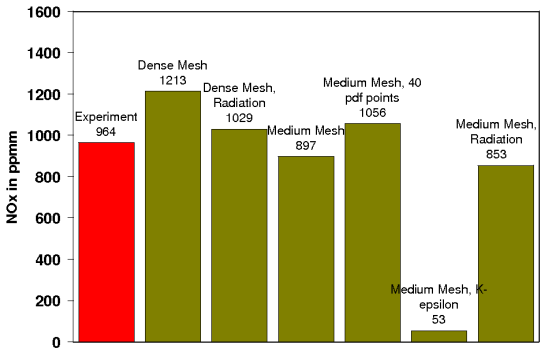

Figure 7.19: Comparison of NO_x value for various parameter studies for the case of -7 SOI.

The effect of several parameters on various flow and chemistry variables is studied, NO_x and soot being the most important. A medium sized mesh with 40 PDF points and radiation enabled gives NO_x values closest to those observed experimentally. The results from the coarse mesh and the regular k-ϵ turbulence models are relatively poor.

The use of a very dense mesh over-predicts NO_x values, possibly attributed to numerical errors introduced by skewed geometry of computational cells. Over-prediction is particularly undesirable considering the fact that the NO_x values need to be multiplied by a factor of 1.2 as suggested by Miyamoto et. al. [141] in order

to compensate for the difference in molecular structure of Diesel (actual fuel) and n-heptane (model fuel). A difference of 10% in the NO value was seen when the number of PDF points were increased from 20 to 40.

7.9 Strain Rate and Scalar Dissipation Rate

The progress of rate of strain and scalar dissipation rate (1/s) and temperature (K) is shown in the following three figures for the crank position of -1.9, -0.9 and 1.1 degrees for the case of SOI -7° ATDC on a iso-surface of stoichiometric mixture fraction. These crank positions correspond to the time frame shortly after ignition.

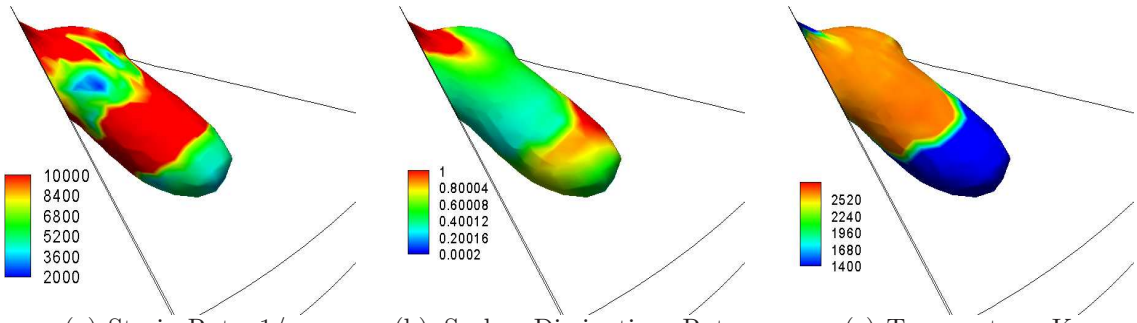

(a) Strain Rate, 1/s (b) Scalar Dissipation Rate, 1/s (c) Temperature, K

Figure 7.20: Strain rate, scalar dissipation rate and temperature shown on an stoichiometric iso-surface at -1.9° ATDC for the case of SOI at -7° ATDC.

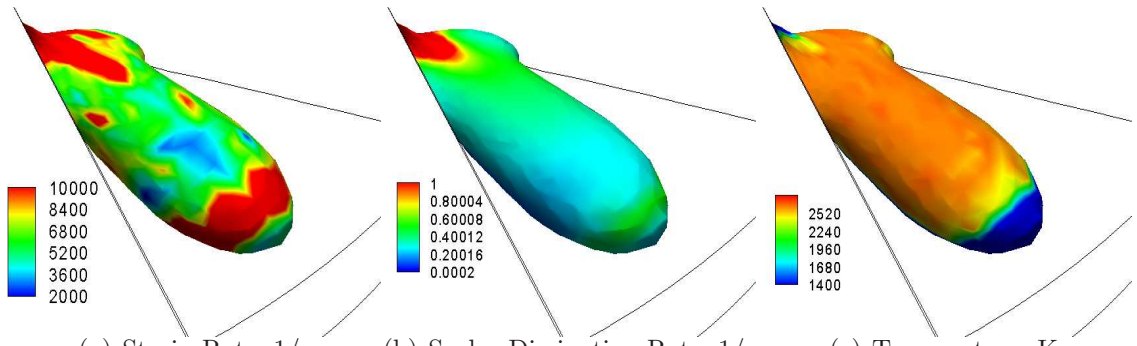

(a) Strain Rate, 1/s (b) Scalar Dissipation Rate, 1/s (c) Temperature, K

Figure 7.21: Strain rate, scalar dissipation rate and temperature shown on an stoichiometric iso-surface at -0.9° ATDC for the case of SOI at -7° ATDC.

In all the three figures, it can be noted that the very high scalar dissipation rates are restricted to the injection location, where no chemical reaction is occurring. The first high-strain region also occurs in the vicinity of injection. The progress of the thin reaction zone at the border of high temperature zone can be seen clearly. This zone also corresponds to the second high-strain region. Beyond the high-temperature region is a cold region where the fuel is yet to ignite. In the last figure, the second

high-strain zone has crossed the stoichiometric envelope. The temperature rises behind this region as it travels across the stoichiometric envelope. One can also see temperature regions in the form of thin flamelet like structures.

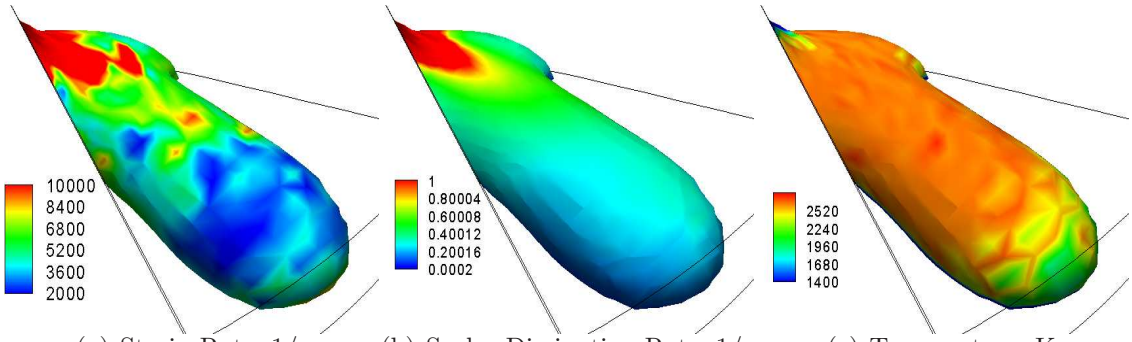

(a) Strain Rate, 1/s (b) Scalar Dissipation Rate, 1/s (c) Temperature, K

Figure 7.22: Strain rate, scalar dissipation rate and temperature on an stoichiometric iso-surface at 23.0° ATDC for the case of SOI at -7° ATDC.

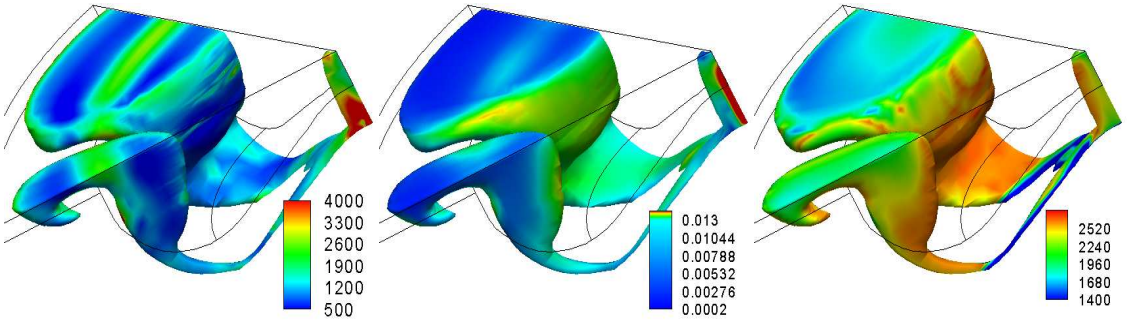

(a) Strain Rate, 1/s (b) Scalar Dissipation Rate, 1/s (c) Temperature, K

Figure 7.23: Strain rate, scalar dissipation rate and temperature on an stoichiometric iso-surface at 1.1° ATDC for the case of SOI at -7° ATDC.

In the fourth figure, 7.23, the same three variables are shown at a later crank position of 23 degrees, when the combustion has reached past its peak. The maximum values of scalar dissipation as well as strain rates are much lower than during the ignition period. The distribution is much variegated and the regions of high dissipation and strain rate values corresponding to relatively lower temperatures. This may indicate that diffusive losses at high strain rates inhibit reaction, resulting in extinction occurring in those computational cells.

Chapter 8

Conclusions

The simulation of turbulent flows is a challenging problem. The presence of reactions adds more complexity to this challenge. Ability to accomplish such a complex challenge within industrially viable computational and time resources with reasonable results is the prime goal of this work.

The results and discussions in the previous chapter leads one to conclude that ILDM provides a reasonable method of integrating kinetic rate laws for complex reaction mechanisms into the probabilistic description of turbulent flows. Choice of reaction variables can slightly affect the accuracy of the results.

The ignition model based on a stirred vessel results for the entire mechanism (including low-temperature HC reactions) gives ignition-delay times comparable to those insinuated by the experimentally measured heat release time profiles. Introduction of the RNG k-ϵ model and an enhanced wall heat transfer equation translate to better heat transfer and turbulence predictions in conformity with literature.

One can also conclude that the Zeldovich mechanism for NO_x prediction when used with concentrations of intermediate reactive species obtained from ILDM can enhance the accuracy of calculations by approximately 10-20 %. Similarly, soot predictions, using a phenomenological model that incorporates soot precursors from ILDM, can be obtained within 20-30 % of those obtained experimentally. NO_x is formed in the lean to stoichiometric regions of the flame and in contrast to soot, peaks in the post-flame regions. Soot rises rapidly after injection, and a peak is seen slightly after the peak of fuel concentration appears indicating that soot forms predominantly in the rich regions of the flame.

In all the temperature profiles, one can observe that there is a deviation from the experimental values before the injection begins. Initially it was believed that this could be due to the assumption of an ideal gas law. Implementing a better equation of state (Redlich-Kwong or Soave) failed to close this gap, and the problem could not be resolved. A reassessment of the pressure-temperature relationship is required to address this issue. In summary, all major parameters viz. temperature, pressure, heat-release rate as well as pollutants NO_x and soot are predicted satisfactorily. Although, commenting on the numerics of ILDM remains outside the scope of this

work, general observations regarding its functionality can be made. Enabling the simultaneous use of a zero rpv (equilibrium) in addition to the regular table will go a long way in addressing the issue of source terms where no ILDM points exist. The need to use a one-step reaction or model points and the inaccuracy that comes along with it can then be disregarded. There are several reasons to which, the mismatch between experimental data and simulation results, is attributable. Assumption of a uniform pressure for use with ILDM for all cases is one of them. When a one-step model is used when ILDM states cannot be found, the NO and soot calculations are performed using only a temperature PDF. Moreover, the concentrations of intermediate species thus obtained are not added to the respective cells but are used only for NO and soot calculations. This is to avoid errors in mass balance of the one-step chemistry calculation.

In spite of being a good and affordable method that has more value than just the purpose of demonstration, integrating ILDM into turbulent reactive flow simulation remains fraught with many disputable difficulties, the robustness of this method being the most questionable one. Results can be obtained only with several numerical limitations. One such limitation is the assumption of a statistical independence of the probability distributions of the T, ξ and rpv. The normalizations and time scale analysis used to address this assumption induces the numerical frailty in the simulation code. Future work could include implementing a method that eliminates such assumption and directly calculates the joint PDFs. The expense in terms of computational effort for such a method remains to be seen. However, one should consider the fact that this work is restricted to the application in an unsteady-state condition where the variation in the mixture fraction with time can be large. Therefore, at any given instant, only a certain range of the computational domain is treated with ILDM numerics.

Systems involving a steady-state flow e.g. a process heater, do not face this problem, except for a small region near the areas where fuel and air are mixed. In such a case, it is speculated that more accuracy and robustness can be achieved. Nevertheless, in its current form, the KIVA code coupled with ILDM is a good tool for simulating combustion processes in internal combustion engines and predicting NO_x and soot.

A further analysis using the strain rate and scalar dissipation rate to correlate the three PDFs (assumed independence) can be investigated.

Appendix A - Slices of 2-RPV Table

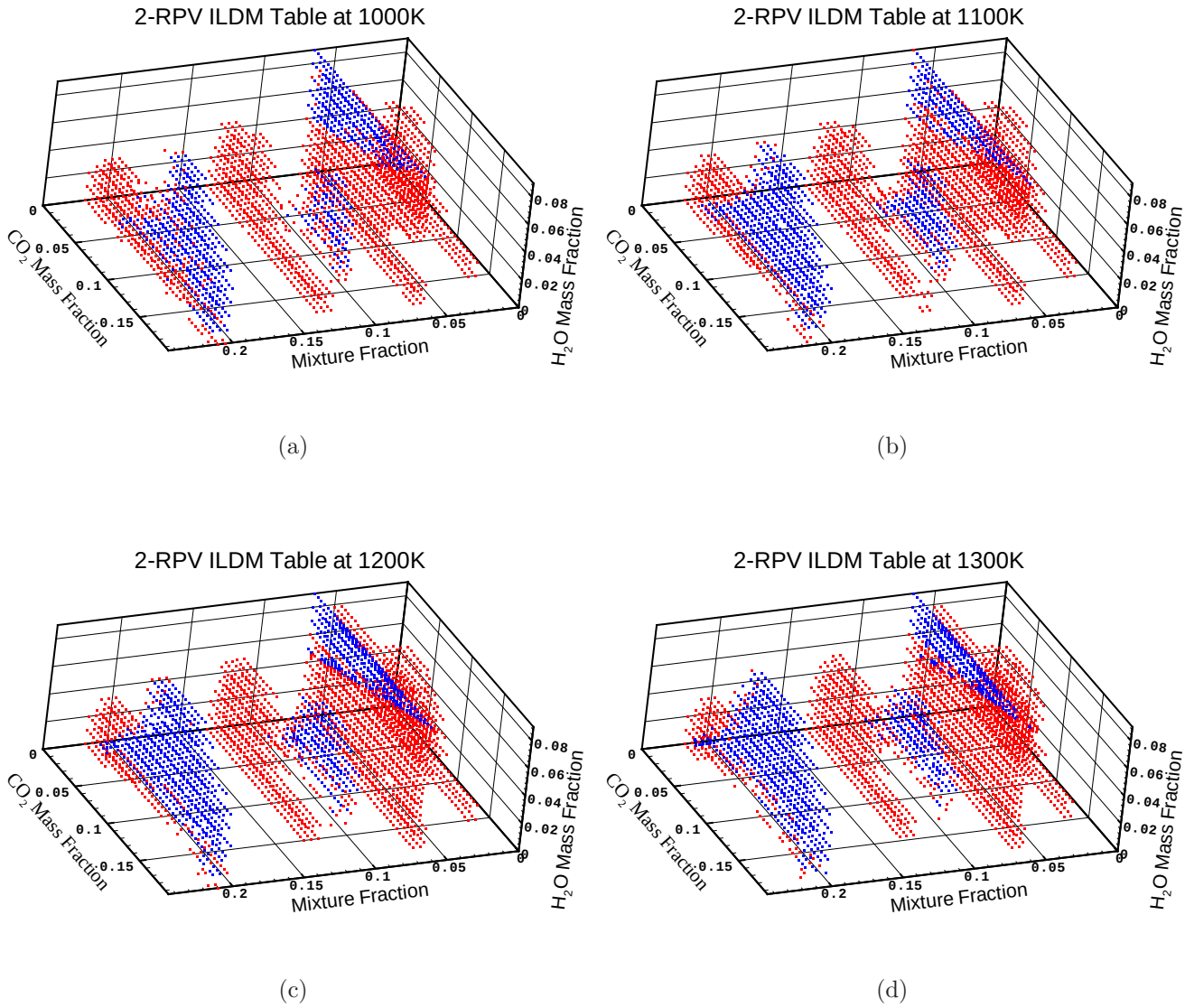

(a) (b)

(c) (d)

Figure 1: Slices of ILDM table with two reaction progress variables for heptane-air system at T=1000 K - 1300 K [139].

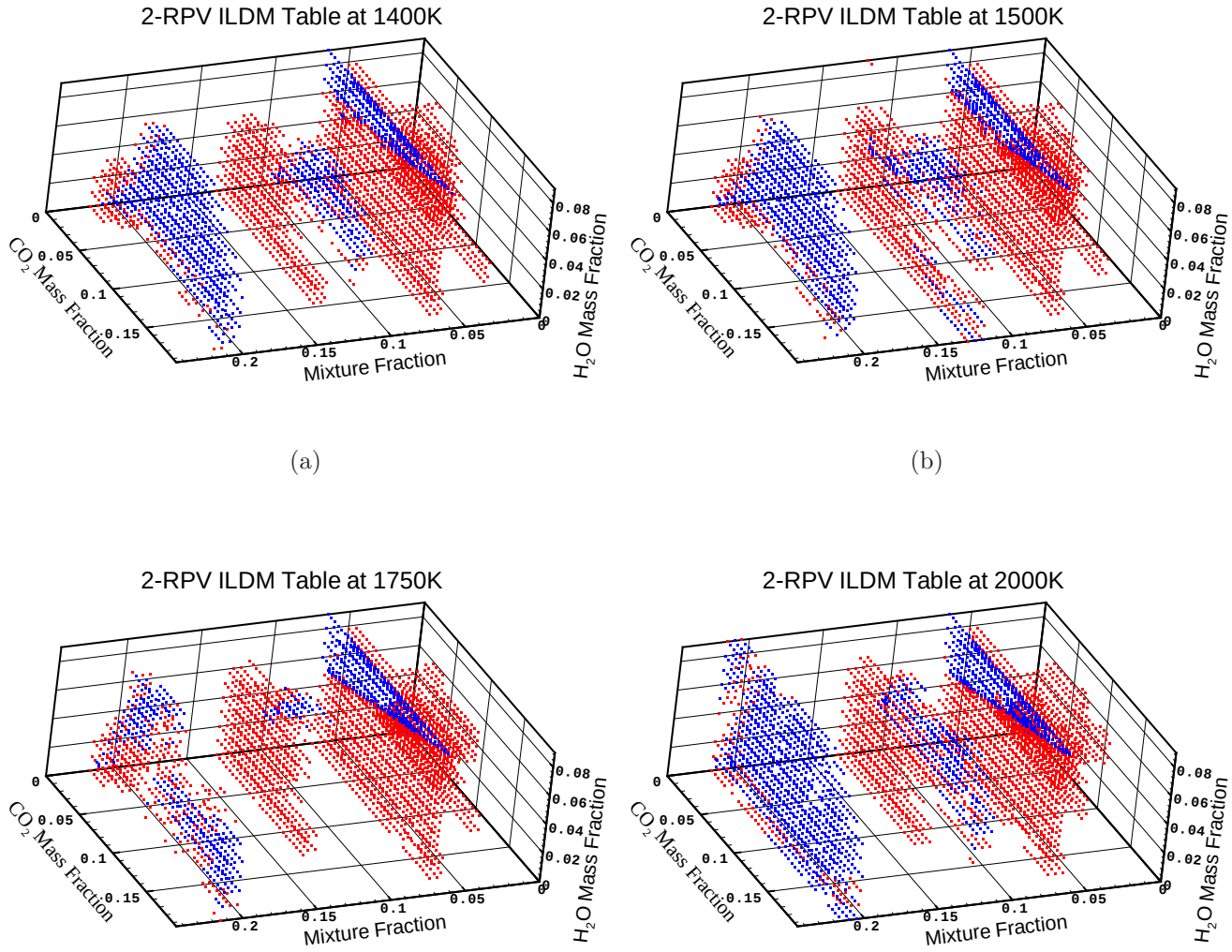

(a) (b)

(c) (d)

Figure 2: Slices of ILDM table with two reaction progress variables for heptane-air system at T=1400 K - 2000 K [139].

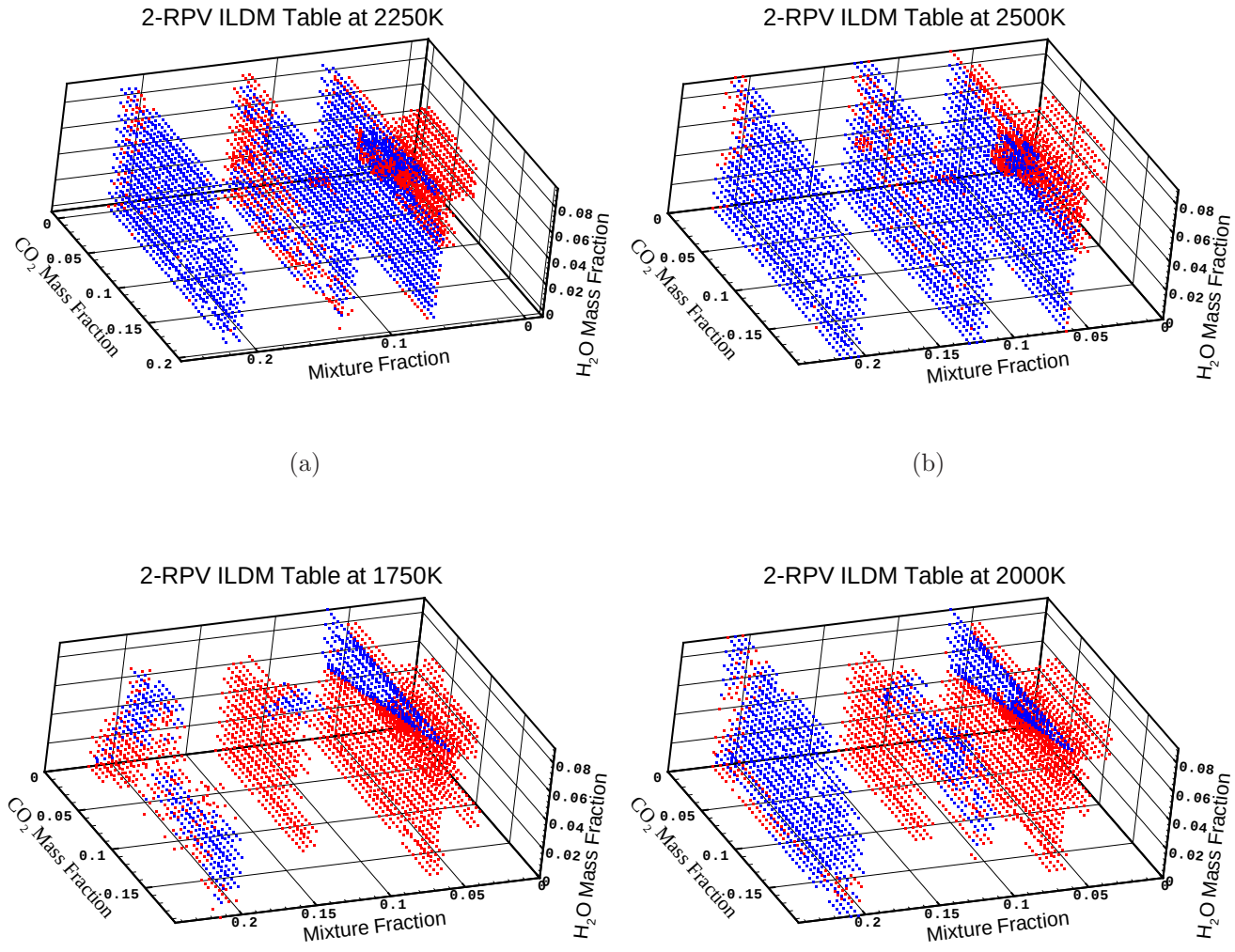

Figure 3: Slices of ILDM table with two reaction progress variables for heptane-air system at T=2000 K - 3000 K [139].

Bibliography

[1] I. Mayeres, S. Proost. *Why do we still have Diesel cars in Europe?* In EAERE 2000 Annual Conference, 30 June - 2 July 2000, pp 1–22, University of Crete, Department of Economics, Rethymnon, Greece,. 2000.

[2] C. Hibbs. *Diesel auto sales trending to exceed gasoline in Europe in 2006.* PriceWaterhouseCoopers Report, available at `http://www.greencarcongress.com/2006/01/diesel_auto_sale.html`, pp 14–18, 2004.

[3] N. Blackaby. *Once bitten, twice shy.* Power Engineering International **8**, pp 20–22, 2005.

[4] N. Peters. *Turbulent combustion.* Cambridge University Press, New York, NY, 2000.

[5] R. Klein. *Numerics in combustion.* Von Karman Institute, Belgium, 1999.

[6] R.B. Bird, W.E. Stewart, E.N. Lightfoot. *Transport phenomenon.* John Wiley & Sons, New York, 1960.

[7] F.A. Williams. *Combustion theory.* Addison-Wesley, New York, 1985.

[8] M.W. Chase Jr. (Ed.). *NIST-JANAF thermochemical tables, 4th ed.* National Institute of Standards and Technology, Boulder, CO, USA, 1998.

[9] C. Correa. *Combustion simulations in Diesel engine with reduced reaction mechanisms.* Phd thesis, University of Heidelberg, 2000.

[10] D. Veynante, L. Vervisch. *Turbulent combustion modeling.* Von Karman Institute, Belgium, 1999.

[11] P.A. Libby, F.A. William. *Turbulent reacting flows.* Springer Verlag, Berlin-Heidelberg, Germany, 1980.

[12] S.B. Pope. *Turbulent flows.* Cambridge University Press, Cambridge, UK, 2000.

[13] L. Prandtl. *Bericht über die einstehung der turbulenz.* Zeitschrift fur Angewandte Mathematik und Mechanik **5**, p 136, 1925.

[14] A.N. Kolmogorov. *The equations of turbulent motion in an incompressible fluid.* Izvestia Acad. Sci., USSR;Phys. **6**, pp 56–58, 1925.

[15] L. Prandtl. *Über ein neues formelsystem fur die ausgebildete turbulenz.* Nachr. Akad. Wiss. Göttingen Math-Phys. **k1**, pp 6–19, 1945.

[16] W.P. Jones, B.E. Launder. *The prediction of laminarization with a two-equation model of turbulence.* Int. J. of Heat and Mass Transfer **15**, pp 301–314, 1972.

[17] V. Yakhot, S.A. Orszag. *Renormalization group analysis of turbulence: Basic theory.* J. Sci. Computing **1**, pp 3–51, 1986.

[18] A.A. Amsden, P.J O'Rourke, T.D. Butler. *KIVA-II: A computer program for chemically reactive flows with sprays.* Los Alamos National Laboratory, LA-11560-MS, 1989.

[19] Z. Han, R.D. Reitz. *Turbulence modeling of internal combustion engines using RNG k-ϵ models.* Combust. Sci. and Tech. **106**, pp 267–295, 1995.

[20] H. Schlichting. *Boundary layer theory.* McGraw-Hill, NewYork, USA, 1968.

[21] V. Yakhot, L.M. Smith. *The renormalisation group, the ϵ expansion and derivation of turbulence models.* J. Sci. Computing **7**, p 35, 1992.

[22] G.N Coleman, N.N. Mansour. *Modeling the rapid spherical compression of isotropic turbulence.* Phys. Fluids A **3**, p 2225, 1991.

[23] S.H. El-Tahry. *A comparison of three turbulence models in engine like geometries.* International Symposium on Diagnostics and Modeling of Combustion in Internal Combustion Engines, (COMODIA) 85, Tokyo, Japan, p 203, 1986.

[24] J.B. Heywood. *Internal combustion engine fundamentals.* McGraw-Hill Book Co., Singapore, 1988.

[25] H. Tennekes, J.L. Lumley. *A first course in turbulence.* The MIT press, Cambridge, MA, USA, 1994.

[26] R.D. Reitz. *Assessment of wall heat transfer models for premixed-charge engine combustion computations.* SAE Papers **910267**, 1991.

[27] G.L. Borman. *In-cylinder heat transfer research at the U.W. Engine Research Center.* International Symposium on Diagnostics and Modeling of Combustion in Internal Combustion Engines, (COMODIA) 90, Kyoto, Japan, 1990.

[28] W.M. Kays. *Turbulent Prandtl number - where are we?* ASME J. Heat Transfer **116**, p 284, 1994.

[29] Z. Han, R.D. Reitz. *A temperature wall function formulation for variable density turbulent flows with application to engine convective heat transfer modeling.* Int. J. Heat Mass Transfer **40(3)**, pp 613–625 1997.

[30] A.A. Amsden, T.D. Butler, P.J. O'Rourke, J.D. Ramshaw. *KIVA - A comprehensive model for 2-D and 3-D engine simulations.* SAE Technical Paper **850554**, 1985.

[31] F.V. Bracco. *Modeling of engine sprays.* SAE Technical Paper **850394**, 1985.

[32] R.D. Reitz, R. Diwakar. *Structure of high-pressure sprays.* SAE Technical Paper **870598**, 1987.

[33] J. Xin, L. Ricart, R.D. Reitz. *Computer modeling of Diesel spray atomization and combustion.* Combust. Sci. Tech. **137**, pp 171–194, 1998.

[34] A.B. Liu, D. Mather, R.D. Reitz. *Modeling the effects of drop drag and breakup on fuel sprays.* SAE Paper 930072, 1993.

[35] C. Tatschl, E. v.Kunsberg Sarre, E. v.Berg. *IC-engine spray modeling status and outlook.* International Multidimensional Engine Modeling Users Group Meeting at the SAE Congress, 2002.

[36] P.J. O'Rourke, A. A. Amsden. *The TAB method for numerical calculation of spray droplet breakup.* SAE Technical Paper **SAE 872089**, 1987.

[37] R.D. Reitz. *Modeling atomization processes in high-pressure vaporizing sprays.* Atomisation Spray Technology **3**, pp 309–337, 1987.

[38] `http://www.fluentusers.com/fluent/doc/doc_f.htm`. *Fluent 6.2 User's Guide.* Fluent Inc., Lebanon, NH, USA, 2005.

[39] S.S Hwang, Z. Liu, R.D. Reitz. *Breakup mechanisms and drag coefficients of high speed vaporizing liquid drops.* Atomization and Sprays **6**, pp 353–376, 1996.

[40] L. Ricart, G. Bower, R.D. Reitz. *Cylinder measurements and modeling of liquid fuel spray penetration in heavy-duty Diesel engine.* SAE Technical Paper **971591**, 1997.

[41] P.J. O'Rourke. *Collective drop effects in vaporizing liquid sprays.* Phd thesis, Princeton University, 1981.

[42] N Nordin. *Mesh independent collision conditions for Lagrangian sprays.* `http://www.tfd.chalmers.se/~nordin/KJS/`, 2000.

[43] R. Viskanta, M.P. Mengüç. *Radiation heat transfer in combustion systems.* Prog. Ener. Combust. Sci. **13**, p 97, 1987.

[44] M. Kerker. *The scattering of light and other electromagnetic radiation.* Academic Press, San Diego, USA, 1969.

[45] J. DeRis. *Fire radiation - A review.* In Proceedings of the Combustion Institute, Vol. 17, pp 1003–1016, The Combustion Institute, Pittsburgh, PA, USA. 1978.

[46] B. Marracino, D. Lentini. *Radiation modeling in non-luminous non-premixed turbulent flames.* Combust. Sci. Technol. **128**, pp 23–48, 1997.

[47] R. Siegel, J.R. Howell. *Thermal radiation heat transfer.* Hemisphere Publishing, New York, USA, 1992.

[48] C. Correa, H. Niemann, B. Schramm, J. Warnatz. *Reaction mechanism reduction for higher hydrocarbons by the ILDM method.* In Proceedings of the Combustion Institute, Vol. 28, pp 1607–1614, The Combustion Institute, Pittsburgh, PA, USA. 2000.

[49] C.L. Tien, S.C. Lee. *Flame radiation.* Prog. Ener. Combust. Sci. **8**, p 41, 1982.

[50] C.B. Ludwig, W. Malkmus, J.G. Reardon, J.A. Thomson. *Handbook of infrared radiation from combustion gases.* Goulard, R. and Thomson, J.A. (Ed.), NASA SP-3080, Washington D.C., 1973.

[51] N. Lallemant, A. Sayre, R. Weber. *Evaluation of emissivity correlations for $H_/N2O$-CO_2-N_2/air mixtures and coupling with solution methods of the radiative transfer equation.* Prog. Ener. Combust. Sci. **22**, p 543, 1996.

[52] T.K. Kim, J.A. Menart, H.S. Lee. *Non-gray radiative gas analysis using the S-N discrete ordinates method.* J. Heat Transfer **115**, p 184, 1991.

[53] L. Zhang, A. Soufiani, J. Taine. *Spectral correlated and non-correlated radiative transfer in a finite axisymmetric system containing an absorbing and emitting real gas-particle mixture.* Int. J. Heat Mass Transfer **31**, pp 2261–2272, 1988.

[54] D.K. Edwards. *Advances in heat transfer, T.F. Irvine & J.P. Harnett (Eds.).* Academic Press, San Diego, USA, 1976.

[55] B. Leckner. *Spectral and total emissivity of water vapor and carbon dioxide.* Combust. Flame **19**, pp 33–48, 1972.

[56] H.C. Hottel, A.F. Sarofim. *Radiative heat transfer.* McGraw Hill, New York, USA, 1967.

[57] G.H. Markstein. *Radiative energy transfer from gaseous diffusion flames.* In Proceedings of the Combustion Institute, Vol. 15, pp 1285–1294, The Combustion Institute, Pittsburgh, PA, USA. 1975.

[58] W.W. Yuen, C.L. Tien. *A simple calculation scheme for the luminous-flame emissivity.* In Proceedings of the Combustion Institute, Vol. 16, p 1481, The Combustion Institute, Pittsburgh, PA, USA. 1977.

[59] W.H. Dalzell, A.F. Sarofim, Hoyt C. Hottel, I. A Vasalos. *Multiple scatter: A comparison of theory with experiment.* J. Heat Transfer **92**, pp 285–291, 1970.

[60] J.D. Felske, C.L. Tien. *Calculation of the emissivity of luminous flames.* Combust. Sci. Technol. **7**, pp 25–31, 1973.

[61] F.C. Lockwood, N.G. Shah. *The prediction of the particle laden gas flows.* In Proceedings of the Combustion Institute, Vol. 18, p 1481, The Combustion Institute, Pittsburgh, PA, USA. 1981.

[62] S. Chandrashekhar. *Radiative transfer.* Dover Press, New York, USA, 1960.

[63] R. Koch. *Calculation of multidimensional spectral radiation heat transfer in gas turbines - development and testing of methods.* Phd thesis, University of Karlsruhe, 1992.

[64] C.E. Choi, S.W. Baek. *Numerical analysis of a spray combustion with non-gray radiation using weighted sum of gray gases model.* Combust. Sci. Technol. **115**, pp 297–315, 1996.

[65] W.A. Fiveland. *Discrete ordinate methods for radiative heat transfer in isotropically and anisotropically scattering media.* J. Heat Transfer **109**, pp 809–812, 1987.

[66] A.S. Jamaluddin, P.J. Smith. *Radiative transfer in axisymmetric cylindrical enclosures using the discrete ordinates method.* Combust. Sci. Technol. **62**, p 173, 1988.

[67] A.S. Jamaluddin, P.J. Smith. *Predicting radiative transfer in rectangular enclosures using the discrete ordinates method.* Combust. Sci. Technol. **59**, pp 321–340, 1988.

[68] N. Selcuk, N. Kayakol. *Evaluation of discrete ordinates method for radiative transfer in rectangular furnaces.* Int. J. Heat Mass Trasnfer **40**, pp 213–222, 1997.

[69] B.R. Adams, P.J. Smith. *Three-dimensional discrete-ordinates modeling of radiative transfer in a geometrically complex furnace.* Combust. Sci. Technol. **88**, p 293, 1993.

[70] J. Warnatz, U. Maas, R.W. Dibble. *Combustion.* Springer Verlag, Berlin Heidelberg, 2^{nd} edition, 1999.

[71] C. Heghes. *New evaluated data for hydrocarbon kinetics.* Phd thesis, Universität Heidelberg, 2006.

[72] C.K. Westbrook, W. Pitz, J. Warnatz. *A detailed chemical kinetic reaction mechanism for the oxidation of iso-octane and n-heptane over an extended temperature range and its application to analysis of engine knock.* In Proceedings of the Combustion Institute, Vol. 22, pp 893–901, The Combustion Institute, Pittsburgh, PA, USA. 1988.

[73] C. Chevalier, P. Louessard, U.C. Müller, J. Warnatz. *A Detailed Low-Temperature Reaction Mechanism of n-Heptane Auto-Ignition.* In International Symposium on Diagnostics and Modeling of Combustion in Internal Combustion Engines (COMODIA), Vol. 90, pp 93–97, Nagoya, Japan, July 1-4. 1990.

[74] C. Chevalier, W. Pitz, J. Warnatz, H. Melenk. *Hydrocarbon ignition: automatic generation of reaction mechanisms and applications to modeling of engine knock.* In Proceedings of the Combustion Institute, Vol. 24, pp 93–101, The Combustion Institute, Pittsburgh, PA, USA. 1992.

[75] H.J. Curran, P. Gaffuri, W.J. Pitz, C.K. Westbrook. *A comprehensive modeling study of n-heptane oxidation.* Comb. and Flame **114**, pp 149–177, 1998.

[76] J. Warnatz. *Hydrocarbon ignition: Automatic generation of reaction mechanisms and applications to modeling of engine knock.* In Proceedings of the Combustion Institute, Vol. 20, pp 845–856, The Combustion Institute, Pittsburgh, PA, USA. 1984.

[77] H. Seiser, H. Pitsch, W.J. Pitz, H.J. Curran. *Extinction and auto-ignition of n-heptane in counterflow configuration.* In Proceedings of the Combustion Institute, Vol. 28, pp 2029–2037, The Combustion Institute, Pittsburgh, PA, USA. 2000.

[78] Ya. B. Zeldovich. *Oxidation of Nitrogen in combustion and explosion.* Doklady Akademii Nauk SSSR, Seriya A **51**, pp 217–220, 1946.

[79] C. P. Fenimore. *Formation of Nitric Oxide from fuel Nitrogen in Ethylene flame.* Combust. Flame **19**, p 289, 1972.

[80] K.C. Smyth. *NO production and destruction in a methane/air diffusion flame.* Combust. Sci. Tech. **115**, pp 151–176 1997.

[81] J.A Miller, C.T. Bowman. *Mechanism and modeling of Nitrogen chemistry in combustion.* Pro. Energy Combust. Sci. **17**, p 287, 1989.

[82] T. Just, S. Kelm. *Mechanisms of NO_x formation and abatement in technical combustion.* Industriefeuerung **38**, pp 96–102, 1986.

[83] J.M. Samaniego, F. N Egolfopoulos, C.T. Bowman. *Effect of chemistry and turbulence on NO formation in oxygen/natural gas flames.* In Proceedings of the Summer Program, pp 187–206, Center for Turbulence Research, Stanford university, Stanford, CA. 1996.

[84] H. Bockhorn (Ed.). *Soot formation in combustion. Springer Series in Chemical Physics, Vol. 59.* Springer Verlag, Berlin, 1994.

[85] Y. Yoshihara, A. Kazakov, H. Wang, M. Frenklach. *Reduced mechanism of soot formation - application to natural gas fueled Diesel combustion.* In Proceedings

of the Combustion Institute, Vol. 25, pp 941–948, The Combustion Institute, Pittsburgh, PA, USA. 1994.

[86] H. Pitsch, Y.P. Wan, N. Peters. *Numerical investigation of soot formation and oxidation under Diesel engine conditions.* SAE Technical Paper **952357**, pp 103–117, 1995.

[87] H. Pitsch, H. Barths, N. Peters. *Three-dimensional modeling of NO_x and soot formation in DI-Diesel engines using detailed chemistry based on the interactive flamelet approach.* SAE Technical Paper **962057**, pp 2010–2024, 1996.

[88] P. W. Atkins. *Heat Transfer in Flames, Afgan, A.H. and Beer J.M., Eds.* Scripta, 1974.

[89] J.B. Moss, C.D. Stewart, K.J. Syed. *Flow-field modeling of soot formation at elevated pressure.* In Proceedings of the Combustion Institute, Vol. 23, pp 413–423, The Combustion Institute, Pittsburgh, PA, USA. 1988.

[90] K.J. Syed, J.B. Moss, C.D. Stewart. *Modeling soot formation and thermal radiation in buoyant turbulent diffusion flames.* In Proceedings of the Combustion Institute, Vol. 24, p 1533, The Combustion Institute, Pittsburgh, PA, USA. 1990.

[91] J.B. Moss, K.J. Young. *Modeling sooting turbulent jet flames using an extended flamelet technique.* Combust. Sci. Technol. **105**, pp 33–53, 1995.

[92] C.D. Stewart, K.J. Syed, J.B. Moss. *Modeling soot formation in non-premixed Kerosene-Air flames.* Combust. Sci. Technol. **75**, pp 211–226, 1991.

[93] J.B. Moss, C.D. Stewart, K.J. Young. *Modeling soot formation and burnout in a high temperature laminar diffusion flame burning under oxygen-enriched conditions.* Combust. Flame **101**, pp 491–500, 1995.

[94] N.W. Bressloff, J.B. Moss, P.A Rubini. *CFD prediction of coupled radiation heat transfer and soot production in turbulent flames.* In Proceedings of the Combustion Institute, Vol. 26, p 2379, The Combustion Institute, Pittsburgh, PA, USA. 1996.

[95] J. Sojka. *Simulation des russbildung unter homogenen verbrennungsbedingungen.* Phd thesis, Universität Heidelberg, 2000.

[96] H. Kellerer, Müller, H. J. Bauer, S. Wittig. *Soot formation in a shock tube under elevated pressure conditions. Combustion Science and Technology.* Combust. Sci. Technol. **114**, pp 67–80, 1996.

[97] B.S. Haynes, H.G. Wagner. *Soot formation.* Prog. Ener. Combust. Sci. **7**, p 229, 1995.

[98] H. Jander. *Personal communications of Chrys Correa.* University of Göttingen, Personal communications of Chrys Correa 1999.

[99] J. Warnatz. *The structure of laminar alkane, alkene, and acetylene flames.* In Proceedings of the Combustion Institute, Vol. 18, pp 369–384, The Combustion Institute, Pittsburgh, PA, USA. 1981.

[100] W.P. Bartok, A.F. Sarofim (Ed.). *Fossil fuel combustion.* John Wiley and Sons, Inc., New York, NY, 1^{st} edition, 1991.

[101] R.S. Barlow, J.H. Frank. *Effects of turbulence on species mass fractions in Methane/Air jet flames.* In Proceedings of the Combustion Institute, Vol. 27, pp 1087–1095, The Combustion Institute, Pittsburgh, PA, USA. 1998.

[102] J-Y. Chen, W. Kollmann, R.W. Dibble. *PDF modeling of turbulent non-premixed methane jet flames.* Combust. Sci. Technol. **64**, pp 315–346, 1989.

[103] A.R. Masri, R.W. Dibble, R.S. Barlow. *Raman-Rayleigh measurements in bluff-body stabilized flames of hydrocarbon fuels.* In Proceedings of the Combustion Institute, Vol. 24, pp 317–324, The Combustion Institute, Pittsburgh, PA, USA. 1992.

[104] S.M. Correa, A. Gulati, S.B. Pope. *Raman measurements and joint PDF modeling of a non-premixed bluff-body-stabilized methane flame.* In Proceedings of the Combustion Institute, Vol. 25, pp 1167–1173, The Combustion Institute, Pittsburgh, PA, USA. 1994.

[105] R.S. Barlow, J-Y. Chen. *On transient flamelets and their relationship to turbulent methane-air jet flames.* In Proceedings of the Combustion Institute, Vol. 24, pp 231–237, The Combustion Institute, Pittsburgh, PA, USA. 1992.

[106] S.H. Stårner, R.W. Bilger, R.W. Dibble, R.S. Barlow. *Piloted diffusion flames of diluted methane near extinction: detailed structure from laser measurements.* Combust. Sci. Technol **72**, pp 225–269, 1990.

[107] F. Mauß, D. Keller, N. Peters. *A Lagrangian simulation of flamelet extinction and re-ignition in turbulent jet diffusion flames.* In Proceedings of the Combustion Institute, Vol. 23, pp 693–698, The Combustion Institute, Pittsburgh, PA, USA. 1991.

[108] R.O. Fox. *Computational models for turbulent reactive flows.* Cambridge University Press, New York, NY, 2003.

[109] S. Menon, V. Sankaran. *Structure of premixed turbulent flames in the thin-reaction-zones regime.* In Proceedings of the Combustion Institute, Vol. 28, pp 203–209, The Combustion Institute, Pittsburgh, PA, USA. 2000.

[110] H. Pitsch, H. Steiner. *Large-eddy simulation of a turbulent piloted methane/air diffusion flame (Sandia flame D).* Phys. Fluids **12**, 2541–2554, 2000.

[111] S.B. Pope. *Computations of turbulent combustion: progress and challenges.* In Proceedings of the Combustion Institute, Vol. 23, pp 591–612, The Combustion Institute, Pittsburgh, PA, USA. 1990.

[112] L.A. Vulis. *Turbulent burning velocity.* Explosion, combustion and shock waves **8**, pp 3–8, 1972.

[113] S-Y. Lee, S. Seo, J.C. Broda, S. Pal, R.J. Santoro. *An Experimental estimation of mean reaction rate and flame Structure during combustion Instability in a Lean premixed gas turbine combustor.* In Proceedings of the Combustion Institute, Vol. 28, pp 775–782, The Combustion Institute, Pittsburgh, PA, USA. 2000.

[114] S.B. Pope. *Monte-Carlo calculations of premixed turbulent flames.* In Proceedings of the Combustion Institute, Vol. 18, pp 1001–1010, The Combustion Institute, Pittsburgh, PA, USA. 1981.

[115] S.B. Pope. *PDF methods for turbulent reactive flows.* Prog. Energy Combust. Sci. **11**, p 119, 1985.

[116] M. Brandt, W. Polifke. *Tabulation of mean reaction rates from multivariate, correlated distributions with a Monte-Carlo method.* In Int. Conference on Numerical Combustion, Vol. 9, pp 303–304, 2002.

[117] F. Cullick, M.V. Heitor, J.H. Whitelaw (Ed.). *Jones, W.P. and Kakhi, M. in Unsteady combustion.* Springer, Berlin-Heidelberg, 1996.

[118] S.S. Girimaji. *Assumed β-PDF model for turbulent mixing: Validation and extension to multiple scalar mixing.* Combust. Sci. Technol. **78**, p 177, 1991.

[119] F.C. Lockwood, A.S. Naguib. *Aspects of combustion modeling in engineering turbulent diffusion flames.* J. of the Institute of Fuel **49**, pp 218–223, 1976.

[120] J. Janicka, W. Kollmann. *A two-variable formalism for the treatment of chemical reactions in turbulent hydrogen-air diffusion flames.* In Proceedings of the Combustion Institute, Vol. 17, pp 421–430, The Combustion Institute, Pittsburgh, PA, USA. 1981.

[121] E.E. Khalil, D.B. Spalding, J.H. Whitelaw. *Calculation of local flow properties in two-dimensional furnaces.* Int. J. Heat Mass Transfer **18**, pp 775–791, 1975.

[122] N. Peters. *Reduced kinetic mechanisms for applications in combustion systems.* Springer Verlag, Berlin-Heidelberg, 1993.

[123] M.D. Smooke. *Reduced kinetic mechanisms and asymptote approximations for Methane-Air Flames.* Lecture Notes in Physics, 1991.

[124] L.M.T. Sommers, L.P.H. de Goey. *Analysis of a systematical reduction technique.* In Proceedings of the Combustion Institute, Vol. 25, pp 957–963, The Combustion Institute, Pittsburgh, PA, USA. 1994.

[125] S.H. Lam, D.A. Goussis. *Understanding complex chemical kinetics with computational singular perturbation.* In Proceedings of the Combustion Institute, Vol. 22, pp 931–941, The Combustion Institute, Pittsburgh, PA, USA. 1989.

[126] H.N. Najm, J.C. Lee, M. Valorani, D.A. Goussis, M. Frenklach. *An algorithm for the organization of information.* Journal of Physics: Conference Series **16**, pp 101106, 2005.

[127] U. Maas, S.B. Pope. *Simplifying chemical kinetics: intrinsic low-dimensional manifolds in composition space.* Comb. Flame **88**, p 239 1992.

[128] U. Maas. *Automatische Reduktion von Reaktionsmechanismen zur Simulation Reaktiver Strömungen.* Habilitationsschrift, Universität Stuttgart, 1993.

[129] U Maas, S.B. Pope. *Implementation of simplified chemical kinetics based on intrinsic low-dimensional manifolds.* In Proceedings of the Combustion Institute, Vol. 24, p 103, The Combustion Institute, Pittsburgh, PA, USA. 1993.

[130] R. Rawat. *Modeling finite-rate chemistry in turbulent reacting flows.* Phd thesis, University of Utah, Salt Lake City, UT, 1997.

[131] R.L.G.M Eggels. *Modeling of combustion process and NO formation with reduced reaction mechanism.* Phd thesis, Eindhoven University of Technology, 1996.

[132] H. Niemann. *Automatische reduktion chemischer reaktionsmechanismen.* Phd thesis, IWR, University of Heidelberg, 2000.

[133] B.S. Schramm. *Automatische reduktion chemischer reaktionsmechanismen am beispiel der oxidation von höheren kohlenwasserstoffen und deren verwendung in reaktiven strömungen.* Phd thesis, IWR, University of Heidelberg, 2003.

[134] G. Adelson-Velskii, E.M. Landis. *An algorithm for the organization of information.* Soviet Math. Doklady **3**, pp 12591263, 1962.

[135] V. Eswaran, S.B. Pope. *Direct numerical simulations of turbulent mixing of a passive scalar.* Physics of Fluids **31(3)**, p 506, 1988.

[136] A. Vranos. *A generalized conditional scalar dissipation-mixture fraction joint PDF for flamelet modeling of non-premixed flames.* Combust. Sci. Technol. **84**, pp 323–334, 1992.

[137] W.J.A. Dahm, K.A. Buch. *Log normality of the scalar dissipation PDF in turbulent flows.* Physics of Fluids A, **1**, pp 1290–1293, 1989.

[138] J. Warnatz. *EQLIB: Equilibrium composition and adiabatic flame temperature.* Steinbeis-Transferzentrum, Heidelberg, ver. 2.7, 2003 edition, 1974.

[139] V. Reinhardt. *Personal communications of Ravindra Aglave.* IWR, University of Heidelberg, 2005.

[140] D. Schmidt. *Modellierung reaktiver strömungen unter verwendung automatisch reduzierter reaktionsmechanismen.* Phd thesis, Universität Heidelberg, 1996.

[141] N. Miyamoto, H. Ogawa, M. Shibuya, K. Arai, O. Esmilaire. *Soot formation.* SAE Paper **940676**, 1994.

[142] C. Correa, H. Niemann, B. Schramm, J. Warnatz. *Use of ILDM reduced chemistry in direct injection Diesel engines.* In Thermo- and Fluid-Dynamic Processes in Diesel Engines, Selected Papers from the THIESEL 2000 Conference, pp 353–362, Valencia, Spain, Sept. 13-15. 2002.

[143] D. C. Kyritsis, V. S. Santoro, S. Gomez. *Quantitative scalar dissipation rate measurements in vortex perturbed counterflow diffusion flames.* In Proceedings of the Combustion Institute, Vol. 29, pp 1679–1685, The Combustion Institute, Pittsburgh, PA, USA. 2002.

[144] B. Cuenot, F. N. Egolfopoulos, P. Poinsot. *An unsteady laminar flamelet model for non-premixed combustion.* Combust. Theory and Modeling, **4**, pp 77–97, 2000.

[145] P.S. Kothnur, N.T. Clemens. *Experimental investigation of the relationship between strain and scalar dissipation in gas-phase turbulent jets.* 39th AIAA Aerospace Sciences Meeting, Reno, NV, **AIAA-2001-1023**, 2001.

[146] P.S. Kothnur, N.T. Clemens. *Effects of unsteady strain rate on scalar dissipation structures in turbulent planar jets.* `http://www.ae.utexas.edu/~clemens/pf-kc.pdf`, submitted to Physics of Fluids, 2004.

[147] H.G. Im, J. H. Chen. *Chemical response of methane/air diffusion flames to unsteady strain rate.* Combust. and Flame, **100**, pp 204–212, 1999.

[148] L.K. Su. *Measurements of the three-dimensional scalar dissipation rate in gas-phase planar turbulent jets.* Annual Research Briefs, Center for Turbulence Research, Stanford University, pp 35–46, 1998.

[149] H. Pitsch, S. Fedotov. *Stochastic modeling of scalar dissipation rate fluctuations in non-premixed turbulent combustion.* Annual Research Briefs, Center for Turbulence Research, Stanford University, pp 91–103, 2000.

[150] H. Pitsch, C. M. Cha, S. Fedotov. *Interacting flamelet model for non-premixed turbulent combustion with local extinction and re-ignition.* Annual Research Briefs, Center for Turbulence Research, Stanford University, pp 65–77, 2001.

[151] N. Peters. *Laminar diffusion flamelet models in non-premixed turbulent combustion.* Prog. Energy Combust. Sci., **10**, p 319, 1984.

[152] Unknown. *Creation of the whorléd.* National Energy Research Scientific Computing Center, Annual Report, available on the web at `http://www.nersc.gov/news/annual_reports/annrep04/annrep04.pdf`, pp 14–18, 2004.

[153] S. Sreedhara, K.N. Lakshmisha. *Autoignition in a non-Premixed medium: DNS studies on the effects of three-dimensional turbulence.* In Proceedings of the Combustion Institute, Vol. 29, pp 2051–2059, The Combustion Institute, Pittsburgh, PA, USA. 2002.

[154] M. R. Elsden, E. Gutheil, M. Nehse, J. Warnatz. *Diesel engine ignition modeling.* VDI-Berichte **1313**, pp 473–478 1997.

[155] E. Gutheil. *Modellierung turbulenter kohlenstoffmonoxid/Luft diffusionsflammen.* Phd thesis, TH Darmstadt, 1981.

[156] H. Pitsch, Y.P. Wan, N. Peters. *Simulation of autoignition delay and location of fuel sprays under Diesel engine relevant conditions.* SAE Technical Paper **971590**, pp 103–117, 1997.

[157] S.V. Patankar. *Numerical heat transfer and fluid flow.* Hemisphere Publishing, NewYork, USA, 1980.

[158] S.F. Ashby, A. Manteuffel, P.E. Saylor. *A taxonomy for conjugate gradient methods.* SIAM J. Numer. Anal. **27**, pp 1542–1568, 1990.

[159] R.D. Reitz. *Personal communications of Chrys Correa.* Engine Research Center, University of Wisconsin, Personal Communications of Chrys Correa 1999.

[160] T. Ishiyama, K. Miwa, O. Horikoshi. *A study on ignition process of Diesel engines.* International Symposium on Diagnostics and Modeling of Combustion in Internal Combustion Engines, (COMODIA) 94, Tokyo, Japan, pp 337–342, 1994.

[161] J. Warnatz. *Gas phase combustion chemistry.* Gardiner, W.C.(Ed.), Springer Verlag, Heidelberg-Berlin, 2000.

[162] S. Liu, J.C. Hewson, J.H. Chen, H. Pitsch. *Effect of strain rate on high-pressure non-premixed n-heptane autoignition in counterflow.* Combust. & Flame **137**, pp 320–339, 2004.

[163] N. Peters, G. Packzo, R. Sieser, K. Sheshadri. *Temperature crossover and non-thermal runaway at two stage ignition of Heptane.* Combust. & Flame **101**, pp 38–59, 2002.

Nomenclature

δ	Kronecker delta dependent on the sign of velocity dilatation
$\dot{\rho}_i^{\mathrm{C}}$	Source term due to chemistry of species i
$\dot{\rho}_i^{\mathrm{S}}$	Source term due to spray of species i
$\dot{F}^{\mathrm{S}}$	Momentum source term due to spray
$\dot{Q}^{\mathrm{C}}$	Heat source term due to chemistry
$\dot{Q}^{\mathrm{S}}$	Heat source term due to spray
$\dot{Q}_{\mathrm{d}}$	Heat conduction rate to the droplet surface per unit area
ϵ	Turbulent kinetic energy dissipation rate
Γ_ϕ	General molecular diffusion coefficient
κ	von Karman's constant(= 0.4372)
Λ_{KH}	Wavelength of the Kelvin-Helmholtz instability
Λ_{RT}	Wavelength of the Rayleigh-Taylor instability
$\boldsymbol{\nabla^2}$	Laplacian operator/gradient(scalar)
$\Gamma_{\phi,\mathrm{T}}$	General turbulent diffusion coefficient
μ, μ_{L}	Laminar viscosity= $\rho\nu$
μ_{eff}	Effective or dynamic viscosity = $\mu_L + \mu_T$
μ_{T}	Turbulent viscosity= $\rho\nu_T$
∇	Divergence operator (vector)
ν, ν_L	Laminar kinematic viscosity= μ/ρ
ω_i	Molar rate of formation of species i
Ω_{KH}	Fastest growing frequency of the Kelvin-Helmholtz instability
Ω_{RT}	Fastest growing frequency of the Rayleigh-Taylor instability

ρ	Density
ρ_i	Density of species i
$\bar{\bar{\sigma}}$	Viscous stress tensor
$\tilde{\dot{\omega}}$	Mean reaction rate
$\vec{\boldsymbol{g}}$	Gravitational force vector
$\vec{\boldsymbol{J_i}}$	Diffusion flux of species i $\left(= \rho_i \vec{V_i}\right)$
$\vec{\boldsymbol{J}}_q$	Heat flux vector
$\vec{\boldsymbol{u}}$	Velocity vector
$\vec{\boldsymbol{V_i}}$	Diffusion velocity of species i
ζ	Wall heat loss
A	Pre-exponential factor in Arrhenius expression
B_{d}	Droplet Spalding number
$c_{\mathrm{p,L}}$	Specific heat capacity of liquid (fuel)
C_μ	Empirically determined constant for the k-ϵ model ($= 0.09$)
c_p	Specific heat capacity
D_{T}	Turbulent mass diffusivity
D_{ij}	Binary diffusion coefficient of species i in species j
D_i	Mean diffusion coefficient of species i in the most abundant species
E	Specific internal energy
E_{A}	Activation energy
h_i	Specific enthalpy of species i
J_{w}	Wall heat flux
K	Thermal conductivity of the fluid mixture
K_{T}	Thermal conductivity
$L\left(T_{\mathrm{d}}\right)$	Latent heat of evaporation
M_i	Molar mass of species i
Pr	Prandtl number $= \frac{c_p \mu}{k}$

Pr_{T}	Turbulent Prandtl number
R_{c}	Critical cell Reynolds number (= 144 for Diesel engine case)
r_{c}	Radius of a child droplet
Re_{d}	Droplet Reynolds number
S_{ϕ}	Source/sink term
Sc	Schmidt number = $\frac{\mu}{\rho D}$
Sc_{d}	Droplet Schmidt number
Sc_{T}	Turbulent Schmidt number
Sh_{d}	Droplet Sherwood number
Ta	Taylor number
u_{w}	Friction velocity or the velocity of the fluid at the wall
We	Weber number
We_{L}	Liquid Weber number
xi_{C}	Mixture fraction based on element C
Y_i	Mass fraction of species i
Z	Ohnesorge number
Z_i	Mass fraction of element i

List of Figures

List of Tables

Index

Erklärung:

Hiermit versichere ich, daß ich die Arbeit selbständig verfaßt und keine anderen als die angegebenen Quellen und Hilfsmittel verwendet habe.

Heidelberg, den Ravindra Aglave